Model Predictive Control of a Medium-voltage Grid-connected Converter with LC Filter using Optimal Pulse Patterns with Relaxed Symmetry

by

Annika Christine Birth

Thesis presented in fulfilment of the requirements for the degree of

Master of Engineering (Electrical)

in the Faculty of Engineering at Stellenbosch University

Supervisors: Prof T. Geyer
Prof H. du T. Mouton

March 2020

Declaration

By submitting this thesis electronically, I declare that the entirety of the work contained therein is my own, original work, that I am the sole author thereof (save to the extent explicitly otherwise stated), that reproduction and publication thereof by Stellenbosch University will not infringe any third party rights and that I have not previously in its entirety or in part submitted it for obtaining any qualification.

Annika Christine Birth

Abstract

Medium-voltage converters are operated at very low switching frequencies. To minimise the resulting harmonic distortions, offline computed optimised pulse patterns are the modulation method of choice. The optimal switching angles, at which a converter phase switches, are obtained by solving a constrained optimisation problem.

To simplify the analysis and computation, quarter- and half-wave symmetry of the switching function is typically imposed. Moreover, for three-level converters, the switch positions are required to be non-negative in the positive half-wave of the fundamental period. The impact of these restrictions on the harmonic performance of the pulse patterns is investigated in the first part of this thesis. By relaxing the symmetry restrictions and by allowing also negative switch positions in the positive half-wave of the fundamental period, the current distortions can be reduced by up to one third compared to the traditional problem formulation.

Commonly used linear control techniques require zero current ripple at regularly-spaced sampling instants. For optimised pulse patterns, in general, the current ripple is never zero in all three phases. Moreover, the switching angles may be discontinuous when varying the modulation index. To address these issues, controllers based on trajectory tracking were developed, most notably model predictive pulse pattern control. By treating the fundamental and harmonic components as one single quantity, it achieves superior disturbance rejection and very short settling times during transients.

However, only a single (vector valued) variable is controlled with this method, such as the stator flux linkage of a machine or the converter current of a grid-connected converter. To address higher-order systems, such as converters with LC filters, an additional damping loop is required limiting its performance during transients. In the second part of this thesis, a generalised model predictive pulse pattern controller is proposed. It regulates multiple controlled variables along their nominal trajectories and does not require an additional active damping loop. Nearly optimal steady-state performance and fast transient response times are achieved in simulations.

Opsomming

Mediumspanning omsetters word bedryf teen baie lae skakelfrekwensies. Aflynberekende geoptimeerde pulspatrone is die modulasie tegniek van keuse om die gevolglike harmoniese distorsie te verminder. Die optimale vuurhoeke, waarteen die omsetter skakel, word verkry deur 'n optimeringsprobleem met beperkings op te los.

Om beide die analiese en berekeninge te vereenvoudig, word kwartgolf en halfgolf simmetrie tipies toegepas. Drievlak omsetters vereis dat die skakelposisies nie-negatief moet wees tydens die positiewe halfsiklus van die fundamentele periode. Die gevolg van hierdie beperkings op die harmoniese optrede van die pulspatroon word ondersoek in die eerste deel van hierdie tesis. Deur die kwartgolf simmetrie te ontspan en die negatiewe skakelposisies toe te laat tydens die positiewe halfsiklus, kan die stroomharmoniese distorsies verminder word met tot 'n derde in vergelyking met die tradisionele formulering.

Algemene lineêre beheertegnieke benodig nul stroomriffel by die die monsteroomlikke. Oor die algemeen is die stroomriffel nooit nul nie in al drie fases wanneer geoptimeerde pulsepatron gebruik word. Verder kan die vuurhoeke diskontinu word wanneer die modulasieindeks verander word. Om hierdie probleme aan te spreek, was beheerders gebasseer op trajekvolging ontwerp. Modelvoorspellendepulspatroonbeheer is die mees merkwaardigste van hierdie beheertegnieke. Deur die fundamentele komponent en riffel as 'n enkele kwantiteit te hanteer, bereik die laasgenoemde beheer tegniek uitstekende steuringsverwerping and baie kort vestigingstye tydens oordragsverskynsels.

Slegs 'n enkele veranderlike (vektor waarde) word beheer met hierdie metode, soos byvoorbeeld die stator vloedkoppeling van 'n masjien of the omsetterstroom van 'n kragnetwerkgekoppelde omsetter. Hoë-orde stelsels, soos byvoorbeeld omsetters met LC-filters, vereis 'n addisionele dempingslus wat hul optrede tydens oorgangsverskynsels belemmer. 'n Veralgemeende modelvoorspellendebeheerder pulspatroon strategie word voorgestel in die tweede deel van hierdie tesis. Dit reguleer verskeie beheerde veranderlikes al langs hul onderskeie nominale trajekte en vereis nie die gebruik van 'n addisionele aktiewe dempingslus nie. Beinaoptimale bestendigde toestand optrede asook vinnige oorgangs-optrede word bereik in simulasies.

Acknowledgements

First of all, I am thankful to Prof Mouton and Tobias Geyer for making my Master studies possible and allowing me to learn from both of them over the past two years. Thank you Prof Mouton, for having the initial idea for this Masters and the trust that I can do it. Thank you Tobias, for your guidance and endless patience.

I also want to thank Tinus Dorfling for always having an open ear, no matter what troubles I had. Thank you also for the treats that we enjoyed.

At the ABB Research Center, I had the chance to meet so many amazing and inspiring people from the permanent employees and the interns, which I am very grateful for. Some brief talks during coffee or lunch breaks often gave me the motivation to tackle the next coming problem and push through the hard times.

Last, I want to thank my friends and family for never giving up to remind me that there is a life outside of the office and my Masters. Thank you all!

Contents

Nomenclature

Symbols

a_n, b_n	Fourier coefficients of the nth harmonic
A	Vector of single-phase switching angles
$\boldsymbol{A}, \tilde{\boldsymbol{A}}_i$	System matrix in the discrete-time domain
α_i	ith switching angle, $\alpha_i \in [0, 2\pi]$
$\boldsymbol{B}, \tilde{\boldsymbol{B}}_i$	Input matrix in the discrete-time domain
$\boldsymbol{C}$	Output matrix in the continuous-time and discrete-time domains
d	Pulse number, $d \in \mathbb{N}$
f_1	Fundamental frequency
f_{sw}	Switching frequency
$\boldsymbol{F}, \tilde{\boldsymbol{F}}$	System matrix in the continuous-time domain
$\boldsymbol{G}, \boldsymbol{G}_1, \boldsymbol{G}_2$	Input matrix in the continuous-time domain
γ^*	Load angle
$\boldsymbol{H}$	Hessian matrix in the QP
$i_p(t)$	Current in continuous-time domain in phase p
$\boldsymbol{i}_{abc}(t)$	Three-phase current in continuous-time domain
J	Objective function for optimisation problem
$\boldsymbol{K}, \boldsymbol{K}^{-1}$	Clarke transformation matrices
k	Discrete time step, $k \in \mathbb{N}$
ℓ	Discrete time step within the prediction horizon, $\ell \in \{k, k+1, \ldots, k+N\}$
L_σ	Leakage inductance in SI
m	Modulation index, $m \in [0, \frac{4}{\pi}]$
n	Harmonic order, $n \in \mathbb{N}$
n_p	Number of switching transitions within the prediction horizon in phase p, $n_p \in \mathbb{N}$
n_{pk}	Number of switching transitions in the kth sampling interval in phase p, $n_{pk} \in \mathbb{N}$
n_u, n_x, n_y	Dimension of the input, state and output vector
N	Prediction horizon, $N \in \mathbb{N}$
p	Phase, $p \in \{a, b, c\}$
P	Real power
ϕ	Phase angle
Q	Reactive power
t	Time, $t \in \mathbb{R}^+$
t_{pi}	Modified ith switching instant in phase p, $t_{pi} \in \mathbb{R}^+$
Δt_{pi}	Switching instant modification in phase p for the ith switching transition, $\Delta t_{pi} \in \mathbb{R}$
T_s	Sampling interval, $T_s \in \mathbb{R}^+$
θ	Angle argument in pulse pattern, $\theta \in [0, 2\pi]$

$\boldsymbol{\theta}_1^*$	Vector of sampling angles for computing the reference trajectory contribution of the converter voltage, $\boldsymbol{\theta}_1^* \in [0, 2\pi]$
u_i	ith single-phase switch position, $u_i \in \mathcal{U}$
$u_p(t)$	Switching signal in continuous-time in phase p, $u_p(t) \in \mathcal{U}$
$\boldsymbol{u}_{abc}(t)$	Three-phase switching signal in continuous-time, $\boldsymbol{u}_{abc}(t) \in \mathcal{U}^3$
$u_p(\theta)$	Pulse pattern over one fundamental period of 2π, $u_p(\theta) \in \mathcal{U}$
Δu_i	ith switching transition, $\Delta u_i \in \{-1, 1\}$
U	Vector of single-phase switch positions
$\mathcal{U}$	Set of converter levels, $\mathcal{U} = \{-1, 0, 1\}$
$\mathcal{U}^+$	Set of non-negative converter levels, $\mathcal{U}^+ = \{0, 1\}$
$v_p(t)$	Voltage in continuous-time domain in phase p
$\boldsymbol{v}_{abc}(t)$	Three-phase voltage in continuous-time domain
$w_p(k)$	Averaged switch position in phase p in kth sampling interval, $w_p \in [-1, 1]$
$\boldsymbol{w}_{abc}(k)$	Three-phase averaged switch position in kth sampling interval, $\boldsymbol{w}_{abc} \in [-1, 1]^3$
$\boldsymbol{W}_{abc}(k)$	Sequence of three-phase averaged switch positions over the prediction horizon computed at time instant kT_s, $\boldsymbol{W}_{abc} \in [-1, 1]^{3N}$
$\Delta w_p(k)$	Correction of the averaged switching signal in phase p in the kth sampling interval, $\Delta w_p \in [-1, 1]$
$\Delta \boldsymbol{W}_{abc}(k)$	Sequence of averaged switch positions corrections over the horizon computed at time instant kT_s, $\Delta \boldsymbol{W}_{abc} \in [-1, 1]^{3N}$
ω_1	Angular fundamental frequency, $\omega_1 = 2\pi f_1$
$\boldsymbol{x}_{\alpha\beta}(t)$	State variable in stationary orthogonal $\alpha\beta$ coordinates
X_σ	Leakage reactance in pu
$\boldsymbol{y}_{\alpha\beta}(t)$	Output variable in stationary orthogonal $\alpha\beta$ coordinates
$\boldsymbol{Y}^*_{1\text{conv},\alpha\beta}(\theta)$	Reference trajectory contribution of converter voltage sampled over one fundamental period with $\boldsymbol{\theta}_1^*$
$\boldsymbol{Y}^*_{\alpha\beta}(k)$	Reference trajectory for the controller over prediction horizon computed at time instant kT_s

Variables

$\mathcal{U}$	Set
$z(t)$	Scalar quantity in the continuous-time domain
$z(k)$	Scalar quantity in the discrete-time domain
$\boldsymbol{z}$	Column vector referring to, e.g. a three-phase quantity
Z	Column vector referring to a sequence of scalar quantities over multiple time instants
$\boldsymbol{Z}$	Column vector referring to a sequence of vector quantities over multiple time instants or a matrix

Superscripts

A^*, t^*	Vector of optimal switching angles, nominal switching time for MP^{3}C$^+$
$\hat{i}$	Amplitude of current
$\overline{w}$	Upper bound on averaged switch position
$\underline{w}$	Lower bound on averaged switch position
$\tilde{\boldsymbol{x}}$	State vector of reduced dimension
$\boldsymbol{z}^T$	Row vector

Subscripts

A_F	Vector of switching angles for the full-wave symmetric OPP
A_H	Vector of switching angles for the half-wave symmetric OPP
A_Q	Vector of switching angles for the quarter- and half-wave symmetric OPP with multipolar switch positions
A_{uQ}	Vector of switching angles for the quarter- and half-wave symmetric OPP with unipolar switch positions
$\boldsymbol{i}_{abc}$	Three-phase current in abc coordinates
$\boldsymbol{i}_{\alpha\beta}$	Three-phase current in $\alpha\beta$ coordinates
i_c	Converter current
i_g	Grid current
i_s	Stator current
I_B	Base current for per unit system
I_R	Rated current
I_{TDD}	Total demand distortion of the current
u_n	Switching signal harmonic of order n
v_{cap}	Capacitor voltage
v_0	Common-mode voltage
$\boldsymbol{y}_{\text{conv}}$	Reference vector contribution of converter voltage
$\boldsymbol{y}_{\text{grid}}$	Reference vector contribution of grid voltage

Abbreviations

dc	Direct current
FWS	Full-wave symmetry
HWS	Half-wave symmetry
MV	Medium-voltage
MPC	Model predictive control
MP^{3}C	Model predictive pulse pattern control
MP^{3}C$^+$	Proposed model predictive pulse pattern control with averaged switch positions
NPC	Neutral-point-clamped
OPP	Optimised pulse pattern
PCC	Point of common coupling
pu	Per unit
PWM	Pulse width modulation
QaHWS	Quarter- and half-wave symmetry with multipolar switch positions
QaHWS$^+$	Quarter- and half-wave symmetry with unipolar switch positions
QP	Quadratic program
rms	Root-mean-square
SHE	Selective harmonic elimination
TDD	Total demand distortion

Chapter 1

Introduction

1.1 Research Motivation

In power electronics, a fundamental trade-off between the *switching effort* of the converter and the generated *harmonic distortion* in the load exists. The switching effort relates to switching losses in the semiconductor switches, which are limited by the cooling capacity of the converter. Reducing the switching effort thus allows higher power ratings, which increases the efficiency of the converter. The supplied load is typically an electrical machine or the grid. Harmonic distortion in the stator currents of the machine cause copper and iron losses. In case of a grid-connected converter, strict harmonic standards have to be met. In conclusion, the goal of generating sinusoidal output waveforms conflicts with the thermal limitations in the converter.

In medium-voltage (MV) applications, the switching frequency is restricted to a few hundred Hertz. Consequently, particular attention is required to reduce the harmonic distortions as much as possible. Optimised pulse patterns (OPPs) allow the minimisation of the current harmonic distortions for a given switching frequency. For the computation of such optimised switching signals, certain assumptions are typically made. While research on OPPs mainly focuses on the application of OPPs to various converter types and their efficient computation, the impact of such imposed assumptions has been neglected without further consideration.

OPPs are optimal under ideal steady-state conditions. In real-life applications, a controller is required to modify the OPP in order to handle non-idealities and disturbances, such as a ripple of the dc-link voltage and measurement noise. A modern versatile control strategy is model predictive control (MPC). MPC has been combined with OPPs to control MV inverters connected to an electrical machine. This model predictive pulse pattern controller (MP^{3}C) achieves near optimal steady-state performance and fast transient control. MP^{3}C is, however, restricted to first-order systems, such as the simple inductive load corresponding to a machine. A general MP^{3}C method for higher-order systems is preferable, which allows for control of a variety of applications with OPPs.

1.2 Outline and Contributions

The contributions of this thesis are divided in two parts. The theory required for the derivations in this thesis is provided in Chapter 2. Chapter 3 investigates the impact of the implicitly imposed assumptions on OPPs for a selection of three-level waveforms. In Chapter 4, a general MP^{3}C method for a grid-connected MV converter with an additional LC filter is designed. Chapter 5 concludes the thesis with a discussion of the presented results and an outlook for future research.

The main contributions of this thesis are the following ones:

- The generalisation of the three-level OPP problem by relaxing the commonly made assumptions. These assumptions comprise non-negative switch positions in the positive half-wave of the fundamental period, quarter-wave symmetry and half-wave symmetry.
- The computation and performance evaluation of OPPs with low pulse numbers and different imposed symmetries.
- The design of a generalised MPC scheme based on a novel approach to transform the OPP from the continuous-time to the discrete-time domain.
- The performance evaluation of the proposed controller during steady-state operations and transients.

Chapter 2

Theoretical Background

In this chapter, the fundamental principles and basic concepts required for this thesis are summarised.

2.1 Neutral-point-clamped Converter

The most popular inverter topology for medium-voltage (MV) applications, i.e. power ratings above 1 MVA, is the three-level neutral-point-clamped (NPC) converter [1]. Fig. 3.1 shows the NPC converter with its three phase legs. Each phase leg consists of four active switches paired with four freewheeling diodes, and two clamping diodes. The neutral point (N) is created by the two dc-link capacitors C_{dc}. At the terminal of each phase leg, the three-level phase voltage

$$v_{cp}(t) = \frac{V_{\mathrm{dc}}}{2} u_p(t) \tag{2.1}$$

is generated, where V_{dc} is the dc-link voltage, $u_p(t) \in \mathcal{U}$ is the switching signal in this phase with $\mathcal{U} = \{-1, 0, 1\}$, and p denotes the phase with $p \in \{a, b, c\}$.

The three phase voltages sum up to the *common-mode voltage*

$$v_0(t) = \frac{1}{3}\big(v_{ca}(t) + v_{cb}(t) + v_{cc}(t)\big). \tag{2.2}$$

The common-mode voltage affects the balance of the neutral point potential in the NPC converter and might harm the bearings of a connected machine. In this thesis, we neglect the influence of the common-mode voltage on the neutral point potential and assume a constant neutral point potential for simplification. Nevertheless, the common-mode voltage is to be kept as small as possible. We also assume the dc-link voltage V_{dc} to be constant.

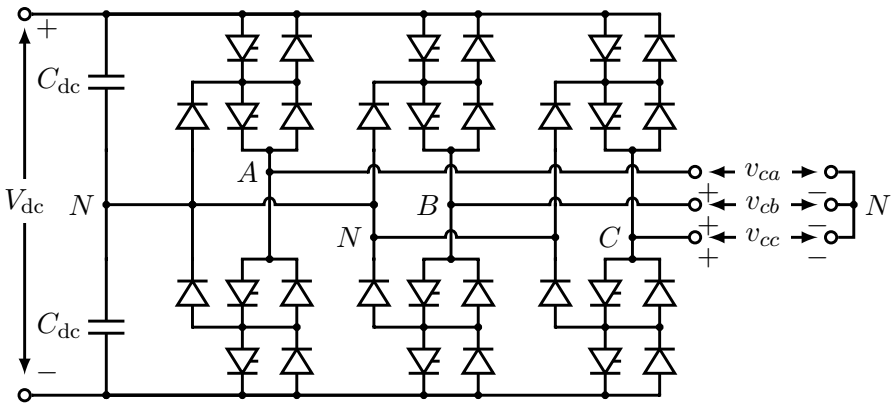

Figure 2.1: Three-level NPC converter.

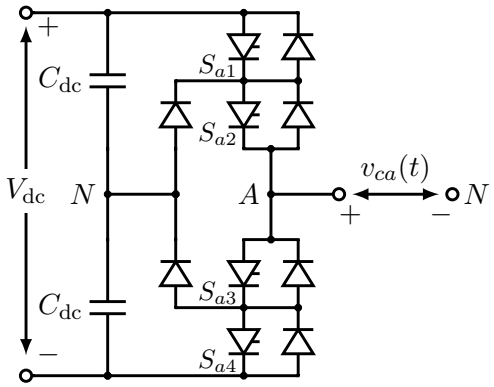

Figure 2.2: Phase leg of phase a of the NPC inverter.

Switch position	Active switches				Phase voltage
u_p	S_{p1}	S_{p2}	S_{p3}	S_{p4}	v_{cp}
-1	0	0	1	1	$-\frac{V_{\mathrm{dc}}}{2}$
0	0	1	1	0	0
1	1	1	0	0	$\frac{V_{\mathrm{dc}}}{2}$

Table 2.1: Switching states and resulting phase voltage for the three-level NPC inverter.

Switching Frequency Consider the single phase leg shown in Fig. 2.2. The four active switches are labelled with S_{a1}, S_{a2}, S_{a3} and S_{a4}. To generate the three voltage levels, always two switches in the phase leg are conducting, i.e. are active. For each output level, the active (1) and inactive (0) switches in the phase leg are stated in Table 2.1 together with the equivalent switch position of the switching signal. Switching by more than one level up or down is generally prohibited owing to the risk of a short circuit and an imbalance of the blocking voltages. This means that switching from -1 to 1 is only permitted via an intermediate zero switch position. As a result, at each switching transition, one semiconductor switch is turned on and another one is turned off.

With this, the *averaged* switching frequency of one semiconductor switch f_{sw} can be directly related to the number of on/off transitions of that semiconductor within one fundamental period. The switching frequency is used as a measure for the switching effort. Due to the particularly high switching losses in MV converters, the maximum switching frequency is limited typically between $100\,\mathrm{Hz}$ and $500\,\mathrm{Hz}$.

Total Demand Distortion The switched converter voltages consist of the desired fundamental component and the undesired harmonic component. The voltage harmonics generate harmonic distortions in the currents of the connected load, either the stator currents of a machine or grid currents. A figure of merit to express the harmonic distortion in the current is the *total demand distortion* (TDD). The current TDD is defined as the square root of the sum of the squared current harmonics $\hat{i}_n$ related to the nominal current

$$I_{\mathrm{TDD}} = \frac{1}{\sqrt{2} I_{\mathrm{nom}}} \sqrt{\sum_{n \neq 1} \left(\hat{i}_n\right)^2}, \tag{2.3}$$

where I_{nom} is the rms value of the nominal or rated current.

2.2 Per Unit System

It is common practice to normalise the electrical quantities in an electrical system such that they are equal to *one* when operating at the rated conditions of the connected load. In this so-called *per unit* system, each parameter and variable is normalised with respect to its base quantity. These are derived from the three primary base quantities:

- The peak amplitude of the rated phase voltage $V_B = \sqrt{\frac{2}{3}} V_R$,
- the peak amplitude of the rated phase current $I_B = \sqrt{2} I_R$, and
- the rated angular frequency $\omega_B = \omega_{sR}$.

Note that the rated parameters are rms values and that the rated voltage is a line-to-line voltage. Considering a drive system with an electrical machine, the rated machines parameters are used as base quantities. For a grid-connected converter, the rated parameters are the quantities on the secondary side of the transformer. From the primary base quantities, we can derive the base impedance and the base inductance as

$$Z_B = \frac{V_B}{I_B} \qquad \text{and} \qquad L_B = \frac{Z_B}{\omega_B},$$

respectively.

2.3 Optimal Pulse Width Modulation

Pulse width modulation (PWM) is used to generate the switching signals for the converter. The discrete-valued switching signal is composed of pulses with variable width, which are chosen such that the required fundamental amplitude is achieved, i.e. the *modulation index* m.

One popular scheme to generate the switching signals is *carrier-based* PWM. The switching signal directly results from the comparison of a *modulating* signal, with the fundamental frequency f_1, with one or more *carrier* signals with higher frequency f_c. A high ratio of the carrier to fundamental frequency, i.e. f_c/f_1, ensures low harmonic distortions in the load currents but in turn requires a high switching frequency. Main advantages of carrier-based PWM are its easy implementation and straightforward use with classic control schemes such as field-oriented control [2, 3]. However, applying carrier-based PWM to MV inverters demands very low carrier to fundamental frequency ratios ($f_c/f_1 < 11$) when operating at nominal conditions. This leads to high amplitudes of the current harmonics [4]. Another disadvantage is the restriction of the switching transitions to the half-intervals of the carrier signal. As a result, the achievable harmonic performance is limited and the harmonic spectrum cannot be well shaped.

In order to achieve high quality converter output currents with low switching to fundamental frequency ratios, *optimal* PWM schemes are used [5]. In optimal or programmed PWM, steady-state conditions are assumed. This allows for precise optimisation of the switching signal over one fundamental period, which is typically carried out in an *offline* computation [6]. The computation is based on the exact representation of the harmonics as functions of the *switching angles*, i.e. the switching times, by means of Fourier analysis. The two available optimal PWM strategies are selective harmonic elimination (SHE) and optimised pulse patterns (OPPs), sometimes also referred to as synchronous optimal PWM [7]. The terminology and basic optimal PWM problems are introduced in this section.

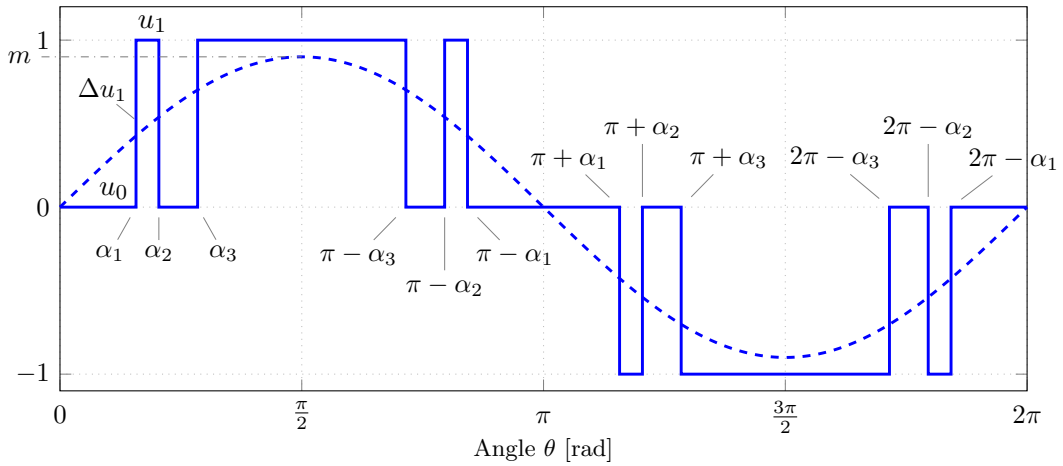

Figure 2.3: Single-phase pulse pattern (solid line) over one fundamental period. The amplitude of the fundamental component (dashed line) is the modulation index m.

2.3.1 Pulse Pattern

For the offline switching signal computation, symmetry between the three phases is assumed. As a result, the switching signals in phases a, b and c correspond to the single-phase switching signal phase-shifted by $0°$, $120°$ and $240°$, respectively. We refer to the single-phase switching signal over one fundamental period as the *pulse pattern* $u(\theta)$. An example is shown in Fig. 2.3.

Let k be the number of switching transitions within one fundamental period $T_1 = 1/f_1$ in one phase. Table 2.1 implies that within one fundamental period each of the four semiconductors in a phase leg is switched $k/4$ times on average. The average switching frequency of a single semiconductor directly follows as $f_{\text{sw}} = k/4\, f_1$. With this, we define the *pulse number* d as the ratio of the switching frequency f_{sw} of a single semiconductor switch in a phase leg to the fundamental frequency f_1 of the switching signal

$$\frac{f_{\text{sw}}}{f_1} = \frac{k}{4} = d. \tag{2.4}$$

It is common practise to impose quarter-wave and half-wave symmetry on the pulse pattern, i.e.

$$u(\pi - \theta) = u(\theta) \tag{2.5}$$
$$u(\pi + \theta) = -u(\theta). \tag{2.6}$$

Moreover, for three- and multi-level pulse patterns, *unipolar* switch positions are assumed. This means that the polarity of the switch positions corresponds to that of the respective fundamental half-wave: there are only non-negative switch positions, $\mathcal{U}^* = \{0, 1\}$, in the positive half-wave of the fundamental period and vice versa.

As a result of these assumptions, only the switching angles and switch positions in the first quarter of the fundamental period need to be determined in the pulse pattern computation. For the three-level converter, one quarter of the number of switching transitions in the fundamental period equals the pulse number, see (2.4). We can thus define the pulse pattern by the d switching angles $\alpha_i \in \left[0, \frac{\pi}{2}\right]$ with $i \in \{1, \ldots, d\}$, and the $d + 1$ switch positions $u_i \in \mathcal{U}^*$ with

$i \in \{0, 1, \ldots, d\}$. This gives the piece wise constant function

$$u(\theta) = \begin{cases} u_0 & 0 \leq \theta \leq \alpha_1 \\ u_1 & \alpha_1 \leq \theta \leq \alpha_2 \\ \vdots & \\ u_{d-1} & \alpha_{d-1} \leq \theta \leq \alpha_d \\ u_d & \alpha_d \leq \theta \leq \frac{\pi}{2}. \end{cases} \tag{2.7}$$

At each switching angle α_i, a specific switching transition occurs, which is defined as

$$\Delta u_i = u_i - u_{i-1}, \tag{2.8}$$

with $i \in \{1, \ldots, 4d\}$. We can use (2.8) to find the ith switch position as the sum of the preceding switching transitions added to the initial switch position

$$u_i = u_0 + \sum_{j=1}^{i} \Delta u_j, \tag{2.9}$$

where u_0 is the initial switch position. Recall that NPC inverters are allowed to switch only by one level up or down. Therefore, the switching transitions are restricted to $\Delta u_i = \{-1, 1\}$. This combined with the unipolar switch position restriction $u_i \in \mathcal{U}^+$ leads to a fixed sequence of switch positions in the first quarter-wave of the fundamental period $U = [0\ 1\ 0\ 1\ 0 \ldots]$. The sequence of switching transitions directly follow as

$$\Delta u_i = (-1)^{i-1}, \qquad \text{with} \quad i = 1, \ldots, d. \tag{2.10}$$

Fourier Analysis The pulse pattern $u(\theta)$ is a 2π-periodic function, which can be represented by the Fourier series as

$$u(\theta) = \frac{a_0}{2} + \sum_{n=1}^{\infty} \big(a_n \cos(n\theta) + b_n \sin(n\theta)\big), \tag{2.11}$$

where n is the harmonic order with $n \in \mathbb{N}$, and the Fourier coefficients a_n and b_n are

$$a_n = \frac{1}{\pi} \int_0^{2\pi} u(\theta) \cos(n\theta)\, \mathrm{d}\theta, \quad \text{for } n \geq 0\,, \text{ and} \tag{2.12a}$$

$$b_n = \frac{1}{\pi} \int_0^{2\pi} u(\theta) \sin(n\theta)\, \mathrm{d}\theta, \quad \text{for } n \geq 1\,. \tag{2.12b}$$

Each harmonic can be written as

$$u_n(\theta) = \hat{u}_n \cos(n\theta - \phi_n), \tag{2.13}$$

where the amplitude $\hat{u}_n$ and phase ϕ_n of the nth switching signal harmonic follow from the Fourier coefficients (2.12) as

$$\hat{u}_n = \sqrt{a_n^2 + b_n^2} \tag{2.14a}$$

$$\tan \phi_n = \frac{b_n}{a_n}. \tag{2.14b}$$

This leads to the alternative Fourier series representation

$$u(\theta) = \frac{a_0}{2} + \sum_{n=1}^{\infty} \hat{u}_n \cos(n\theta - \phi_n). \tag{2.15}$$

For the three-level switching signal (2.7), Fourier series expansion leads to the compact representation

$$u(\theta) = \sum_{n=1}^{\infty} \hat{u}_n \sin(n\theta) \tag{2.16a}$$

$$\hat{u}_n = \begin{cases} 0, & n = 2, 4, 6, \dots \\ \dfrac{4}{\pi n} \displaystyle\sum_{i=1}^{d} \Delta u_i \cos(n\alpha_i), & n = 1, 3, 5, \dots \end{cases} \tag{2.16b}$$

Note that due to the imposed symmetry, the switching signal is an odd function. As a result all Fourier coefficients a_n and all b_n for even orders are zero. For a detailed derivation of (2.16), the interested reader is referred to [8, Ch. 3 Appendix A].

The expression (2.16) forms the basis of the optimal PWM methods. Due to the fixed sequence of switching transitions (2.10), the harmonic components in the switching signal only depend on the d switching angles α_i in the first quarter of the fundamental period.

Three-phase Pulse Pattern From the harmonic representation (2.13) follows that a phase shift of the pulse pattern translates to phase shifts of the harmonics as follows

$$u_n(\theta - \varphi) = \hat{u}_n \cos(n\theta - n\varphi - \phi_n). \tag{2.17}$$

Note that φ is the particular phase shift of phases a, b and c. The phase shift in phase b, $\varphi = 2\pi/3$, results in the phase shift $n2\pi/3$ for the nth harmonic in phase b. Thus, triplen-order harmonics, i.e. integer multiples of three with $n = 3, 6, 9, \dots$, are again in phase with the harmonics of the pulse pattern in phase a. The same applies to phase c. Note that ϕ_n is the phase shift of the nth harmonic, which is the same in each phase.

The switching signal harmonics u_n directly correspond to the phase voltage harmonics v_n, i.e. $v_n = \frac{V_{\mathrm{dc}}}{2} u_n$. Consequently, all triplen-order voltage harmonics are in phase. For a balanced three-phase load with a floating star point, these voltage harmonics cancel each other in the line-to-line voltages and do not drive a harmonic current. Thus, we consider only the odd, non-triplen harmonic orders, $n = 5, 7, 11, \dots$, in the pulse pattern computation.

2.3.2 Selective Harmonic Elimination

In 1964, SHE originated with the computation of a two-level waveform, which eliminates two lower order harmonics in the load voltage [9]. This technique was further developed in [10] and [11] to allow elimination of any number of harmonics by formulating an algebraic system of equations.

For example, consider the three-level waveform with d switching angles in the first quarter of the fundamental, which are the degrees of freedom. With the help of (2.16), the first $d - 1$ harmonics are set to zero, and the fundamental component is set to the modulation index. Solving the system of equations for a varying modulation index yields multiple solution sets of switching angles.

The switching angles in each set are continuous functions of the modulation index, which allows a straightforward implementation with linear controllers. The challenge in SHE is the identification of all solution sets together with the subsequent selection of the optimal set for the particular application. A review of such techniques is beyond the scope of this thesis. The interested reader is referred to [12], [13] and [14] for approaches to obtain all solution sets in case of a two-, three- and multi-level inverter, respectively.

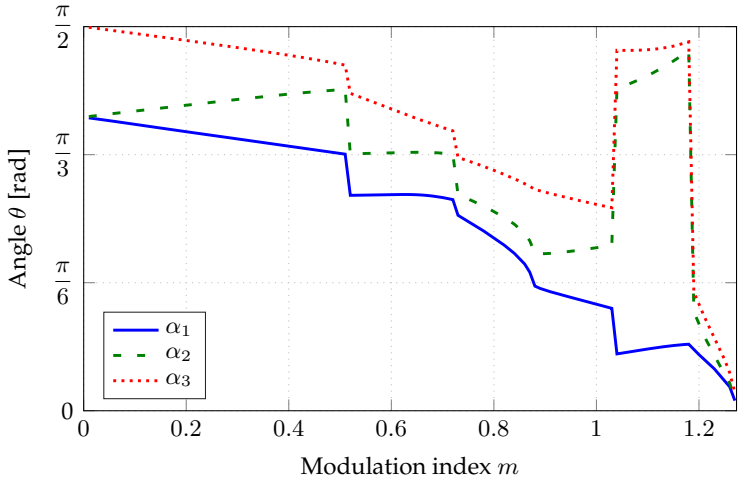

Figure 2.4: Optimal switching angles for a three-level converter with $d = 3$.

The practical implementation of these pulse patterns is done by look-up tables. The offline computed switching angles are stored for all required modulation indices and various numbers of switching angles. Online, the appropriate switching angles are then selected, depending on the reference operating point, and the three-phase switching signal is generated and applied to the inverter.

2.3.3 Optimised Pulse Patterns

OPPs were first proposed in 1977 for two-level inverters [15]. Similar to SHE, expressions for the harmonics are derived by Fourier analysis as functions of the d switching angles (2.16). However, instead of completely eliminating a certain number of harmonics, a constrained optimisation problem is solved minimising the entire harmonic content in the switching signal [16]. An algorithm to solve the optimisation problem of three- and five-level OPPs is presented in [5] and [17], respectively.

For the three-level pulse pattern, the OPP optimisation problem is of the form

$$\underset{\alpha_i}{\text{minimise}} \quad J(\alpha_i) \tag{2.18a}$$

$$\text{subject to} \quad \frac{4}{\pi}\sum_{i=1}^{d} \Delta u_i \cos(\alpha_i) = m \tag{2.18b}$$

$$0 \leq \alpha_1 \leq \alpha_2 \leq \ldots \leq \alpha_d \leq \frac{\pi}{2}, \tag{2.18c}$$

with the d switching angles α_i, with $i \in \{1, \ldots, d\}$, as optimisation variables. For the objective function $J(\alpha_i)$, a performance criterion related to the unwanted effects of the switching signal harmonics is chosen. Most commonly, the TDD of the load current is adopted as objective function [6]. To ensure that the fundamental amplitude corresponds to the modulation index, the equality constraint (2.18b) is introduced. The inequality constraints (2.18c) ensure that the switching angles are in ascending order. A brief summary of the basic terminology of optimisation problems is given below in Section 2.4.

Solving the optimisation problem over the modulation range gives a unique set of switching angles that are optimal with regard to the chosen objective. For $d = 3$, the switching angles over the entire modulation range are shown in Fig. 2.4.

A major drawback of OPPs is the presence of discontinuities in the switching angles over the modulation range, see Fig. 2.4. This poses a challenge for the computation and control of OPPs.

2.4 Optimisation Problems

According to [18], an optimisation problem has the general form

$$\underset{\boldsymbol{x}}{\text{minimise}} \quad J(\boldsymbol{x}) \tag{2.19a}$$

$$\text{subject to} \quad g_i(\boldsymbol{x}) \leq 0 \qquad i = 1, \ldots, m \tag{2.19b}$$

$$h_j(\boldsymbol{x}) = 0 \qquad j = 1, \ldots, p \tag{2.19c}$$

with the *optimisation variable* $\boldsymbol{x} \in \mathbb{R}^{n_r}$. The goal is to minimise the *objective function* (or cost function) $J(\boldsymbol{x}) : \mathbb{R}^{n_r} \to \mathbb{R}$ while satisfying the *inequality* constraints $g_i(\boldsymbol{x}) : \mathbb{R}^{n_r} \to \mathbb{R}$ with $i = 1, \ldots, m$, and the *equality* constraints $h_j(\boldsymbol{x}) : \mathbb{R}^{n_r} \to \mathbb{R}$ with $j = 1, \ldots, p$. The inequality and equality constraints form the *feasible* set (or search space)

$$\mathcal{X} = \left\{ \boldsymbol{x} \in \mathbb{R}^{n_r} | g_i(\boldsymbol{x}) \leq 0,\ i = 1, \ldots, m,\ h_j(\boldsymbol{x}) = 0,\ j = 1, \ldots, p \right\}. \tag{2.20}$$

A point satisfying the inequality and equality constraints is called a *feasible point*. An optimisation problem is feasible if there exist at least one feasible point. Otherwise it is *infeasible*.

The *optimal value* J_{opt} is the lowest possible value of the objective function, which is attained by the *optimal solution* (or optimiser) $\boldsymbol{x}^*$, i.e. $J_{\text{opt}} = J(\boldsymbol{x}^*) \leq J(\boldsymbol{x})$ with $\boldsymbol{x}^* \in \mathcal{X}$ and for all feasible $\boldsymbol{x} \in \mathcal{X}$.

A feasible point $\boldsymbol{x}$ is *locally optimal* if it minimises $J(\boldsymbol{x})$ in a subset of the feasible set. A feasible point $\boldsymbol{x}$ it is *globally optimal* if it minimises $J(\boldsymbol{x})$ over the entire feasible set.

2.4.1 Convex Optimisation Problems

A special class of optimisation problems are *convex* optimisation problems. For their formulation, we require the definitions of a convex set and convex function.

A set $\mathcal{X}$ is *convex* if the line segment between any pair of points $\boldsymbol{x}, \boldsymbol{y} \in \mathcal{X}$ lies also in $\mathcal{X}$, i.e.

$$\lambda \boldsymbol{x} + (1 - \lambda)\boldsymbol{y} \in \mathcal{X} \quad \text{with} \quad \lambda \in [0, 1]\,. \tag{2.21}$$

A function $J(\boldsymbol{x}) : \mathbb{R}^{n_r} \to \mathbb{R}$ is *convex* if for all $\boldsymbol{x}, \boldsymbol{y} \in \mathbb{R}^{n_r}$ and $\lambda \in [0, 1]$, we have

$$J\big(\lambda \boldsymbol{x} + (1 - \lambda)\boldsymbol{y}\big) \leq \lambda J(\boldsymbol{x}) + (1 - \lambda) J(\boldsymbol{y}). \tag{2.22}$$

A convex optimisation problem is of the form

$$\underset{\boldsymbol{x}}{\text{minimise}} \quad J(\boldsymbol{x}) \tag{2.23a}$$

$$\text{subject to} \quad g_i(\boldsymbol{x}) \leq 0 \qquad i = 1, \ldots, m \tag{2.23b}$$

$$\boldsymbol{a}_j^T \boldsymbol{x} = \boldsymbol{b}_j \qquad j = 1, \ldots, p, \tag{2.23c}$$

where the objective function $J(\boldsymbol{x})$ and the inequality constraints $g_1, \ldots, g_m$ are convex, the equality constraints $h_j = \boldsymbol{a}_j^T \boldsymbol{x} - \boldsymbol{b}_j$ are affine, and the domain of the objective function is a convex set. As a result, also the feasible set is convex. The key feature of convex optimisation problems is that any locally optimal solution is also globally optimal.

The affine constraints can be gathered into matrix form: $\boldsymbol{A}\,\boldsymbol{x} = \boldsymbol{b}$, where $\boldsymbol{A} = \mathbb{R}^{p \times n_r}$ and $\boldsymbol{b} \in \mathbb{R}^p$.

2.4.2 Linear Optimisation Problems

If the objective function and the constraints are all affine functions, the problem is called a *linear program*, and it is formulated as

$$\begin{aligned} \underset{\boldsymbol{x}}{\text{minimise}} \quad & J(\boldsymbol{x}) = \boldsymbol{c}^T \boldsymbol{x} && \text{(2.24a)} \\ \text{subject to} \quad & \boldsymbol{G}\,\boldsymbol{x} \leq \boldsymbol{h} && \text{(2.24b)} \\ & \boldsymbol{A}\,\boldsymbol{x} = \boldsymbol{b}, && \text{(2.24c)} \end{aligned}$$

with $\boldsymbol{c} \in \mathbb{R}^{n_r}$, $\boldsymbol{G} = \mathbb{R}^{m \times n_r}$, $\boldsymbol{h} \in \mathbb{R}^m$, $\boldsymbol{A} = \mathbb{R}^{p \times n_r}$ and $\boldsymbol{b} \in \mathbb{R}^p$. Linear problems are always convex and can be solved efficiently.

2.4.3 Quadratic Optimisation Problems

A *quadratic program* (QP) is of the form

$$\begin{aligned} \underset{\boldsymbol{x}}{\text{minimise}} \quad & J(\boldsymbol{x}) = \frac{1}{2}\boldsymbol{x}^T \boldsymbol{H} \boldsymbol{x} + \boldsymbol{q}^T \boldsymbol{x} + r && \text{(2.25a)} \\ \text{subject to} \quad & \boldsymbol{G}\,\boldsymbol{x} \leq \boldsymbol{h} && \text{(2.25b)} \\ & \boldsymbol{A}\,\boldsymbol{x} = \boldsymbol{b}, && \text{(2.25c)} \end{aligned}$$

where the objective function is a quadratic function and $\boldsymbol{H} \in \mathbb{R}^{n_r \times n_r}$, $\boldsymbol{q} \in \mathbb{R}^{n_r}$, $\boldsymbol{G} = \mathbb{R}^{m \times n_r}$, $\boldsymbol{h} \in \mathbb{R}^m$, $\boldsymbol{A} = \mathbb{R}^{p \times n_r}$ and $\boldsymbol{b} \in \mathbb{R}^p$.

The QP is convex if and only if the Hessian matrix $\boldsymbol{H}$ is *positive semidefinite*, i.e. for all $\boldsymbol{x} \in \mathbb{R}^{n_r}$ it holds that

$$\boldsymbol{x}^T \boldsymbol{H} \boldsymbol{x} \geq 0. \tag{2.26}$$

The expression *if and only if* states that this is a necessary and sufficient condition. The matrix $\boldsymbol{H}$ is *positive definite* if

$$\boldsymbol{x}^T \boldsymbol{H} \boldsymbol{x} > 0 \tag{2.27}$$

for all non-zero $\boldsymbol{x} \in \mathbb{R}^{n_r}$.

Chapter 3

Symmetry Relaxation of Three-level Optimised Pulse Patterns

3.1 Introduction

The offline computation of switching patterns allows the precise shaping of their harmonic content, and thus enables the generation of high quality inverter outputs [19]. Assuming steady-state conditions, the switching signal over one fundamental period, i.e. the pulse pattern, is optimised.

For the derivation of an analytical expression of the harmonics, typically four assumptions are imposed on the switching signal:

1. Periodicity,
2. Half-wave symmetry,
3. Quarter-wave symmetry[1] and
4. Unipolar switch positions (in case of multi-level switching signals).

While the first assumption of periodicity is required to perform the Fourier analysis, the other three are imposed to simplify the problem and are justified only by intuition. The examination of the impact on the performance when relaxing these three assumptions is the objective of this chapter. To this end, a review of the existing literature and recent research on relaxation of these typically imposed assumptions is given in the remainder of this section for the two available offline PWM methods: selective harmonic elimination (SHE) and optimised pulse patterns (OPPs). In addition, the case study used throughout this chapter for the derivation and computation of the OPPs is introduced. Section 3.2 defines the general pulse pattern and provides an overview of the imposed symmetry assumptions and the resulting new types of pulse patterns. Moreover, the mathematical derivation of the harmonic content depending on the imposed symmetry conditions is presented. Section 3.3 derives the four resulting optimisation problems and Section 3.4 describes the general procedure to solve them. Features allowing successful and efficient solving of the optimisation problem are discussed as well. Finally in Section 3.5, OPPs with different imposed restrictions are computed and their performances are compared against each other.

[1] We refer to quarter-wave symmetry and half-wave symmetry as two independent concepts. This means that half-wave symmetry is not implied by quarter-wave symmetry. For example, a quarter-wave symmetric OPP without half-wave symmetry may be created for the case of a non-zero dc-offset.

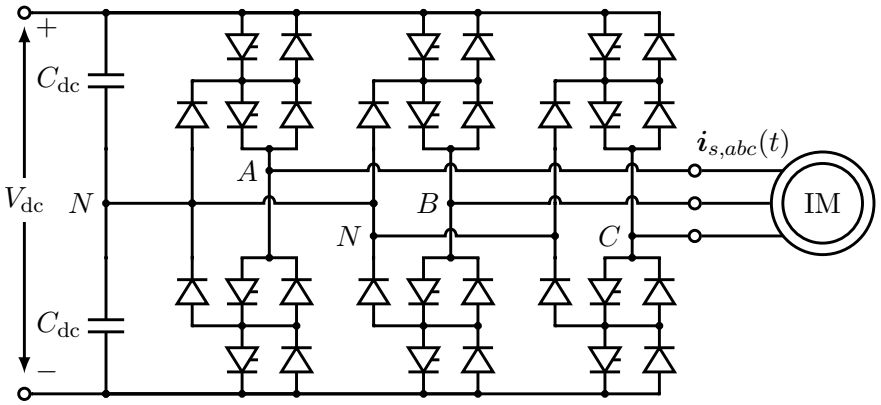

Figure 3.1: Medium-voltage drive system: Three-level NPC inverter connected to an induction machine (IM).

3.1.1 Literature Review

For the SHE problem, relaxing the quarter-wave symmetry assumption on the pulse pattern was first investigated in [20]. A formulation for the two-, three- and general multi-level SHE problem is presented, which allows one to find new half-wave symmetric pulse patterns. These solutions have been unattainable by the traditional quarter- and half-wave symmetric SHE problem. Comparison of these newly obtained solution sets against traditional solutions reveals a reduction of the overall harmonic distortion [21]. Further relaxation of half-wave symmetry is reported in [22] and experimentally verified with a five-level inverter. The number of attainable solutions when relaxing symmetry increases to infinity. Moreover, due to the additional degrees of freedom, the problem becomes more difficult to solve. This gives rise to new formulations and algorithms to solve the general SHE problem [23].

For the OPP problem, relaxation of the symmetry assumptions was investigated only recently in a small number of publications. In 2014, half-wave symmetric OPPs for the two-level inverter were computed with various numbers of switching angles [24], [25]. The obtained OPPs reduce the current TDD in a certain interval of the modulation range. Similar results were reported when taking into account the isotropy properties of a connected electrical machine [26]. Relaxing the quarter-wave symmetry assumption, the computed two-level OPPs achieve a reduction of up to $20\,\%$ of the current TDD for a specific interval of the modulation range. Symmetry relaxation of three- or multi-level OPPs has not been published yet. Furthermore, no literature could be found on OPPs with a relaxed unipolar switch position constraint, i.e. allowing negative switch positions in the positive half-wave of the fundamental period.

3.1.2 Medium-voltage Drive Case Study

The case study for the OPP computation is described in this section. We assume a three-level neutral-point-clamped (NPC) inverter connected to an induction machine as depicted in Fig. 3.1. The rated values of the drive system and the leakage inductance of the machine are given in Table 3.1.

When connecting an induction machine to the NPC inverter, the three-phase inverter voltages $\boldsymbol{v}_{c,abc} = [v_{ca}\ v_{cb}\ v_{cc}]^T$ drive the stator current $\boldsymbol{i}_{s,abc} = [i_{sa}\ i_{sb}\ i_{sc}]^T$ through the stator windings of the machine. For the OPP derivation, only the steady-state behaviour for harmonic frequencies is of interest. Thus, a harmonic model of the machine is derived, representing the machine solely as an inductive load with the leakage inductance L_σ

$$\boldsymbol{v}_{c,abc}(t) = L_\sigma \frac{\mathrm{d}\boldsymbol{i}_{s,abc}(t)}{\mathrm{d}t}. \tag{3.1}$$

Table 3.1: Parameters of NPC inverter connected to machine.

Parameter	Symbol	SI value
Rated line-to-line voltage	V_R	$3.3\,\mathrm{kV}$
Rated stator current	I_R	$2.12\,\mathrm{kA}$
Rated angular stator frequency	ω_{sR}	$2\pi 50\,\mathrm{rad/s}$
Dc-link voltage	V_{dc}	$5.2\,\mathrm{kV}$
Leakage inductance	L_σ	$0.73\,\mathrm{mH}$

Note that we neglected the stator resistance. Furthermore, an equal leakage inductance in all three phases is assumed.

Adopting the per unit system, we can derive the leakage reactance of the MV machine in per unit as

$$X_\sigma = \frac{L_\sigma}{L_B} = 0.255\,\mathrm{pu}.$$

The dc-link voltage in per unit is $V_{\mathrm{dc}} = 1.929\,\mathrm{pu}$.

3.2 Symmetry Relaxation

Relaxing one-by-one the assumptions of

1. unipolar switch positions,
2. quarter-wave symmetry and
3. half-wave symmetry

results in the definition of *four* types of three-level pulse patterns. Symmetry between the three phases remains, which allows us to consider only the single-phase switching signal $u(\theta)$.

3.2.1 Pulse Pattern Types

Quarter- and Half-wave Symmetric OPPs with Unipolar Switch Positions (QaHWS$^+$) The first type of pulse patterns corresponds to the traditional definition. Quarter- and half-wave symmetry and unipolar switch positions are imposed on the pulse pattern (2.7). As a result, the pulse pattern is defined by the switching angles and switch positions in the first quarter of the fundamental. An example is shown in Fig. 3.2a. In this type, only positive switch positions in the positive half-wave of the fundamental period are allowed $u_i \in \mathcal{U}^+$. Consequently, only the d switching angles in the first quarter of the fundamental period remain as optimisation variables $\alpha_i \in \left[0, \frac{\pi}{2}\right]$ with $i \in \{1, \ldots, d\}$. The number of switching transitions in each half-wave is restricted to even numbers. Thus, only integer pulse numbers $d \in \mathbb{N}$ are possible.

Quarter- and Half-wave Symmetric OPPs with Multipolar Switch Positions (QaHWS) Relaxing the restriction of unipolar switch positions allows for negative switch position in the positive half-wave of the fundamental period, i.e. *multipolar* switch positions. This gives the second type of OPPs, see for example in Fig. 3.2b. The quarter- and half-wave symmetry conditions require the initial switch position to be zero, i.e. $u_0 = 0$. As a result, the pulse pattern is fully defined by the d switching angles and d switch positions in the first quarter of the fundamental period. The domain of the set of switching angles remains the same. The switch positions, however, are now optimisation variables and defined as $u_i \in \mathcal{U}$ with $i \in \{1, \ldots, d\}$. The pulse number is still limited to integer numbers.

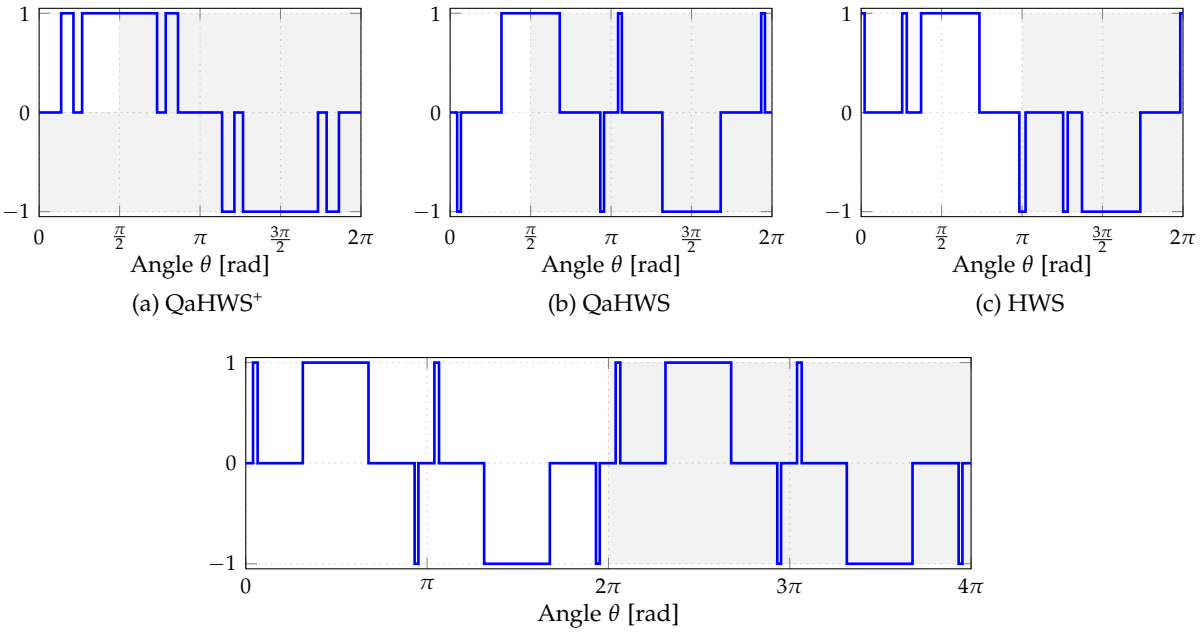

Figure 3.2: Pulse patterns of all four symmetry types. The search space of the corresponding optimisation problems is indicated by the white areas.

Half-wave Symmetric OPPs with Multipolar Switch Positions (HWS) For the third type of pulse patterns, quarter-wave symmetry is relaxed, see Fig. 3.2c. As a result, the number of elements in each set of optimisation variables, i.e. the number of switching angles and switch positions, increases to $2d$. Furthermore, the domain of the switching angles increases to half of the fundamental period, i.e. $\alpha_i \in [0, \pi]$. The domain of the switch positions remains the entire set of multipolar output levels $u_i \in \mathcal{U}$. From (2.6) follows that the first switch position in the second half-wave of the fundamental period corresponds to the initial switch position $u_{2d} = u_0$. The pulse number is still limited to integer numbers.

Full-wave Symmetric OPPs with Multipolar Switch Positions (FWS) Finally, relaxing half-wave symmetry results in the fourth type of OPPs, see the example in Fig. 3.2d. As the 2π periodicity persists, symmetry between each full-wave of the pulse pattern can be observed. We refer to such pulse patterns therefore as *full-wave* symmetric pulse patterns. Due to periodicity, the last switch position u_{4d} has to be equal to the initial switch position u_0, i.e. $u_{4d} = u_0$. Thus, the optimisation variables are the $4d$ switching angles $\alpha_i \in [0, 2\pi]$ with $i \in \{1, \ldots, 4d\}$, and the $4d$ switch positions $u_i \in \mathcal{U}$ with $i \in \{1, \ldots, 4d\}$. The number of switching transitions in one fundamental period is restricted to an even number. It follows that the number of the switching transitions divided by two is an integer number; this implies $4d/2 = 2d \in \mathbb{N}$. Thus, for full-wave symmetric pulse patterns, the pulse numbers can be *non-integer* numbers $d \in \{1, 1.5, 2, 2.5, \ldots\}$.

3.2.2 Harmonic Analysis

The OPP optimisation problem is based on the representation of the harmonics as functions of the switching angles and the switch positions. By applying the Fourier series expansion, we derive analytical expressions for the harmonic amplitudes in each of the previously defined pulse pattern types. In Fig. 3.3, the specific characteristics of all four OPP types are summarised.

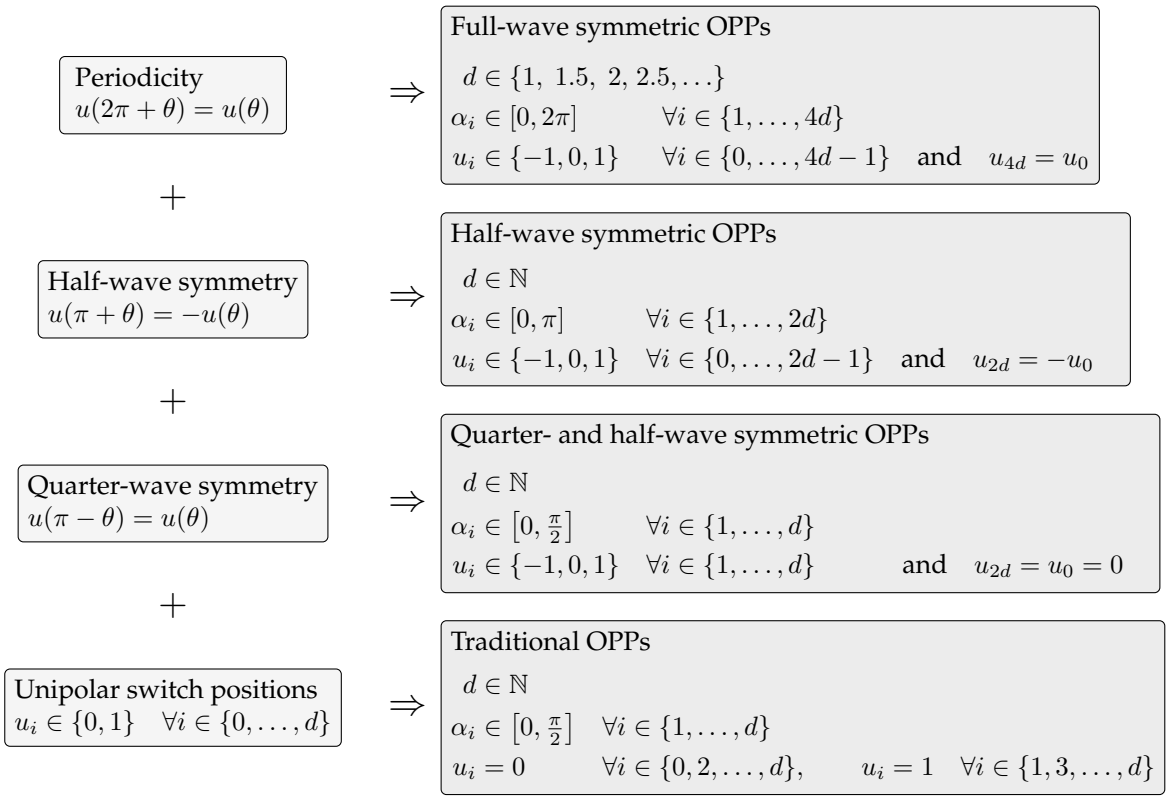

Figure 3.3: Overview of the typically imposed assumptions and the resulting characteristics of the pulse pattern types.

Consider that the relaxed symmetry types are defined by additional restrictions on the full-wave symmetric OPP. Thus, we can derive the Fourier coefficients for the full-wave symmetric OPP first and then simplify the derivation by imposing the symmetry assumptions. A detailed derivation for each type showing the applied simplification steps is given in Appendix A. The derived expressions are summarised in Table 3.2.

Full-wave Symmetry The Fourier coefficients for pulse patterns with full-wave symmetry are given in (3.2) in Table 3.2. The derived expressions reveal that the full-wave symmetric pulse pattern contains non-zero harmonics at integer orders $n \in \mathbb{N}$ and variable phase shifts due to the existence of both Fourier coefficients a_n and b_n. The Fourier coefficient a_0 represents a possible dc-offset.

Half-wave Symmetry Imposing half-wave symmetry, the expressions for the Fourier coefficients are given by (3.3) in Table 3.2. We see that half-wave symmetric pulse patterns consist of only odd numbered harmonics with various phase shifts. They have no dc-offset, due to $a_0 = 0$.

Quarter- and Half-wave Symmetry With quarter- and half-wave symmetry imposed, the derivation of the Fourier coefficients is further simplified and results in the well-known expressions for the traditional pulse patterns given in (3.4) in Table 3.2. For a detailed derivation, the interested reader is referred to [8, Ch. 3 Appendix A]. It is clear from the stated expressions that in the quarter- and half-wave symmetric pulse pattern the harmonics for even orders are zero. Additionally, the zero a_n Fourier coefficients turns each of the functions for the harmonics in (2.13) into a sine wave with a phase shift ϕ_n of $0°$ or $180°$.

Full-wave symmetry

$$a_n = \begin{cases} 2u_0 - \dfrac{1}{\pi}\displaystyle\sum_{i=1}^{4d} \Delta u_i \alpha_i, & n = 0 \\ -\dfrac{1}{\pi n}\displaystyle\sum_{i=1}^{4d} \Delta u_i \sin(n\alpha_i), & n = 1, 2, 3, \dots \end{cases} \qquad b_n = \frac{1}{\pi n}\sum_{i=1}^{4d} \Delta u_i \cos(n\alpha_i), \quad n = 1, 2, 3, \dots \tag{3.2}$$

Half-wave symmetry

$$a_n = \begin{cases} 0, & n = 0, 2, 4, \dots \\ -\dfrac{2}{\pi n}\displaystyle\sum_{i=1}^{2d} \Delta u_i \sin(n\alpha_i), & n = 1, 3, 5, \dots \end{cases} \qquad b_n = \begin{cases} 0, & n = 2, 4, 6, \dots \\ \dfrac{2}{\pi n}\displaystyle\sum_{i=1}^{2d} \Delta u_i \cos(n\alpha_i), & n = 1, 3, 5, \dots \end{cases} \tag{3.3}$$

Quarter- and half-wave symmetry

$$a_n = 0, \quad n = 0, 1, 2, \dots \qquad b_n = \begin{cases} 0, & n = 2, 4, 6, \dots \\ \dfrac{4}{\pi n}\displaystyle\sum_{i=1}^{d} \Delta u_i \cos(n\alpha_i), & n = 1, 3, 5, \dots \end{cases} \tag{3.4}$$

Table 3.2: Fourier coefficients a_n and b_n when imposing full-wave symmetry, half-wave symmetry, or quarter- and half-wave symmetry on the pulse pattern.

induca

3.3 Optimisation Problem

3.3.1 Objective Function

The total demand distortion (TDD) of the current is adopted as objective function for the optimisation problem.

Consider the inverter system presented in Section 3.1.2 consisting of a three-level NPC inverter connected to an induction machine. In this case, the OPPs are computed for minimal harmonic distortion in the stator current. Recall that the derived harmonic model represents the machine as a purely inductive load. With this we can directly relate the nth stator current harmonic $\hat{i}_n$ to the nth inverter voltage harmonic $\hat{v}_n$

$$\hat{i}_n = \frac{\hat{v}_n}{n\omega_1 X_\sigma}, \tag{3.5}$$

where all quantities are in per unit, X_σ is the leakage reactance of the induction machine and ω_1 is the angular fundamental frequency. The voltage harmonics result from scaling the pulse pattern harmonics $\hat{u}_n$ with half the dc-link voltage V_{dc} according to (2.1). Substituting (3.5) and (2.1) into the definition of the current TDD (2.3) leads to

$$I_{\text{TDD}} = \frac{1}{\sqrt{2} I_{\text{nom}} \omega_1 X_\sigma} \frac{V_{\text{dc}}}{2} \sqrt{\sum_{n \neq 1} \left(\frac{\hat{u}_n}{n} \right)^2}, \tag{3.6}$$

which gives the current TDD as a function of the pulse pattern harmonics.

We can write (3.6) as $I_{\text{TDD}} = c\sqrt{J}$, where c is a constant factor depending only on machine and inverter parameters, and J is a function of the pulse pattern. Thus, we choose as objective function

$$J = \sum_{n \neq 1} \left(\frac{\hat{u}_n}{n} \right)^2, \tag{3.7}$$

which is the sum of the squared pulse pattern harmonics weighted with the harmonic order. For an inductive load, minimising the objective function (3.7) consequently minimises the harmonic distortion in the current.

As explained in Section 2.3.1, in a symmetric three-phase system with a floating star point, triplen-order voltage harmonics, i.e. integer multiples of three, are in phase. Voltage harmonics in phase do not drive a harmonic current, which implies that the triplen-order current harmonics are zero. Therefore, the triplen-order switching signal harmonics are omitted in the objective function and only the non-triplen orders, $n = 2, 4, 5, 7, 8, 10 \ldots$, are considered. This allows us to write the objective function as

$$J = \sum_{n=2,4,5,7,\ldots} \frac{a_n^2 + b_n^2}{n^2}, \tag{3.8}$$

where we have substituted the pulse pattern harmonic amplitudes by the Fourier coefficients according to (2.14a).

3.3.2 Constraints

Constraints in the optimisation problem can be divided in two categories. The first one includes all constraints that relate to the fundamental component; the second one relates to constraints, which are directly imposed on the optimisation variables. The former set of constraints ensures that the inverter generates the required output voltage to drive the exact reference stator current. The latter avoids infeasible switch positions. With respect to the Fourier representation of the switching signal (2.15), the constraints for the general OPP problem are

- The dc-component of the OPP is zero, i.e. $a_0 = 0$;
- The phase of the fundamental component is $\phi_1 = \frac{\pi}{2}$, i.e. $a_1 = 0$;
- The amplitude of the fundamental component $\hat{u}_1$ equals the modulation index,i.e. $b_1 = m$;
- The switching angles are sorted in an ascending order $\alpha_i \leq \alpha_{i+1}$;
- The switching transitions are limited to $\Delta u_i \pm 1$; and
- The switch positions are restricted to the set of feasible output levels of the inverter $u_i \in \mathcal{U}$.

3.3.3 Specific Optimisation Problems

With this, the optimisation problems for the four pulse pattern types can be derived for a given pulse number d and modulation index m.

Full-wave Symmetric OPPs with Multipolar Switch Positions By inserting the Fourier coefficients (3.2) derived in the previous section into the objective function (3.8) and imposing the above listed constraints, we formulate the following general optimisation problem for 2π-periodic three-level OPPs

$$\underset{A_F,U_F}{\text{minimise}} \quad \sum_{n=2,4,5,\ldots} \left(\frac{1}{\pi n^2}\sum_{i=1}^{4d}\Delta u_i \sin(n\alpha_i)\right)^2 + \left(\frac{1}{\pi n^2}\sum_{i=1}^{4d}\Delta u_i \cos(n\alpha_i)\right)^2 \tag{3.9a}$$

$$\text{subject to} \quad 2u_0 - \frac{1}{\pi}\sum_{i=1}^{4d}\Delta u_i\alpha_i = 0 \tag{3.9b}$$

$$-\frac{1}{\pi}\sum_{i=1}^{4d}\Delta u_i \sin(\alpha_i) = 0 \tag{3.9c}$$

$$\frac{1}{\pi}\sum_{i=1}^{4d}\Delta u_i \cos(\alpha_i) = m \tag{3.9d}$$

$$0 \leq \alpha_1 \leq \alpha_2 \leq \ldots \leq \alpha_{4d} \leq 2\pi \tag{3.9e}$$

$$\Delta u_{i+1} = u_{i+1} - u_i \in \{-1, 1\} \tag{3.9f}$$

$$u_i \in \{-1, 0, 1\}, \qquad \forall\, i \in \{0, \ldots, 4d-1\}. \tag{3.9g}$$

The two sets of optimisation variables are the $4d$ switching angles $A_F = [\alpha_1\, \alpha_2 \ldots \alpha_{4d}]^T$ and switch positions $U_F = [u_0\, u_1 \ldots u_{4d-1}]^T$ within one fundamental period. The minimum number of optimisation variables in each set is 4, and the minimum pulse number is $d = 1$ for full-wave symmetric three-level OPPs.

Half-wave Symmetric OPPs with Multipolar Switch Positions For the half-wave symmetric OPP problem, the optimisation variables are the switching angles and switch positions in the first half of the fundamental period. Thus, the two sets consist of $2d$ elements each: The switching angles $A_H = [\alpha_1\, \alpha_2 \ldots \alpha_{2d}]^T$ and the switch positions $U_H = [u_0\, u_1 \ldots u_{2d-1}]^T$. Recall that by definition, the dc-offset of half-wave symmetric OPPs is zero, and that only odd order harmonics exist. Consequently, we may drop the constraint on the dc-offset and consider only odd, non-triplen order harmonics in the objective function, $n = 5, 7, 11, 13, \ldots$. With this, the following optimisation problem for half-wave symmetric OPPs is derived

$$\underset{A_H,U_H}{\text{minimise}} \quad \sum_{n=5,7,11,\ldots} \left(\frac{2}{\pi n^2}\sum_{i=1}^{2d}\Delta u_i \sin(n\alpha_i)\right)^2 + \left(\frac{2}{\pi n^2}\sum_{i=1}^{2d}\Delta u_i \cos(n\alpha_i)\right)^2 \tag{3.10a}$$

$$\text{subject to} \quad -\frac{2}{\pi}\sum_{i=1}^{2d}\Delta u_i \sin(\alpha_i) = 0 \tag{3.10b}$$

$$\frac{2}{\pi}\sum_{i=1}^{2d}\Delta u_i \cos(\alpha_i) = m \tag{3.10c}$$

$$0 \leq \alpha_1 \leq \alpha_2 \leq \ldots \leq \alpha_{2d} \leq \pi \tag{3.10d}$$

$$\Delta u_{i+1} = u_{i+1} - u_i \in \{-1, 1\} \tag{3.10e}$$

$$u_i \in \{-1, 0, 1\}, \qquad \forall\, i \in \{0, \ldots, 2d-1\}. \tag{3.10f}$$

Quarter- and Half-wave Symmetric OPPs with Multipolar Switch Positions The two sets of optimisation variables reduce each to d elements for the quarter- and half-wave symmetric OPP problem with multipolar switch positions. Recall that the initial switch position is restricted to zero. Furthermore, Fourier series expansions showed that the phase shifts of the pulse pattern harmonics are either $0°$ or $180°$. Thus, when setting the fundamental amplitude to m, the phase shift of the fundamental component is always $0°$ and the constraint on Fourier coefficient a_1 may be dropped, leading to

$$\underset{A_Q, U_Q}{\text{minimise}} \quad \sum_{n=5,7,11,\ldots} \left(\frac{4}{\pi n^2} \sum_{i=1}^{d} \Delta u_i \cos(n\alpha_i) \right)^2 \tag{3.11a}$$

$$\text{subject to} \quad \frac{4}{\pi} \sum_{i=1}^{d} \Delta u_i \cos(\alpha_i) = m \tag{3.11b}$$

$$0 \leq \alpha_1 \leq \alpha_2 \leq \ldots \leq \alpha_d \leq \frac{\pi}{2} \tag{3.11c}$$

$$\Delta u_{i+1} = u_{i+1} - u_i \in \{-1, 1\} \tag{3.11d}$$

$$u_i \in \{-1, 0, 1\}, \qquad \forall\, i \in \{1, \ldots, d\}, \tag{3.11e}$$

where $A_Q = [\alpha_1\, \alpha_2 \ldots \alpha_d]^T$ and $U_Q = [u_1\, u_2 \ldots u_d]^T$.

Quarter- and Half-wave Symmetric OPPs with Unipolar Switch Positions For completeness, we repeat here the traditional, quarter- and half-wave symmetric three-level OPP problem. Recall that only the switching angles in the first quarter of the fundamental period are optimisation variables $A_{uQ} = [\alpha_1\, \alpha_2 \ldots \alpha_d]^T$. The sequence of switch positions is fixed to $U_{uQ} = [0\,1\,0\,1\,0\ldots]^T$. This allows us to derive the expression for the switching transitions $\Delta u_i = (-1)^{i-1}$ with $i \in \{1, \ldots, d\}$, which we use to insert in following OPP optimisation problem

$$\underset{A_{uQ}}{\text{minimise}} \quad \sum_{n=5,7,11,\ldots} \left(\frac{4}{\pi n^2} \sum_{i=1}^{d} \Delta u_i \cos(n\alpha_i) \right)^2 \tag{3.12a}$$

$$\text{subject to} \quad \frac{4}{\pi} \sum_{i=1}^{d} \Delta u_i \cos(\alpha_i) = m \tag{3.12b}$$

$$0 \leq \alpha_1 \leq \alpha_2 \leq \ldots \leq \alpha_d \leq \frac{\pi}{2}. \tag{3.12c}$$

3.3.4 Properties

The constraints in each optimisation problem form the *feasible* set for the optimisation variables, i.e. the search space of the optimisation problem. For example, in case of the general full-wave symmetric OPP problem, the feasible set for the switching angles is a subset of the Euclidean space $\mathbb{R}^{4d}$. The feasible set for the switch positions is a subset of the integer set $\mathcal{U}^{4d}$. Two particular properties of these OPP optimisation problems require closer examination.

First, the trigonometric terms in the objective functions and in the constraints turn the OPP problems into *non-convex* optimisation problems. In particular, the trigonometric terms lead to multiple *local* minima in the search space. For such non-convex optimisation problems, there exists no straightforward algorithm for solving it. Thus, solving the optimisation problem is often a challenging and time consuming process, in particular when the number of degrees of freedom is high. In most cases, applying local optimisation methods, such as gradient-based algorithms, in combination with a large number of initial values, distributed within the search

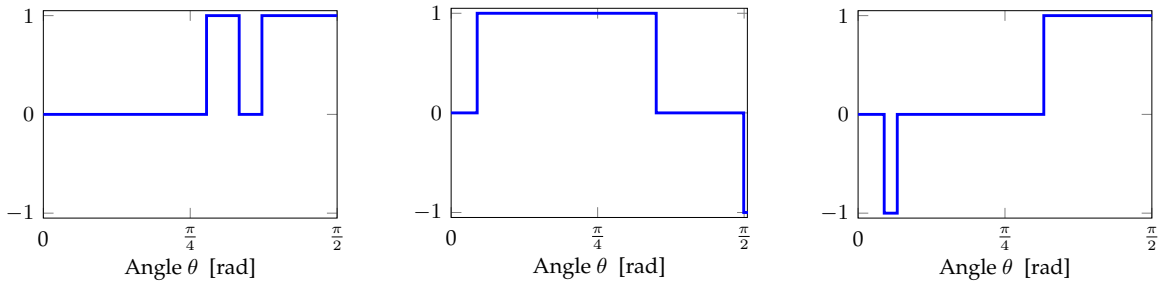

(a) $U_{Q1} = [1\ 0\ 1]^T$ (b) $U_{Q2} = [1\ 0\ -1]^T$ (c) $U_{Q2} = [-1\ 0\ 1]^T$

Figure 3.4: Optimal solutions for each of the three feasible switching sequences of the quarter- and half-wave symmetric OPP problem with multipolar switch positions for $d = 3$ and $m = 0.68$.

space, provide acceptable results. However, such algorithms cannot guarantee the optimality of the solution. Only the probability of finding the optimal solution might be increased through the careful choice of the initial values, which is discussed in the following section.

Second, allowing multipolar switch positions $u_i \in \{-1, 0, 1\}$ turns the three newly derived OPP problems (3.9), (3.10) and (3.11) into *mixed-integer* optimisation problems. This term refers to the mixed nature of the optimisation variables: While the switching angles are defined as a subset of real numbers, the switch positions are a subset of integer numbers. This further complicates the OPP problem and the solution process. One simple and common solution approach is to enumerate all admissible sequences of switch positions, the so-called *switching sequences*. A reduced, non-convex optimisation problem with only the switching angles as optimisation variables is solved for each switching sequence, and the resulting values for the objective function are compared. The switching sequence and the corresponding switching angles giving the lowest value are selected as global optimal solution. For the traditional three-level OPP problem, only a single switching sequence needs to be evaluated. However, for the relaxed OPP problems, there exist multiple feasible switching sequences. The generation of these feasible switching sequences is described in the following section. It is apparent that the computation of OPPs by enumeration is computationally tractable only for a low number of feasible switching sequences, and thus for the low pulse numbers considered in this thesis.

For completeness, it should be mentioned at this point that there exists another promising approach to solve the mixed-integer OPP problem by creating a new optimisation variable [27]. The combination of the value of the switching angle and the sign of the switching transition creates the so-called *virtual angle*. As a result, only *one* optimisation problem needs to be solved to take all feasible switching sequences into account. However, this approach makes use of the quarter- and half-wave symmetric properties of the pulse pattern, and is thus not directly applicable to the OPP problems with relaxed symmetry.

3.3.5 Example

For a better understanding of the OPP optimisation problem, consider for example the quarter- and half-wave symmetric OPP problem with multipolar switch positions (3.11) for pulse number $d = 3$. The optimisation variables are the three switching angles α_1, α_2 and α_3, and the three switch positions u_1, u_2 and u_3. The initial switch position u_0 is fixed to zero. The number of feasible switching sequences is four: $U_{Q1} = [1\ 0\ 1]^T$, $U_{Q2} = [1\ 0\ -1]^T$, $U_{Q3} = [-1\ 0\ 1]^T$, and $U_{Q4} = [-1\ 0\ -1]^T$. Since the fundamental component must have a zero phase shift, the switching sequence U_{Q4} leads to infeasibility. The three feasible switching sequences are shown in Fig. 3.4.

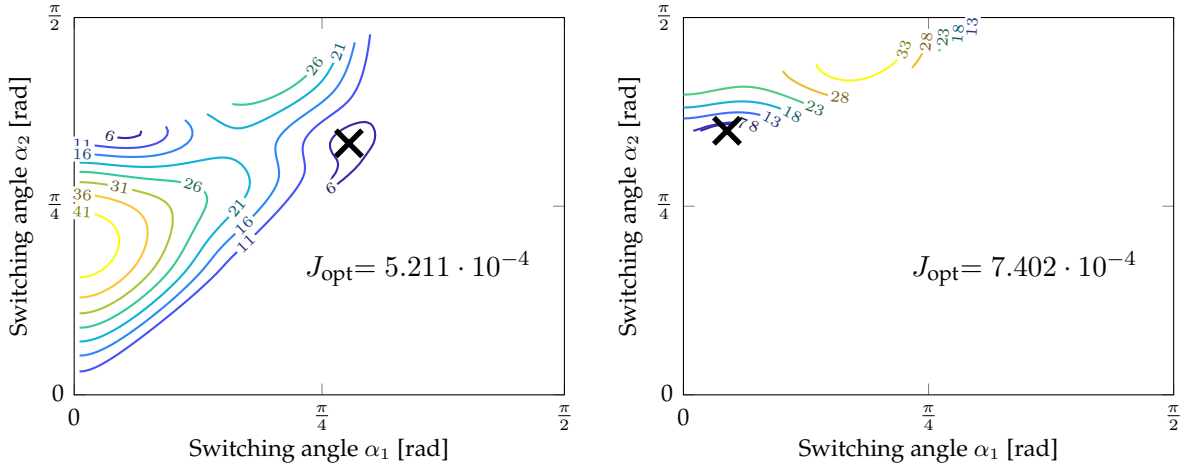

(a) $U_{Q1} = [1\ 0\ 1]^T$ (b) $U_{Q2} = [1\ 0\ -1]^T$

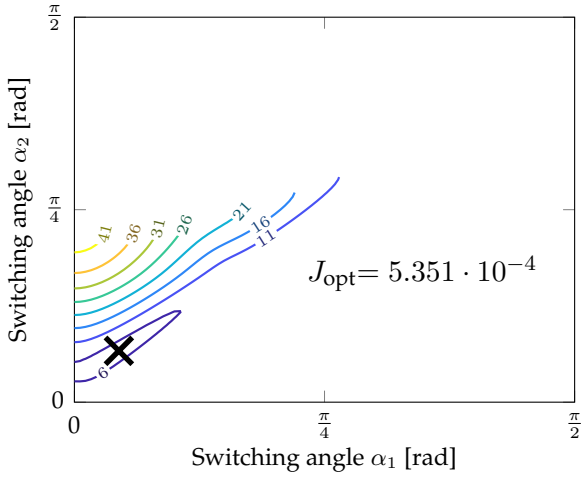

(c) $U_{Q2} = [-1\ 0\ 1]^T$

Figure 3.5: Values of the objective function $(\cdot 10^{-4})$ versus the first two angles for the three feasible switching sequences of the quarter- and half-wave symmetric OPP problem with multipolar switch positions for $d = 3$ and $m = 0.68$. The cross indicates the optimal solution.

Consider now the optimisation problem for one of the three switching sequences. The three switching angles provide three degrees of freedom; one is required to satisfy the equality constraint on the fundamental component. Thus, for the optimisation of the pulse pattern, the second and third switching angle remain for optimisation. It is thus possible to visualise the optimisation problem by evaluating the objective function for a grid of the two switching angles. The third switching angle for each point is determined by the modulation index constraint. If the solution satisfies the ascending order constraint on the switching angles, a feasible point is found. In the end, the objective function can be plotted over the two first switching angles for each feasible switching sequence. An example for the modulation index $m = 0.68$ is shown in Fig. 3.5. The figures show the search space for each of the three switching sequences. In each search space, the minimal value J_{opt} is indicated by the cross. For the first switching sequence, we see in Fig. 3.5a that a second local minima exists left of the global minimum. It is clear that a gradient-based solver requires multiple initial values to find both local minima. The optimal solution at this particular modulation index is the pulse pattern with the first switching sequence; it is shown in Fig. 3.4a.

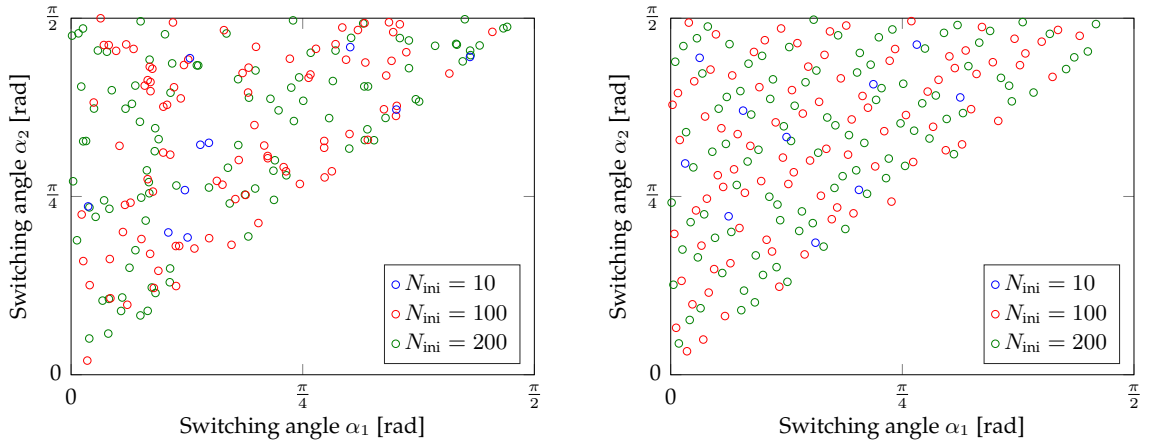

(a) Generated by `rand` function.

(b) Generated by Halton sequence.

Figure 3.6: Initial points for the quarter- and half-wave symmetric OPP optimisation problem with $d = 2$ generated by two different methods. The initial set fulfils the order constraint on the switching angles $0 \leq \alpha_1 \leq \alpha_2 \leq \frac{\pi}{2}$.

3.4 Computation of Optimised Pulse Patterns

3.4.1 Computational Features

In the previous section, we described the non-convex and mixed-integer properties of the OPP optimisation problem. In order to address the complications arising from these properties, the choice of the initial values and the enumeration of the switching sequences are discussed in detail in this section.

Choice of Initial Values A common method to choose the initial values is by generating random numbers and sorting them to meet the order constraint on the switching angles. An example set of initial values for the quarter- and half-wave symmetric OPP problem with $d = 2$ generated by MATLAB's `rand` function is shown in Fig. 3.6a for different numbers of initial values N_{ini}. We see from the figure that only with a large number of initial values, a sufficient distribution of the points over the search space is given. Thus, the optimisation problem has to be solved 200 or more times to ensure a high probability of finding the optimal solution.

Another method to generate the set of initial values is to use quasi-random Halton sequences [28]. These sets can be computed in advance for any number of switching angles and give a more even distribution over the search space, see Fig. 3.6b. We see from the figures that for a low number of initial values, the coverage of the entire search space by the Halton points is more uniform than for the randomly generated ones. The even distribution of the initial values positively influences the probability of finding the optimal solution. For more information on Halton sequences and their generation, the interested reader is referred to [29].

Enumeration of Switching Sequences Solving the mixed-integer OPP problem requires to enumerate all feasible switching sequences. The number of feasible switching sequences depends on the number of switch positions that are a degree of freedom. More specifically, due to the restriction of the switch positions to three integer values, only every second switch position is an actual degree of freedom. In the previous explained example, just the first and third switch position could be chosen to be either 1 or -1. We can generalise the degree of freedom originating from the switch positions to: ceil $\left(\frac{d}{2}\right)$. As there exist two options for each

Table 3.3: Number of feasible switching sequences for the four OPP problem types: quarter- and half-wave symmetry with unipolar switch positions (QaHWS$^+$), quarter- and half-wave symmetry with multipolar switch positions (QaHWS), half-wave symmetry (HWS) and the full-wave symmetry (FWS).

QaHWS$^+$	QaHWS	HWS	FWS
$N_{\text{seq,uQ}} = 1$	$N_{\text{seq,Q}} = 2^{\text{ceil}\left(\frac{d}{2}\right)} - 1$	$N_{\text{seq,H}} = 2^{d+1} - 2$	$N_{\text{seq,F}} = 2^{2d+1} - 4$

degree of freedom, the number of feasible switching sequences is $N_{\text{seq,Q}} = 2^{\text{ceil}\left(\frac{d}{2}\right)} - 1$. We subtracted the one switching sequence, which generates only negative switch positions in the positive half-wave of the fundamental period. Such a pulse pattern implies a phase shift of $180°$ of the fundamental component. Due to the zero phase shift constraint on the fundamental component, this switching sequence leads to an infeasible optimisation problem.

For the half-wave symmetric OPP problem with an initial switch position of zero, the degree of freedom for the switch positions doubles compared to the quarter- and half-wave symmetric OPP problem. Thus, the number of switching sequences with a zero initial switch position is 2^d. Additionally, we have to consider the switching sequences with a non-zero initial switch position. As the first *and* the second switch position are fixed in this case, the number of switching sequences with an initial switch position of -1 or 1 is 2^{d-1}. Thus, we determine the total number of feasible switching sequences to be $N_{\text{seq,H}} = 2^d + 2 \cdot 2^{d-1} - 2 = 2^{d+1} - 2$, where we again omitted the infeasible switching sequences with only negative switch positions in the positive half-wave of the fundamental waveform.

For full-wave symmetric OPPs, the number of switch positions that are optimisation variables is again doubled compared to half-wave symmetric OPPs. As a result, the number of switching sequences when assuming a zero initial switch position increases to 2^{2d}. For the two cases of a non-zero initial switch position, doubling the number of optimisation variables leads to 2^{2d-1} feasible switching sequences. The total number of feasible switching sequences for the full-wave symmetric OPP problem then follows as $N_{\text{seq,F}} = 2^{2d} + 2 \cdot 2^{2d-1} - 4 = 2^{2d+1} - 4$. The four omitted switching sequences are the ones with a dc-offset, meaning only positive or negative switch positions in the entire fundamental period.

The number of feasible switching sequences for each OPP type are listed in Table 3.3. Recall that for the traditional, quarter- and half-wave symmetric OPP with unipolar switch positions the number of feasible switching sequences is *one* (2.10).

Truncation of Infinite Sum Recall in the definition of the current TDD (2.3) the infinite sum of squared current harmonics. As the current TDD is adopted as objective function for the OPP problem, the infinite sum of harmonics emerges in each OPP optimisation problem. It is clear that the sum of an infinite number of terms is impossible to compute numerically. Therefore, to evaluate the current TDD and the objective function, we truncate the sum and consider only a finite number of harmonics N_{har}. Note that N_{har} does not correspond to the highest harmonic order that is considered. For the quarter- and half-wave, and half-wave symmetric OPP problems only harmonics of odd and non-triplen order are considered in the objective function. Thus, choosing $N_{\text{har}} = 100$ implies that the highest considered harmonic order is $n_{\text{max}} = 301$. In case of the full-wave symmetric OPP problem, when odd and even non-triplen harmonics are considered, choosing $N_{\text{har}} = 100$ implies that the highest order is $n_{\text{max}} = 151$.

In Fig. 3.7, the accuracy of the truncated sum is shown as a function of the number of considered harmonics in the objective function. The values of the objective function are normalised by the value obtained when considering 1000 harmonics. We can see from the figure that for the half-wave and quarter- and half-wave symmetric OPP problems, it is sufficient to consider 100 harmonics. For the full-wave symmetric OPP problem, twice as many harmonics are needed

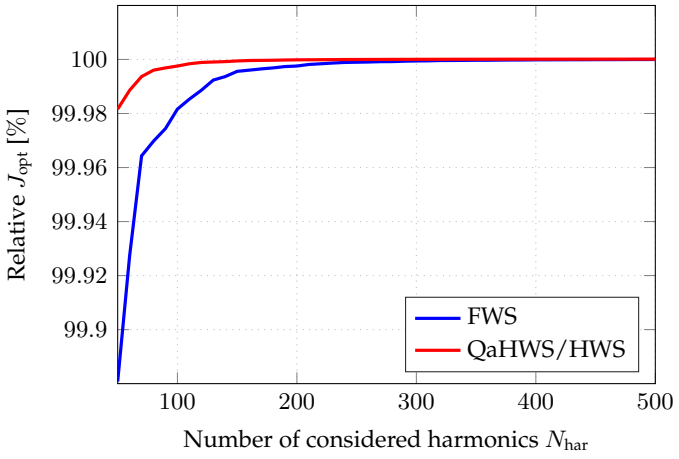

Figure 3.7: Accuracy of the objective function in dependence of the number of considered harmonics for the full-wave symmetric (FWS), half-wave symmetric (HWS) and quarter- and half-wave symmetric (QaHWS) OPP problem.

to achieve the same accuracy; this corresponds to considering harmonics up to the 300th order in the objective function.

3.4.2 Algorithm

The computational procedure described in [5] is adapted in this thesis for computing the OPPs with relaxed symmetry. In Fig. 3.8, the flow-chart of the computation is shown.

Step 1: The pulse number and modulation indices for the OPPs are specified. The modulation indices are determined by sampling the modulation range $m \in \left[0, \frac{4}{\pi}\right]$ with a certain step size, which gives the set $\mathcal{M}$ of modulation indices. Additionally, we need to specify which symmetry and switch position constraint we impose on the OPPs: Full-wave symmetry, half-wave symmetry, quarter- and half-wave symmetry with multipolar switch positions or quarter- and half-wave symmetry with unipolar switch positions.

Step 2: The pre-processing steps described in the previous section are executed next. The set of initial values is created from the Halton sequence for the required number of switching angles and adapted to the search space depending on the imposed symmetry conditions. The feasible switching sequences are generated and enumerated depending on the symmetry, the switch position constraint and the pulse number.

Step 3: With the modulation index m selected from the set $\mathcal{M}$, the specific optimisation problem for each particular feasible switching sequence is formulated.

Step 4: The optimisation problem is solved with the `fmincon` function of MATLAB. The solver uses the gradient method to search the search space for a local minimum, starting at the given initial values. Only the solution corresponding to the lowest value of the objective function is kept for each switching sequence.

Step 5: By comparing the obtained minimal values of the objective function for each switching sequence, the switching sequence yielding the lowest value is identified and kept as the optimal solution.

Step 6: From the optimal switching angles and switching sequence, the OPP over one entire fundamental period is constructed by applying the assumed symmetry conditions. The OPP is stored for the chosen modulation index. Then, the procedure is repeated from Step 3 for the next modulation index.

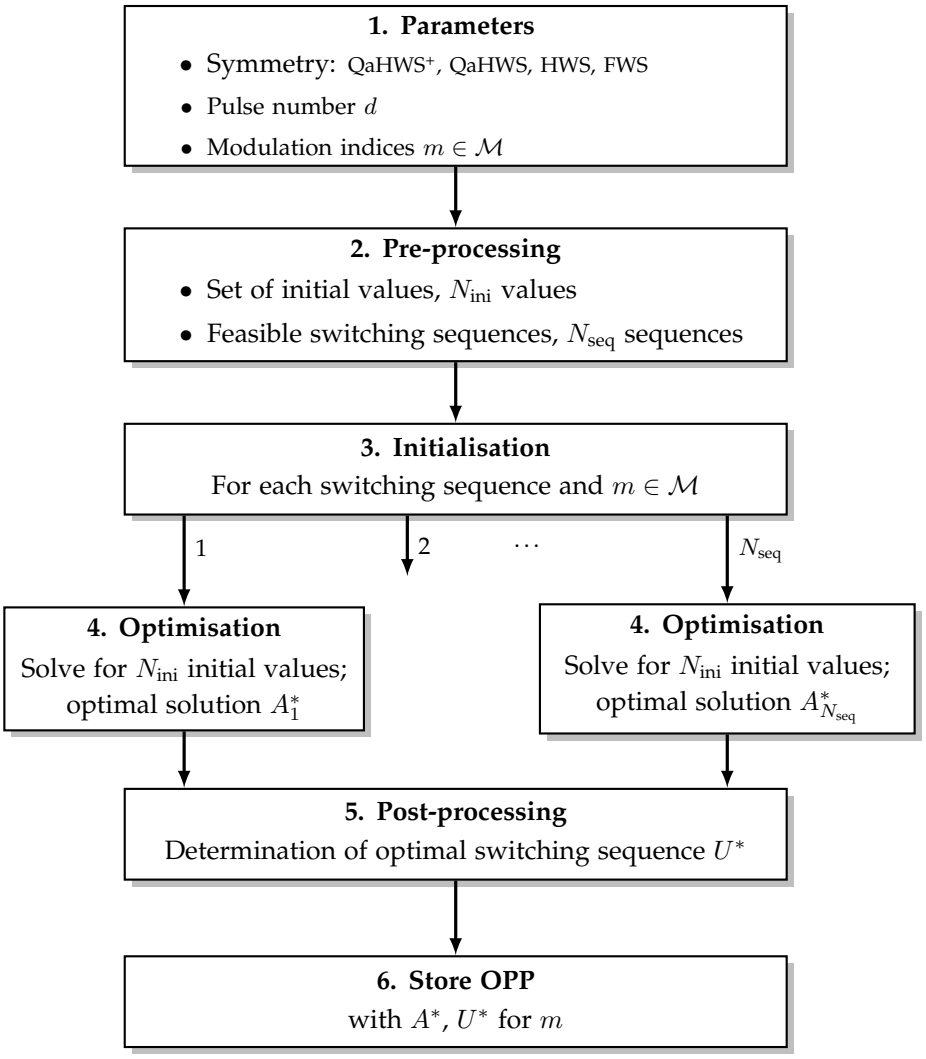

Figure 3.8: Computation procedure of OPPs with relaxed symmetry. Adapted from [5].

3.5 Performance Evaluation

For the case study presented in Section 3.1.2, OPPs of the four symmetry types and the pulse numbers $d \in \{1, 2, 3\}$ are computed over the entire modulation range. For the full-wave symmetric OPP problem, additionally the non-integer pulse numbers $d \in \{1.5, 2.5\}$ are considered. The modulation range is sampled with a step size of 0.01, which results in 127 modulation indices for each OPP problem. The minimum number of initial values generated by the Halton sequence is chosen as 100. Harmonics up to the 300th order are considered for the truncated sum in the objective function. The OPPs with relaxed symmetry are compared against the traditional unipolar quarter- and half-wave symmetric OPPs.

For the comparison of the various OPPs, we can calculate the current TDDs directly from the corresponding values of the objective function, (3.6) and (3.7), with

$$I_{\text{TDD}} = \frac{1}{\sqrt{2} I_{\text{nom}} \omega_1 X_\sigma} \frac{V_{\text{dc}}}{2} \sqrt{J_{\text{opt}}}, \tag{3.13}$$

where all quantities are in per unit and the nominal current is the rated current. Consequently, we can write $\sqrt{2} I_{\text{nom}} = 1$. Note that the modulation index is proportional to the angular fundamental frequency, as we assume a fully magnetised machine with a stator flux magnitude

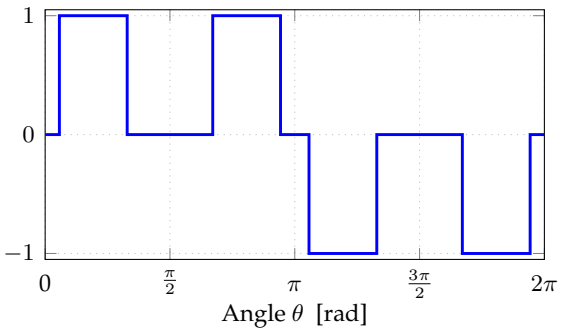

Figure 3.9: Quarter- and half-wave symmetric OPP for $d = 2$, resulting from the one feasible switching sequence for this pulse number with unipolar switch positions.

Ψ_s of 1 pu

$$\Psi_s = \frac{m}{\omega_1}\frac{V_{\text{dc}}}{2} = 1. \tag{3.14}$$

From this, the fundamental frequency follows as

$$\omega_1 = m\frac{V_{\text{dc}}}{2}, \tag{3.15}$$

which yields for the current TDD

$$I_{\text{TDD}} = \frac{1}{mX_\sigma}\sqrt{J_{\text{opt}}}\,. \tag{3.16}$$

3.5.1 Relaxing Unipolar Switch Positions

Relaxing the constraint of unipolar switch positions on the traditional OPP problem adds the negative output level $u_i = -1$, with $i \in \{1, \ldots, d\}$, as degree of freedom to the optimisation problem. This increases the number of feasible switching sequences to $N_{\text{seq,Q}} = 2^{\text{ceil}\left(\frac{d}{2}\right)} - 1$.

However, for pulse numbers $d = \{1, 2\}$, the only feasible switching sequence remains to be the traditional unipolar one, shown for example in Fig. 3.9 for pulse number $d = 2$. Consequently, solving the quarter- and half-wave symmetric OPP problem with multipolar switch positions results in the well-known traditional OPPs.

Multiple feasible multipolar switching sequences for the quarter- and half-wave symmetric OPP problem become possible for pulse numbers of $d = 3$ or higher. For pulse number $d = 3$, the three feasible switching sequences were shown in Fig. 3.4, and are repeated here for the reader's convenience: $U_{Q1} = [1\ 0\ 1]^T$, $U_{Q2} = [1\ 0\ -1]^T$ and $U_{Q3} = [-1\ 0\ 1]^T$. The first switching sequence corresponds to the traditional unipolar OPP, while the second and third one result in new multipolar pulse patterns. Two OPPs, obtained with the first and third switching sequence, are shown in Fig. 3.10a and Fig. 3.11a for a modulation index of $m = 0.6$. The corresponding harmonic spectra of the load currents are shown next to the OPPs. At this particular modulation index, the multipolar OPP reduces the current TDD from $12.22\,\%$ to $9.10\,\%$, i.e. by $25\,\%$. Inspection of the two spectra shows that this current TDD improvement results from the significantly reduced lower order harmonics in the multipolar OPP. We conclude that the additional degree of freedom introduced by the multipolar switch positions produces a *new* optimal solution for the quarter- and half-wave symmetric OPP problem.

To further evaluate the beneficial extent of the multipolar switch positions, the current TDDs for the entire modulation range resulting from the uni- and multipolar OPPs with $d = 3$ are calculated and plotted together in Fig. 3.12. For the current TDDs of multipolar OPPs, the respective optimal switching sequence is indicated for the particular modulation index range.

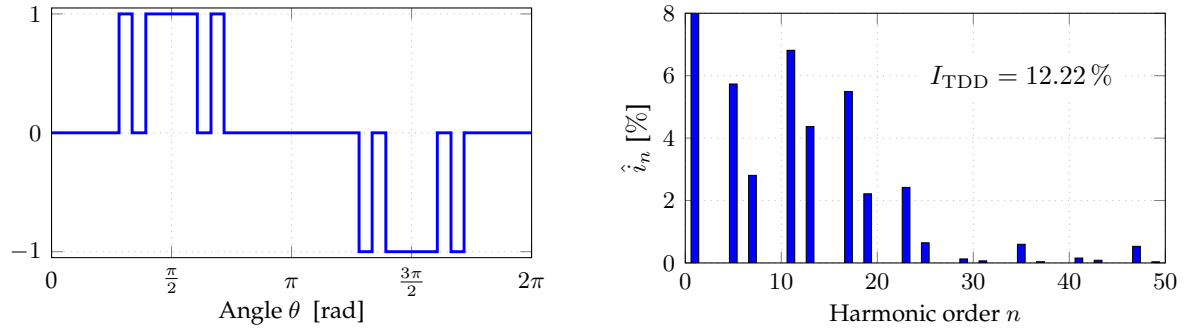

(a) Unipolar pulse pattern (b) Current spectrum

Figure 3.10: Pulse pattern and current spectrum of the quarter- and half-wave symmetric OPP with $d = 3$, $m = 0.6$ and unipolar switch positions $u_i \in \{0, 1\}, \forall i \in \{1, \ldots, d\}$.

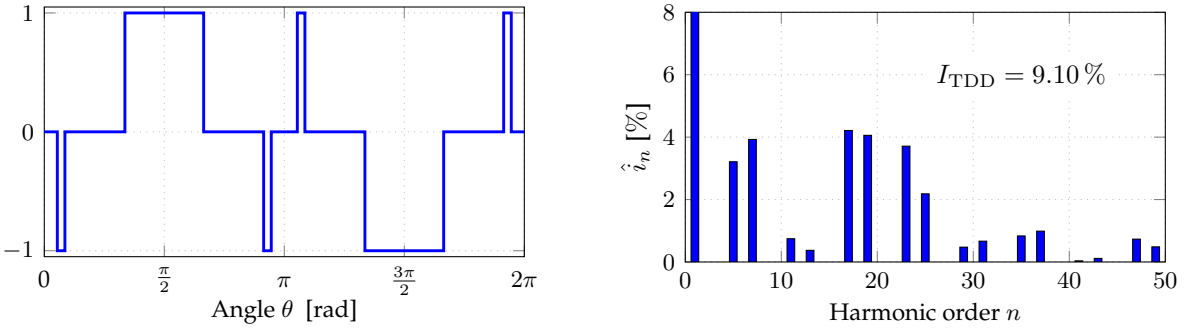

(a) Multipolar pulse pattern (b) Current spectrum

Figure 3.11: Pulse pattern and current spectrum of the quarter- and half-wave symmetric OPP with $d = 3$, $m = 0.6$ and multipolar switch positions $u_i \in \{-1, 0, 1\}, \forall i \in \{1, \ldots, d\}$.

We can see from the figure that for most of the modulation range, the first switching sequence U_{Q1}, i.e. the traditional unipolar one, yields the optimal solution. This implies that the OPPs computed based on the multipolar optimisation problem equal the OPPs computed with the traditional OPP formulation for these particular modulation indices. In the modulation index interval of $m = [0.37, 0.67]$, however, new solutions with lower current TDDs are found when utilising the multipolar switching sequences U_{Q2} and U_{Q3}. This interval is also highlighted in the figure. The maximum absolute and relative reductions of the current TDD in the specific interval of modulation indices are summarised in Table 3.4. By relaxing the unipolar switch position constraint, the current TDD can be reduced by up to $30\,\%$ relative to the current TDD obtained by the traditional OPPs.

Another important metric to consider for the OPP evaluation is the common-mode voltage. Due to (2.1), the switching signal, and thus the OPP, directly affects the common-mode voltage. For the further analysis, we calculate and examine the maximum common-mode switch

Table 3.4: Intervals of current TDD reduction when relaxing the unipolar switch position constraint for quarter- and half-wave symmetric OPPs with $d = 3$.

Interval	Optimal switching sequence	Modulation index interval	Maximum reduction of current TDD absolute	relative
I	U_{Q2}	$0.37 \leq m \leq 0.58$	$4.830\,\%$	$25.82\,\%$
	U_{Q3}	$0.58 < m \leq 0.67$	$3.304\,\%$	$30.68\,\%$

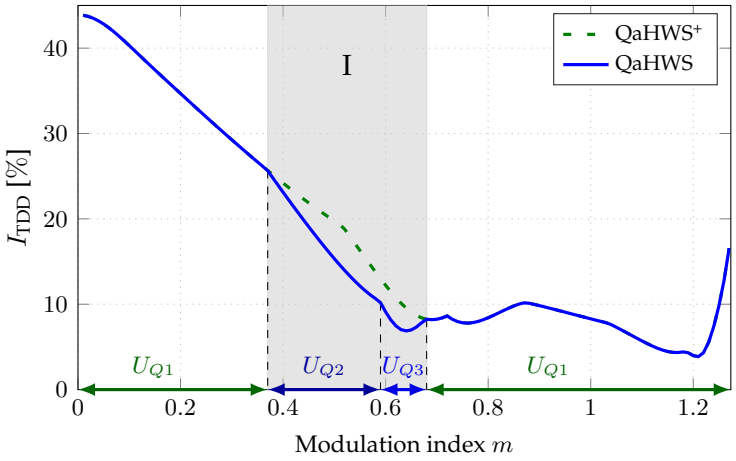

Figure 3.12: Current TDDs resulting from the uni- and multipolar OPPs with quarter- and half-wave symmetry imposed and $d = 3$.

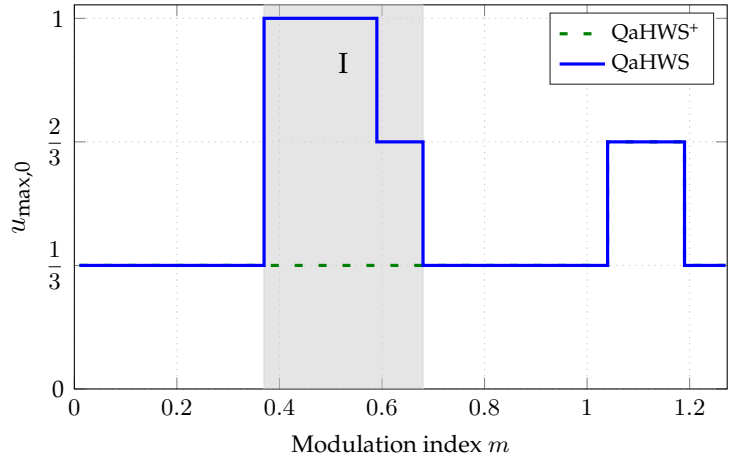

Figure 3.13: Maximum common-mode switch position of the uni- and multipolar OPPs with quarter- and half-wave symmetry imposed and $d = 3$.

position $u_{\mathrm{max},0}$ in one fundamental period generated by the three-phase pulse pattern

$$u_{\mathrm{max},0} = \max_{\theta\in[0,2\pi]} \frac{1}{3}\big(u_a(\theta) + u_b(\theta) + u_c(\theta)\big), \tag{3.17}$$

which is easily derived from (2.2).

The maximum common-mode switch positions of the uni- and multipolar OPPs with $d = 3$ are shown in Fig. 3.13 over the entire modulation range. The interval of current TDD reduction resulting from the multipolar switching sequences is again highlighted. The comparison shows that the multipolar OPPs increase the maximum common-mode voltage by up to three times. Note that when the optimal switching sequence changes from the second to the third one at $m = 0.59$, the maximum common-mode switch position decreases by $\frac{1}{3}$. To mitigate the adverse effect of the multipolar OPPs on the common-mode voltage, a constraint can be introduced in the optimisation problem limiting the maximum common-mode switch position to $\frac{2}{3}$. In return, the current TDD would increase slightly.

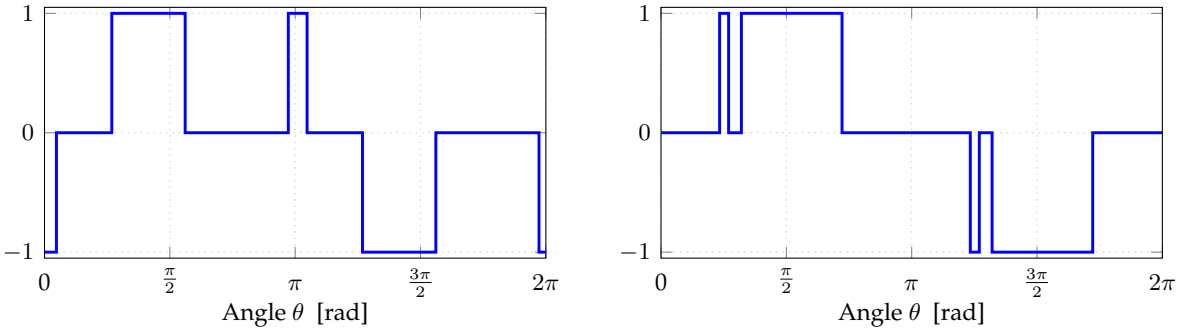

(a) OPP for $m = 0.54$ (b) OPP for $m = 0.8$

Figure 3.14: Half-wave symmetric OPPs with $d = 2$.

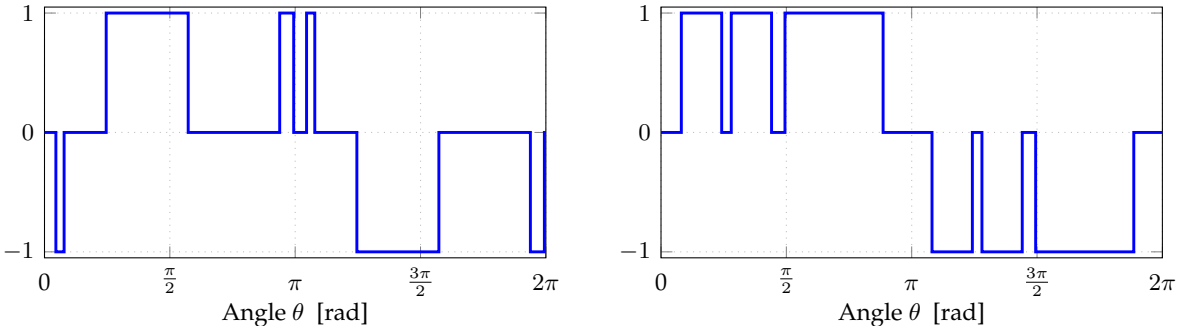

(a) OPP for $m = 0.6$ (b) OPP for $m = 1.05$

Figure 3.15: Half-wave symmetric OPPs with $d = 3$.

3.5.2 Relaxing Quarter-wave Symmetry

When relaxing the quarter-wave symmetry, the entire first fundamental half-wave of the pulse pattern is subject to optimisation. As a result, the domain of the switching angles expands to $\alpha_i \in [0, \pi]$, and the initial switch position is no longer constrained to zero, which gives rise to multiple new feasible switching sequences for all pulse numbers. According to the expression derived in Table 3.3, the number of switching sequences for the half-wave symmetric OPP problem with multipolar switch positions is $N_{\text{seq,H}} = 2^{d+1} - 2$. Thus, there are six feasible switching sequences for pulse number $d = 2$. These additional switching sequences and the expanded switching angle domain enable to compute new half-wave symmetric OPPs, such as the two examples shown in Fig. 3.14.

The OPP in the left figure, i.e. Fig. 3.14a, results from the multipolar switching sequence $U_{H2} = [-1\ 0\ 1\ 0]^T$. We can see from the figure that the non-zero initial switch position allows one to place a pulse over the edges of the fundamental period. The OPP shown in Fig. 3.14b is constructed from the traditional switching sequence $U_{H1} = [0\ 1\ 0\ 1]^T$. The optimisation of the four switching angles within the first half-wave of the fundamental allows one to push the third switching angle, which was constraint to the second quarter in the quarter- and half-wave symmetric OPP, over into the first quarter of the fundamental period. For this OPP, the commonly made statement that the number of switching angles in one quarter of the fundamental corresponds to the pulse number no longer holds true.

New OPPs are also found when considering the pulse number $d = 3$, see the examples in Fig. 3.15. The new feasible switching sequences and the enlarged switching signal domain allow one again to find new optimal solutions. For example, the half-wave symmetric OPP in

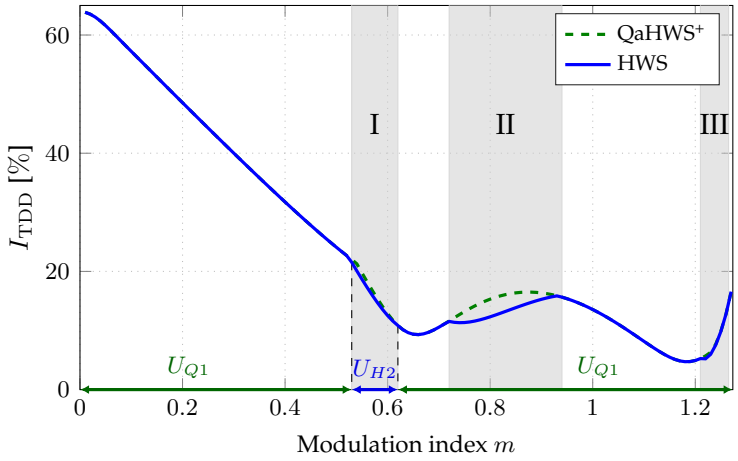

Figure 3.16: Current TDDs of the half-wave symmetric (HWS) and the traditional (QaHWS$^+$) OPPs with pulse number $d = 2$.

Fig. 3.15a at $m = 0.6$ arises from the multipolar switching sequence $U_{H4} = [0\ -1\ 0\ 1\ 0\ 1]^T$ with a single negative switch position in the first half-wave of the fundamental period. A comparison with the quarter- and half-wave symmetric OPP at the same modulation index, which is shown in Fig. 3.11a with the two negative switch positions in the first half-wave of the fundamental period, reveals that the half-wave symmetric OPP reduces the current TDD by $5.31\,\%$. The OPP at $m = 1.05$ built from the unipolar switching sequence $U_{H1} = [0\ 1\ 0\ 1\ 0\ 1]^T$ in Fig. 3.15b exploits the entire optimisation domain for each switching angle and clusters more than half of the switching angles in the first quarter of the fundamental. Thus, quarter-wave symmetry ceases to exist and the current TDD is reduced by $4.11\,\%$.

In Fig. 3.16, the current TDDs resulting from the OPPs with relaxed quarter-wave symmetry and the traditional OPPs are compared for pulse number $d = 2$ over the entire modulation range. The optimal switching sequences are indicated again for the specific modulation indices, and the intervals of current TDD reduction are highlighted. Note that the unipolar switching sequence U_{H1} is the half-wave symmetric equivalent to the switching sequence U_{Q1} of the quarter- and half-wave symmetric OPP problem. Thus, we refer to the unipolar half-wave symmetric switching sequence also with U_{Q1}. The absolute and relative values of the current TDD reduction in each interval are summarised in Table 3.5. We see from the figure and the table that the first interval of current TDD reduction is achieved by utilising the multipolar switching sequence U_{H2}. For the remainder of the modulation range, the traditional unipolar switching sequence is optimal. Thus, in the Intervals II and III the reduction of current TDD results from the OPPs as shown in Fig. 3.14b, which cluster more than half of the switching angles in one quarter of the fundamental period.

The four switching angles in the first half-wave of the fundamental in the half-wave symmetric OPP with pulse number $d = 2$ are shown in Fig. 3.17 over the entire modulation range.

Table 3.5: Intervals of current TDD reduction when relaxing quarter-wave symmetry of the OPP optimisation problem with $d = 2$.

Interval	Optimal switching sequence	Modulation index interval	Maximum reduction of current TDD	
			absolute	relative
I	U_{H2}	$0.53 \leq m \leq 0.61$	$1.20\,\%$	$5.64\,\%$
II	U_{Q1}	$0.72 \leq m \leq 0.93$	$2.99\,\%$	$19.52\,\%$
III	U_{Q1}	$1.22 \leq m \leq 1.26$	$0.490\,\%$	$8.60\,\%$

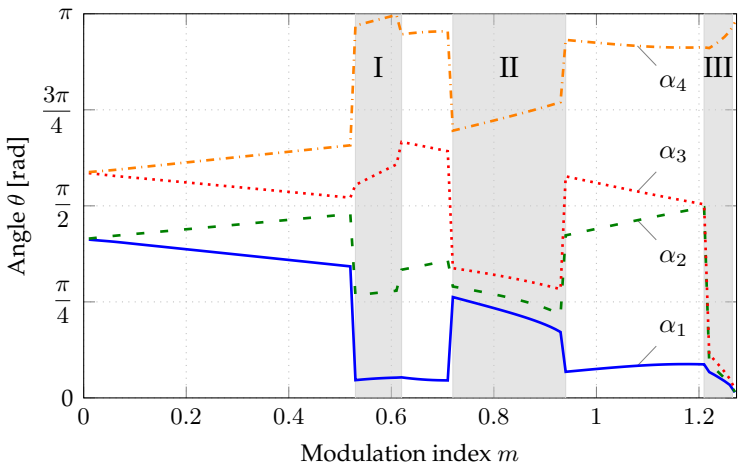

Figure 3.17: Switching angles of the half-wave symmetric OPP for pulse number $d = 2$ over the entire modulation range.

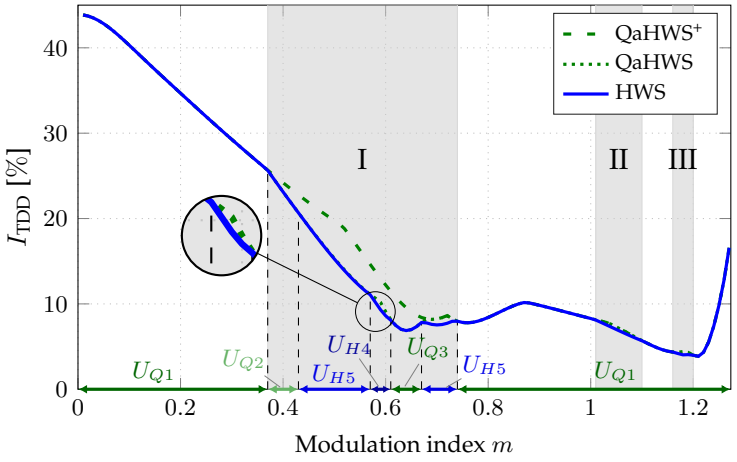

Figure 3.18: Current TDDs of OPPs with half-wave symmetry (HWS), quarter- and half-wave symmetry and multipolar switch positions (QaHWS) and of the traditional (QaHWS$^+$) OPPs for pulse number $d = 3$.

The modulation index intervals, in which the half-wave symmetric OPPs achieve lower harmonic distortions, are again highlighted. We can clearly distinguish these intervals from the remaining modulation indices, due to the removal of quarter-wave symmetry. Outside of these three intervals of current TDD reduction, the optimal solutions have quarter-wave symmetry.

For pulse number $d = 3$, the corresponding current TDDs of the half-wave symmetric and traditional OPPs are compared in Fig. 3.18 over the entire modulation range. The current TDDs of the previously computed quarter- and half-wave symmetric OPPs with multipolar switch positions are shown additionally. The optimal switching sequences for the half-wave symmetric OPP problem are indicated for each modulation index. Note that the terms U_{Q1}, U_{Q2} and U_{Q3} refer to the quarter- and half-wave symmetric switching sequences shown in Fig. 3.4 advanced over one fundamental half-wave. These switching sequences thus imply that the optimal solution exhibits quarter-wave symmetry. The switching sequence $U_{H5} = [1\ 0\ 1\ 0\ 1\ 0]^T$ starts with a non-zero initial switch position. The corresponding ranges of modulation indices for which the current TDD is reduced, and the maximum absolute and relative reductions of the current TDD within these intervals are listed in Table 3.6. The relative reductions are in relation to the current TDDs of the traditional OPPs at the respective modulation indices.

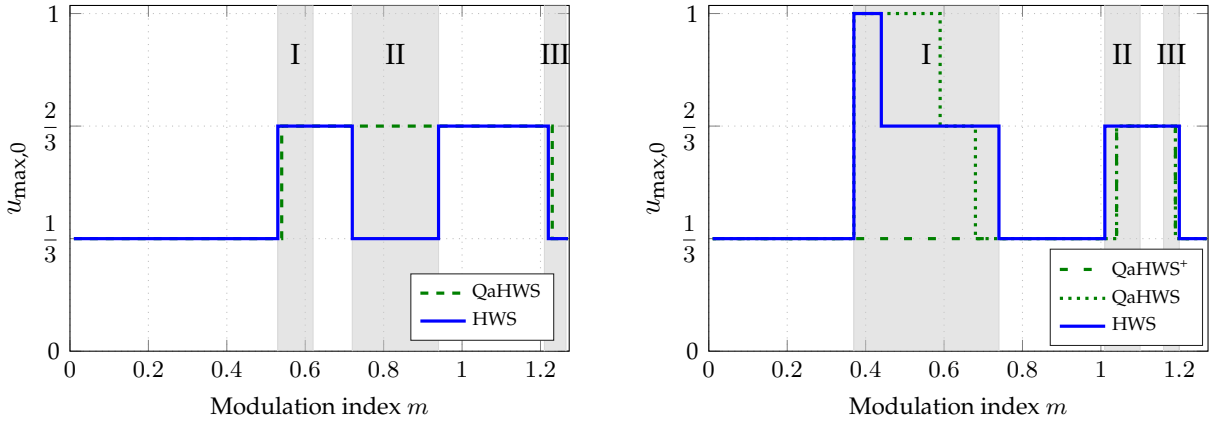

(a) Pulse number $d = 2$ (b) Pulse number $d = 3$

Figure 3.19: Maximum common-mode switch positions of half-wave symmetric (HWS) and quarter- and half-wave symmetric (QaHWS) OPPs.

Similar to the OPPs with pulse number $d = 2$, there are three intervals of modulation indices, for which new half-wave symmetric OPPs are obtained and therefore the current TDD is reduced. Further similarities to pulse number $d = 2$ are that the current TDD reduction in Interval I is achieved by employing multipolar switching sequences and for the remaining modulation range the traditional quarter-wave symmetric switching sequence is optimal. Note that an optimal quarter-wave symmetric switching sequence, i.e. U_{Q2} and U_{Q3}, implies that for these modulation indices the solutions correspond to the previously shown quarter- and half-wave symmetric OPPs. Thus, at these modulation indices, the relaxation of the quarter-wave symmetry has no effect on the optimal solution. However, for modulation indices in the interval of $m \in [0.43, 0.61]$ and $m \in [0.67, 0.74]$, new half-wave symmetric OPPs are found, which reduce the current TDD even further. Additionally, in the Intervals II and III, OPPs feature more than half of the switching angles in one quarter of the fundamental period, as the example in Fig. 3.15b, leading to small reductions in the current TDD.

The maximum common-mode switch position of the half-wave symmetric OPPs with pulse numbers $d = \{2, 3\}$ are calculated and compared in Fig. 3.19 over the entire modulation range with the corresponding quarter- and half-wave symmetric results. The modulation index intervals of current TDD reduction, due to the half-wave symmetric OPPs are also indicated in these figures. We can see that the half-wave symmetric OPPs with pulse number $d = 2$ incur no increase of the maximum common-mode voltage, but rather reduce the common-mode voltage

Table 3.6: Intervals of current TDD reduction when relaxing quarter-wave symmetry of the OPP optimisation problem with $d = 3$.

Interval	Optimal switching sequence	Modulation index interval	Maximum reduction of current TDD absolute	relative
I	U_{Q2}	$0.37 \leq m \leq 0.43$	2.113 %	9.27 %
	U_{H5}	$0.43 < m \leq 0.57$	4.909 %	26.26 %
	U_{H4}	$0.57 < m \leq 0.61$	3.677 %	29.53 %
	U_{Q3}	$0.61 < m \leq 0.67$	3.304 %	30.68 %
	U_{H5}	$0.67 < m \leq 0.74$	1.243 %	14.41 %
II	U_{Q1}	$1.01 \leq m \leq 1.10$	0.331 %	4.35 %
III	U_{Q1}	$1.17 \leq m \leq 1.19$	0.383 %	8.67 %

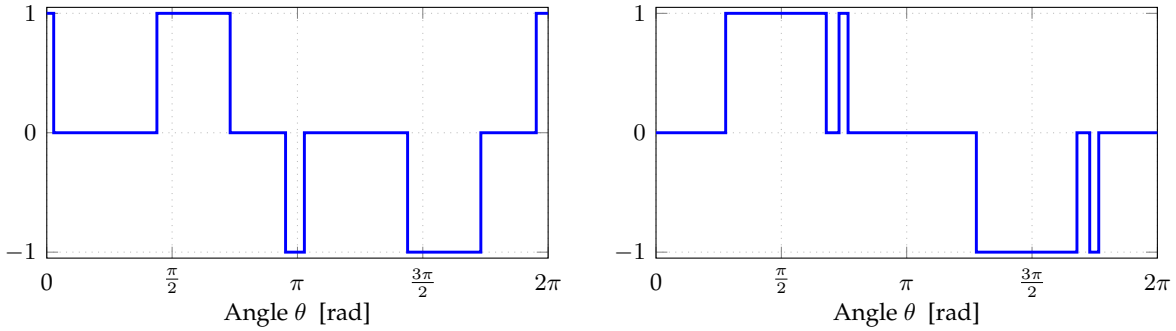

(a) Second OPP solution for $m = 0.54$

(b) Second OPP solution for $m = 0.8$

Figure 3.20: The second solutions for the half-wave symmetric OPP problem with $d = 2$ corresponding symmetrically to the OPPs in Fig. 3.14.

in Interval II. For pulse number $d = 3$, the relaxation of the quarter-wave symmetry benefits the maximum common-mode switch position likewise. We can see in Fig. 3.19b that the half-wave symmetric OPPs mitigate the adverse rise in the common-mode voltage caused by the relaxation of the switch position constraint in the quarter- and half-wave symmetric OPPs.

Symmetry An interesting feature arises for the half-wave symmetric OPP problem: For each modulation index in the intervals of current TDD reduction, a second half-wave symmetric solution exists. The second solution gives the same value for the objective function, and thus for the current TDD, but has a different set of switching angles and/or switching sequence. Alternative OPPs for pulse number $d = 2$ are shown in Fig. 3.20. The corresponding first solutions are given in Fig. 3.14. Close examination of the two pairs reveals that for each pair of the two solutions are in fact symmetrical to each other. We determine this symmetry as

$$u_B(\theta) = -u_A(2\pi - \theta), \tag{3.18}$$

where $u_A(\theta)$ and $u_B(\theta)$ refer to the OPPs of the first and second solution, respectively. Recall that the OPPs are half-wave symmetric. Thus, we can insert (2.6) in (3.18) and obtain

$$-u_B(\pi + \theta) = -u_A(2\pi - \theta). \tag{3.19}$$

When we substitute $\theta' = \pi + \theta$ and use the property of 2π periodicity of the OPPs we obtain

$$u_B(\theta') = u_A(\pi - \theta'). \tag{3.20}$$

As a result, (3.20) implies that the first half-waves of the two OPPs of a solution pair are line symmetric about $\frac{\pi}{2}$.

The existence of the two solutions and the symmetry to each other is visualised in Fig. 3.21. The figure shows the search space of the half-wave symmetric OPP problem with $d = 2$ at $m = 0.8$ in dependence of the first and fourth switching angle when assuming the unipolar switching sequence. Recall that the half-wave symmetric OPP problem requires two degrees of freedom to set the fundamental component to the reference, see (3.9). Thus, two switching angles remain as degree of freedom, which span the search space shown in the figure, in which the global minimum is to be found. The dashdotted line across the search space corresponds to the line symmetry about $\frac{\pi}{2}$, i.e. $\alpha_1 = \pi - \alpha_4$. The two minima with identical minimal current TDD are indicated with the crosses. These two minima correspond to the OPPs in Fig. 3.14b and Fig. 3.20b. We can see from the figure that the entire search space is symmetrical with relation to the dashdotted line.

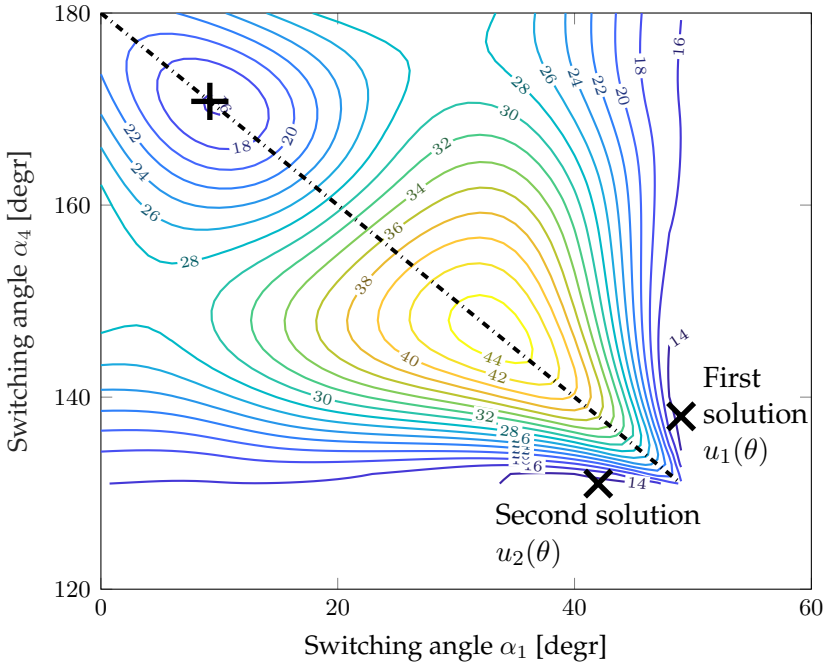

Figure 3.21: Current TDD (values in [%]) plotted over the first and fourth switching angle of the half-wave symmetric OPP optimisation problem for $d = 2$ and at $m = 0.8$. Note that the angles are indicated in degrees.

To prove the symmetry of the two OPP solutions we calculate the two pairs of Fourier coefficients a_{An} and b_{An}, and a_{Bn} and b_{Bn} for the first and second solution, respectively. The detailed derivation is given in Appendix B. As a result, we obtain the correlations

$$a_{An} = -a_{Bn} \qquad \text{and} \qquad b_{An} = b_{Bn}. \tag{3.21}$$

Because the Fourier coefficients in the objective function are squared, it is apparent from (3.21) that the two solutions give an identical value for their respective local minima and thus result in the same current TDD.

Another interesting characteristic of the OPP problem can be observed from Figure 3.21: The expansion of the search space dimension due to the relaxation of quarter-wave symmetry. Note that the search space of the half-wave symmetric OPP problem with $d = 2$ is two-dimensional when applying the unipolar switching sequence and when fixing the amplitude and phase of the fundamental component. Imposing quarter-wave symmetry, one dimension is removed as the problem has two switching angles less for optimisation and one equality constraint is dropped. Thus, the search space reduces to just a line, which corresponds to the dashdotted line in the figure. As a result, the quarter- and half-wave symmetric OPP problem can find only the local minimum (shown as a $+$) at the top left corner of the search space, which is therefore identified as the global minimum. When relaxing the quarter-wave symmetry condition, we can see that this minimum however is only suboptimal.

To summarise, the quarter-wave symmetry relaxation adds degrees of freedom to the OPP problem by, first, extending the domain of the switching angles and, second, enabling multiple feasible switching sequences. In the expanded search space, new local minima emerge leading to new half-wave symmetric solutions. These solutions are beneficial for the current TDD *and* the maximum common-mode voltage for certain modulation indices. Two symmetrical solutions exist for every half-wave symmetric OPP giving the exact same current TDD.

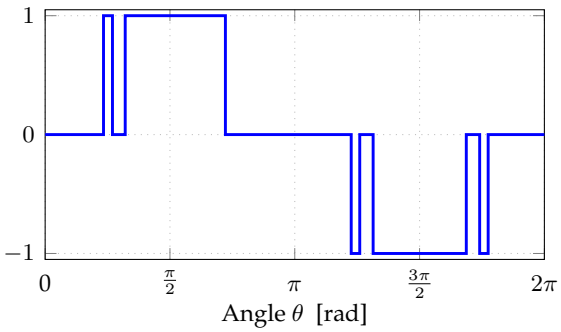

Figure 3.22: Full-wave symmetric OPP with pulse number $d = 2.5$ and $m = 0.8$.

3.5.3 Relaxing Half-wave Symmetry

Last, we compute and examine OPPs with relaxed half-wave symmetry. With only 2π periodicity imposed, the pulse pattern over the entire fundamental period is subject to optimisation. Thus the domain for the switching angles is further expanded, and the number of feasible switching sequences is increased. For the pulse numbers $d = \{1, 2, 3\}$, the resulting pulse patterns nevertheless exhibit half-wave symmetry even without explicitly imposing it. For these low pulse numbers, we can draw the conclusion that imposing half-wave symmetry has no adverse effect on the optimality of OPPs. It, however, reduces the computational burden by cutting the number of optimisation variables to half and reducing the number of feasible switching sequences by roughly 2^{d+1}, see Table 3.3.

Full-wave symmetry gives rise to non-integer pulse numbers, e.g. $d = \{1.5, 2.5, \ldots\}$. An example of a full-wave symmetric OPP with pulse number $d = 2.5$ at $m = 0.8$ is shown in Fig. 3.22. By closely inspecting the pulse pattern, we observe similarities with the OPP with pulse number $d = 2$ in Fig. 3.14b and with the OPP with $d = 3$ in Fig. 3.10a. It appears that the non-integer full-wave symmetric OPP is a combination of the half-wave symmetric OPP with $d = 2$ from 0 to π and the half-wave symmetric OPP with $d = 3$ from π to 2π. Similar to the feature of two symmetric solutions, which we observed for the half-wave symmetry OPP problem, another full-wave symmetric OPP exists. In this second solution for the OPP, the first half-wave corresponds to the OPP with $d = 3$ and the second half-wave corresponds to the OPP with $d = 2$.

This characteristic is observed for other modulation indices and non-integer pulse numbers. In fact, each half-wave of the full-wave symmetric OPP with the non-integer pulse number d appears to correspond to one half-wave of the half-wave symmetric OPPs with the pulse numbers $\lfloor d \rfloor$ and $\lceil d \rceil$. Note that $\lfloor d \rfloor$ and $\lceil d \rceil$ refer to the *floor* and *ceiling* operation, respectively, rounding d to the smaller and larger integer.

The current TDDs of the full-wave symmetric OPPs with $d = \{1.5, 2.5\}$ are shown in Fig. 3.23 together with those of the half-wave symmetric OPPs with integer pulse numbers $d = \{1, 2, 3\}$ over the entire modulation range. We can see that for each modulation index the current TDDs of OPPs with non-integer pulse numbers are significantly different from the current TDDs of OPPs with integer pulse numbers. More specifically, the OPPs with non-integer pulse numbers yield current TDDs, that are bounded from above and below by those of OPPs with floor- and ceil-rounded integer pulse numbers. This is in line with the earlier observation that OPPs with non-integer pulse numbers d are the combination of OPPs with pulse numbers $\lfloor d \rfloor$ and $\lceil d \rceil$.

Consider for comparison the current TDDs of the traditional OPPs with the integer pulse numbers $d = \{1, 2, 3\}$ in Fig. 3.24. The figure shows that at certain modulation indices, the current TDDs of two consecutive pulse numbers are equal. At $m = 0.8$, for example, OPPs

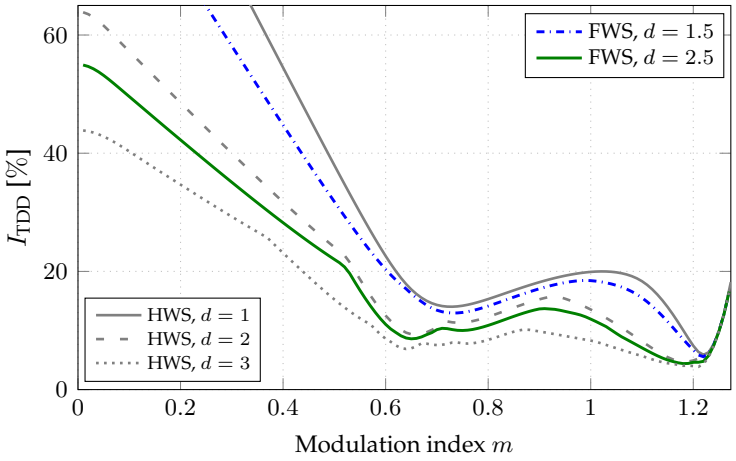

Figure 3.23: Current TDD of full-wave symmetric (FWS) OPPs with non-integer pulse numbers and half-wave symmetric (HWS) OPPs with integer pulse numbers.

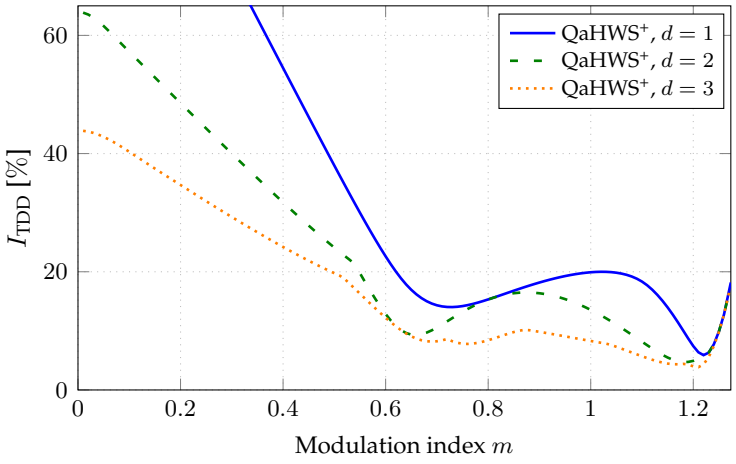

Figure 3.24: Current TDDs of the traditional quarter- and half-wave symmetric OPPs with unipolar switch positions for different pulse numbers (QaHWS$^+$).

with pulse numbers $d = 1$ and $d = 2$ yield current TDDs of $15.3\,\%$, and at $m = 0.63$, the same current TDD of $10.1\,\%$ is achieved by OPPs with pulse numbers $d = 2$ and $d = 3$. This is in contrast to the common assumption that higher pulse numbers always decrease the current TDD. However, recall that a reduction of the current TDD at specifically these two modulation indices was observed when relaxing quarter-wave symmetry and allowing multipolar switch positions, see Table 3.5 and Table 3.6. This corresponds to the observation from Fig. 3.23 that the half-wave symmetric OPPs with multipolar switch positions gain a considerable reduction in the current TDD at each modulation index when increasing the pulse number. We suggest that equal current TDDs for different pulse numbers is an artefact resulting by imposing quarter-wave symmetry and unipolar switch positions.

3.6 Summary

OPPs with relaxed symmetry and multipolar switch positions are introduced, computed and evaluated in this chapter. The derived OPP optimisation problems are non-convex, mixed-integer problems. By relaxing the typically made assumptions on the OPP problem, new OPPs were found. As the traditional OPP problem claims to give unique optimal solutions, the com-

putation of a new OPPs with lower current TDDs reveals that the traditional OPPs are suboptimal.

The restrictive nature of the intuitively assumed unipolar switch positions is revealed as current TDD reductions of up to $30\,\%$ are achieved by the OPPs with multipolar switch positions. The advantageous effect of the multipolar switch position leads to only a slight increase of the computational burden for low pulse numbers. When high pulse numbers are considered, the formulation method of virtual angles can be used to avoid evaluating a large number of feasible switching sequences, which causes almost no increase of the computation time [27]. The main disadvantage, the tendency to increase the common-mode voltage, can be mitigated by an additional constraint in the optimisation problem.

Likewise, the assumption of quarter-wave symmetry artificially restricts the OPP optimisation problem. Half-wave symmetric OPPs are computed for various modulation indices, which reduce the current TDD by up to $20\,\%$ and $30\,\%$ for pulse numbers $d = 2$ and $d = 3$, respectively. These reductions were experimentally verified in [30]. The relaxation of quarter-wave symmetry additionally has an advantageous effect on the common-mode voltage. The presence of two solutions for each half-wave symmetric OPP offers an additional degree of freedom to choose the OPP best suited for the particular application. The main disadvantage of the half-wave symmetric OPPs is that a large number of feasible switching sequence needs to be evaluated. The reformulation of the problem based on the virtual angles [27] might again be possible and facilitate the computation.

Computation of the full-wave symmetric OPPs indicates that half-wave symmetry might not adversely restrict the OPP optimisation problem. No difference in current TDDs was observed for pulse numbers up to $d = 3$. In addition, entirely new OPPs with non-integer pulse numbers can be computed, which offer current TDDs in between the half-wave symmetric integer pulse number solutions.

In conclusion, the intuitive assumptions on the pulse patterns have, to a certain extent, a significant impact on the optimality of the OPPs. Therefore, such simplifying assumptions should be handled with care. Moreover, the additional degrees of freedom provided by relaxing these assumptions, enable the computation of new OPPs, and allow additional terms to be included in the objective function.

Chapter 4

Model Predictive Pulse Pattern Control of Higher-order Systems

4.1 Introduction

Model predictive control (MPC) was developed in the 1970s for applications in the process industry [31]. Over the past two decades, MPC has emerged in the field of power electronics, and gained popularity as an alternative and universal control method [32]. Main advantages are its ability to handle non-linear systems and systems with multiple inputs and outputs, its versatility the cost function offers and its inherent robustness. Based on an internal dynamic model, the controller predicts the evolution of the system over a finite-time horizon, i.e. the *prediction horizon*. An optimisation problem is formulated with a cost function capturing the control objectives, such as optimal reference tracking. Constraints can also be included. By solving the constrained finite-time optimisation problem, the optimal control action over the prediction horizon is obtained. The receding horizon policy is adopted to provide feedback. It implies that only the control action until the next sampling instant is applied to the converter. At the next sampling instant, the process of formulating and solving the optimisation problem is repeated over a shifted prediction horizon.

Due to these advantages, MPC provides a suitable framework to establish control based on optimised pulse patterns (OPPs) with fast transients. Typically, the control of OPPs is restricted to systems with slowly changing operating points. When the modulation index or the pulse number changes, discontinuities usually arise in the switching angles, see for example in Fig. 3.17. This leads to a slow transient response and can even cause overcurrents [7]. The development of an MPC strategy based on OPPs enables the combination of the optimal steady-state performance achieved by OPPs with the fast transient response of MPC. Such a control technique is called model predictive pulse pattern control (MP^{3}C) [33]. From the OPP, a reference trajectory is computed, which contains the fundamental and optimal harmonic components. MP^{3}C then modifies the switching instants of the OPP in order to achieve close trajectory tracking. State-of-the-art MP^{3}C scheme is restricted to first-order systems, i.e. systems with inductive loads.

In this chapter, a generalised MP^{3}C method is derived, which exploits the optimal harmonic performance of OPPs and enables fast control of *higher-order* systems. The proposed MP^{3}C algorithm is divided in two parts: Computation of the optimal reference trajectories from the OPP for each controlled variable, and formulation of an MPC problem based on OPPs for optimal tracking of the precomputed trajectories. We refer to this control method as MP^{3}C$^+$.

In the following, a brief introduction of MPC for power electronics is given along with the description of the existing control techniques based on OPPs. The case study used for

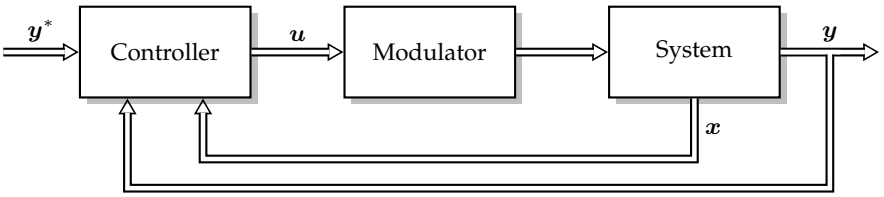

Figure 4.1: In MPC, the controller regulates the system outputs $\boldsymbol{y}$ along their corresponding references $\boldsymbol{y}^*$. The manipulated variable $\boldsymbol{u}$ is the solution to a constrained optimisation problem based on an internal system model. We assume that the system states $\boldsymbol{x}$ are readily available from the system without requiring an observer.

the controller design in this chapter is presented in the remainder of the introduction. The control approach and the objectives of the proposed MP^{3}C$^+$ scheme are described in Section 4.2, and Section 4.3 shows the derivation and implementation of the required reference trajectories. In Section 4.4, the proposed MP^{3}C$^+$ algorithm is presented and the underlying optimisation problem is derived. In Section 4.5, the limitations of the proposed control strategy and the applied compensation methods are theoretically discussed. Section 4.6 shows the simulation results and discusses the performance in dependence of the control parameters.

4.1.1 Model Predictive Control

The five key features characterising MPC are described hereafter. For a detailed introduction to MPC problems, the interested reader is referred to [31].

Internal System Model An internal system model is used to predict the future evolution of the system. Consider the control loop shown in Fig. 4.1. The system has the output vector $\boldsymbol{y} \in \mathbb{R}^{n_y}$ and the state vector $\boldsymbol{x} \in \mathbb{R}^{n_x}$. The input vector $\boldsymbol{u} \in \mathbb{R}^{n_u}$ is the manipulated variable and influences the system states such that the reference vector $\boldsymbol{y}^* \in \mathbb{R}^{n_y}$ is optimally tracked. A discrete-time model is used, which describes the dynamic behaviour of the system at the sampling times kT_s, where $k \in \mathbb{N}$ and T_s is the sampling interval. Assuming $\boldsymbol{u}(t)$ is constant for the time interval $t \in [kT_s, (k+1)T_s]$ and corresponds to $\boldsymbol{u}(k)$, we derive the discrete-time model

$$\boldsymbol{x}(k+1) = \boldsymbol{A}\boldsymbol{x}(k) + \boldsymbol{B}\boldsymbol{u}(k) \tag{4.1a}$$
$$\boldsymbol{y}(k+1) = \boldsymbol{C}\boldsymbol{x}(k), \tag{4.1b}$$

where $\boldsymbol{A} \in \mathbb{R}^{n_x \times n_x}$, $\boldsymbol{B} \in \mathbb{R}^{n_x \times n_u}$ and $\boldsymbol{C} \in \mathbb{R}^{n_y \times n_x}$ are the state, input and output matrix, respectively. The discrete-time model might be derived from a continuous-time model of the system by exact discretisation.

Constraints On the input, state and output variables, constraints of the following form can be imposed

$$\boldsymbol{u} \in \boldsymbol{\mathcal{U}} \subseteq \mathbb{R}^{n_u} \tag{4.2a}$$
$$\boldsymbol{x} \in \boldsymbol{\mathcal{X}} \subseteq \mathbb{R}^{n_x} \tag{4.2b}$$
$$\boldsymbol{y} \in \boldsymbol{\mathcal{Y}} \subseteq \mathbb{R}^{n_y}. \tag{4.2c}$$

Constraints on the state and output variables are usually imposed as *soft* constraints. They specify a certain operation range arising from practical restrictions and may usually be slightly violated during optimisation in order to maintain feasibility. The input constraints are caused by physical limitations and cannot be violated. They are *hard* constraints.

Depending on the input constraints, we distinguish between two families of MPC methods for power electronics: The first one applies the manipulated variable $\boldsymbol{u}$ to a modulator, which creates the appropriate switching signals for the converter. This is shown in Fig. 4.1 and is referred to as *indirect* MPC. The manipulated variable is constrained to a continuous set, e.g.

$$\boldsymbol{\mathcal{U}} = [-1, 1]^{n_u} . \tag{4.3}$$

In *direct* MPC, the vector of manipulated variables $\boldsymbol{u}$ is directly applied to the converter. This removes the modulator stage in Fig. 4.1. The system inputs are constrained to the levels of the converter, for example in the case of a three-level converter

$$\boldsymbol{\mathcal{U}} = \{-1, 0, 1\}^{n_u}. \tag{4.4}$$

Cost Function A cost function is derived capturing the control objectives. Within this thesis, we consider the accurate *reference tracking* of all output variables as the main objective. The resulting cost function is of the form

$$J\big(\boldsymbol{x}(k), \boldsymbol{U}(k)\big) = \sum_{\ell=k}^{k+N-1} I(\boldsymbol{x}(\ell), \boldsymbol{u}(\ell)), \tag{4.5}$$

where $N \in \mathbb{N}$ is the finite-time prediction horizon and $\boldsymbol{U}(k)$ is the sequence of manipulated variables $\boldsymbol{U}(k) = \big[\boldsymbol{u}^T(k)\ \boldsymbol{u}^T(k+1) \dots \boldsymbol{u}^T(k+N-1)\big]^T$. The stage cost $I(\boldsymbol{x}(\ell), \boldsymbol{u}(\ell))$ penalises the predicted system state $\boldsymbol{x}(\ell)$ when applying input $\boldsymbol{u}(\ell)$ at the sampling step ℓT_s within the prediction horizon. The future system states within the cost function are predicted with the help of the internal dynamic model and uses the current state measurement $\boldsymbol{x}(k)$ as the initial state. For our purposes, we assume that all system states can be measured directly in the system and no additional observer is required.

Optimisation Stage In the optimisation stage, a constrained finite-time optimisation problem is formulated and solved. By minimising the cost function subject to constraints and system dynamics described by the internal model, the optimal sequence of manipulated variables $\boldsymbol{U}(k)$ is obtained. The optimisation problem is stated as follows

$$\boldsymbol{U}(k) = \arg \underset{\boldsymbol{U}(k)}{\text{minimise}}\ J\big(\boldsymbol{x}(k), \boldsymbol{U}(k)\big) \tag{4.6a}$$

$$\text{subject to } \boldsymbol{x}(\ell+1) = \boldsymbol{A}\boldsymbol{x}(\ell) + \boldsymbol{B}\boldsymbol{u}(\ell) \tag{4.6b}$$

$$\boldsymbol{y}(\ell+1) = \boldsymbol{C}\boldsymbol{x}(\ell), \tag{4.6c}$$

$$\boldsymbol{u}(\ell) \in \boldsymbol{\mathcal{U}} \qquad \forall \ell = k, \dots, k+N-1. \tag{4.6d}$$

When the optimisation problem is solved online, the computation needs to be performed in real time. This implies that the solution needs to be available at the next sampling instant. Depending on the MPC strategy, this may pose a challenge. For example, constraining the input vector to integer numbers in direct MPC turns the optimisation problem into a mixed-integer problem, which can be challenging to solve.

Receding Horizon Control The obtained optimal sequence of manipulated $\boldsymbol{U}(k)$ achieves the optimal open-loop behaviour of the system from kT_s until the end of the prediction horizon. Out of this sequence, only the manipulated variable $\boldsymbol{u}(k)$ for the current sampling interval is applied to the converter. The remaining elements in $\boldsymbol{U}(k)$ are discarded. At the next sampling instant, the updated system state is measured $\boldsymbol{x}(k+1)$ and fed back to the controller as the initial

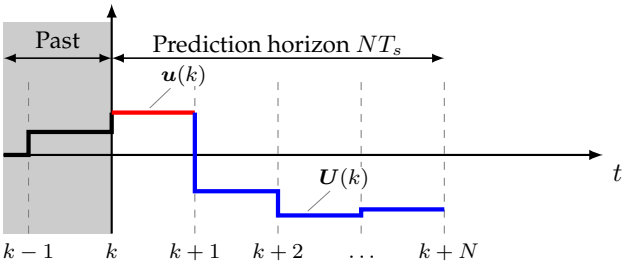

(a) Prediction horizon at $t = kT_s$

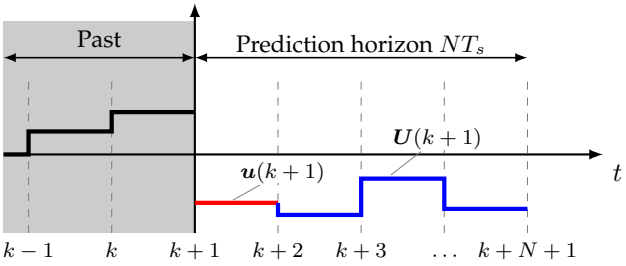

(b) Prediction horizon at $t = (k+1)T_s$

Figure 4.2: Receding horizon policy: From the computed optimal sequence of manipulated variables $\boldsymbol{U}(k)$ over the prediction horizon only the the first element $\boldsymbol{u}(k)$ is applied. At the next sampling step, the optimisation is repeated and the new optimal sequence $\boldsymbol{U}(k+1)$ is obtained.

state for the internal dynamic model, which closes the loop. Based on this new initial state, the evolution of the system is predicted over a shifted horizon and a new optimisation problem is solved. This policy is referred to as *receding horizon control*. The principle is illustrated in Fig. 4.2.

4.1.2 Literature Review

Finite-control-set Model Predictive Control

A specific direct MPC method is *finite-control-set* MPC (FCS-MPC) [34]. Adopting the notion of trajectory tracking, the optimal sequence of manipulated variables, i.e. the switching sequence, is found by enumerating all feasible combinations. For the simple case of current reference tracking in a two-level converter system with an RL load, the FCS-MPC algorithm with a prediction horizon of $N = 1$ was presented in [35]. This concept of predictive current control was extended to three-level converters in [36]. Additionally, the objectives of balanced dc-link capacitor voltages and reduced switching frequency were considered in the cost function. In the following years, this conceptually simple and versatile control method led to an increased research interest [34], although the prediction horizon was generally restricted to $N = 1$.

It is apparent that longer prediction horizons exponentially increase the number of possible switching sequences. Finding the solution of the MPC problem by enumeration in real time thus becomes impractical. For prediction horizons longer than one, the sphere decoding algorithm was proposed [37], [38]. With this technique, the reference tracking MPC problem can be solved time efficiently even for long prediction horizons. The benefit of longer prediction horizons is especially noticeable when considering higher-order systems such as drive systems with LC filters. In [39], the TDD of the stator current in such a case study operated at a low switching frequency was reduced by up to 70 % when increasing the prediction horizon from one to 20 steps.

The switching signal produced by FCS-MPC is not periodic. This results from the fact that

only the switching signal until the end of the prediction horizon is available for optimisation and that the prediction horizon is in general very short compared to the fundamental period. Due to the absence of periodicity, the resulting harmonic spectra are spread out over a large frequency range. For the application of FCS-MPC to a grid-connected converter system, large filters would be required to meet harmonics grid codes.

Trajectory Tracking Control with OPPs

In 1991, the first theoretical considerations of a trajectory tracking current controller based on offline computed OPPs for induction machine drives were published [40]. In order to minimise the tracking error estimated at the current sampling instant, the switching instants of the pulse pattern within the sampling interval are varied in time. This control idea was further developed in [41]. First experimental results were also presented. The main disadvantage of this current tracking controller is the dependence of the system model on the leakage inductance. A new control approach emerged a decade later by introducing tracking of the stator flux trajectory [42]. The optimal flux trajectory is obtained from the OPP by integrating the switching signal over time. The system model is independent of machine parameters. However, establishing closed-loop torque and speed control requires the fundamental components of the stator current and flux. Thus, an additional observer needs to be implemented in the control loop [43].

In [33], flux trajectory tracking control based on OPPs was formulated as an MPC problem. The controller solves an optimisation problem, which minimises the pulse pattern modification over a prediction horizon while controlling the stator flux along its reference. This is achieved by penalising the flux tracking error at the end of the prediction horizon. In contrast to the previous methods, the fundamental and harmonic components of the stator flux are treated as one entity, which makes the additional observer for the fundamental component obsolete. This MPC method is called model predictive pulse pattern control (MP^{3}C). Experimental results for a five-level inverter drive system operating with MP^{3}C are given in [44]. For the control of an inverter drive system with an LC filter, MP^{3}C is augmented with an active damping loop [45]. A filter extracts the harmonic content close to the resonance frequency, which is then damped with a linear quadratic regulator by adding the necessary damping flux to the reference.

Control of multiple variables by an OPP-based MPC scheme has not been proposed yet.

4.1.3 Grid-connected MV Converter with LC Filter Case Study

For the controller design in this chapter, the grid-connected converter system depicted in Fig. 4.3 is chosen as an example of a higher-order system. The rated parameters of the system are provided in Table 4.1. The three-level NPC converter, introduced in Section 3.1.2, is connected via an LC filter and transformer to the point of common coupling (PCC). All quantities are referred to the secondary side of the transformer. The filter components are the inductor L_1 and the capacitor C_2 with their series resistances R_1 and R_2, respectively. The transformer can be represented by its leakage inductance L_t and series resistance R_t. The grid is modelled by the grid inductance L_g, its series resistance R_g and the grid voltage $\boldsymbol{v}_{g,abc}(t)$. We assume to know the exact grid parameters for the simulations. The rated parameters in Table 4.1 are used to establish the per unit system. The parameters of the converter, filter and grid are given in Table 4.2 in SI units and per unit. With this, the resonance frequency of the system is calculated as

$$f_{\text{res}} = \frac{1}{2\pi}\sqrt{\frac{L_1 + L_t + L_g}{C_2 L_1 (L_t + L_g)}} = 484.8\,\text{Hz}. \tag{4.7}$$

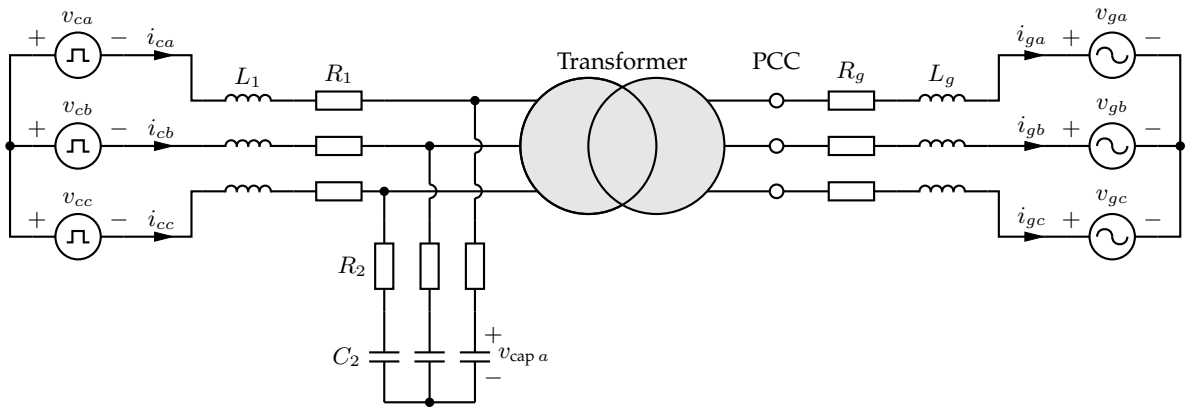

Figure 4.3: Grid-connected MV converter system with LC filter and transformer.

Table 4.1: Rated values of the grid-connected MV converter system.

Parameter	Symbol	SI value
Rated line-to-line voltage (secondary side)	V_R	3.3 kV
Rated current (secondary side)	I_R	1.575 kA
Rated apparent power (secondary side)	S_R	9 MVA
Rated angular grid frequency	ω_g	$2\pi 50\,\mathrm{rad\,s^{-1}}$

Table 4.2: Parameters of the grid-connected MV converter system.

Parameter	Symbol	SI value	pu value
Dc-link voltage	V_{dc}	4.84 kV	1.7963 pu
Filter inductance	L_1	0.35 mH	0.0909 pu
Filter inductance resistor	R_1	0.30 mΩ	0.000 25 pu
Filter capacitor	C_2	420 µF	0.1597 pu
Filter capacitor resistor	R_2	4.00 mΩ	0.0033 pu
Transformer leakage inductance	L_t	0.578 mH	0.1500 pu
Transformer resistor	R_t	18.10 mΩ	0.0150 pu
Grid inductance	L_g	0.383 mH	0.0995 pu
Grid resistor	R_g	12.00 mΩ	0.010 pu

The controlled variables are the three-phase converter current $\boldsymbol{i}_{c,abc}(t)$, the capacitor voltage $\boldsymbol{v}_{\text{cap},abc}(t)$ and the grid current $\boldsymbol{i}_{g,abc}(t)$. The grid voltages $\boldsymbol{v}_{g,abc}(t)$ are assumed to be ideal sinusoidal voltage sources.

Clarke Transformation The three-phase quantities of the converter system are transformed to the stationary orthogonal reference frame by the Clarke transformation. We ignore the common-mode component and use the reduced Clarke transformation. It translates the three-phase quantity $\boldsymbol{\xi}_{abc} = [\xi_a \ \xi_b \ \xi_c]^T$ to the 2-dimensional vector $\boldsymbol{\xi}_{\alpha\beta} = [\xi_\alpha \ \xi_\beta]^T$ and vice versa by:

$$\boldsymbol{\xi}_{\alpha\beta} = \boldsymbol{K}\,\boldsymbol{\xi}_{abc} \qquad \text{and} \qquad \boldsymbol{\xi}_{abc} = \boldsymbol{K}^{-1}\,\boldsymbol{\xi}_{\alpha\beta}, \tag{4.8}$$

where $\boldsymbol{K}$ and $\boldsymbol{K}^{-1}$ are the transformation matrices given by:

$$\boldsymbol{K} = \frac{2}{3}\begin{bmatrix} 1 & -\frac{1}{2} & -\frac{1}{2} \\ 0 & \frac{\sqrt{3}}{2} & -\frac{\sqrt{3}}{2} \end{bmatrix} \qquad \boldsymbol{K}^{-1} = \begin{bmatrix} 1 & 0 \\ -\frac{1}{2} & \frac{\sqrt{3}}{2} \\ -\frac{1}{2} & -\frac{\sqrt{3}}{2} \end{bmatrix}. \tag{4.9}$$

The scaling factor $\frac{2}{3}$ is needed to ensure invariance of the amplitudes.

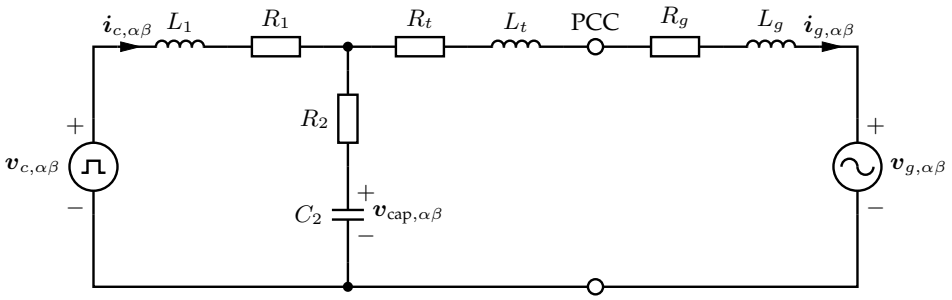

Figure 4.4: Grid-connected MV converter system with LC filter in $\alpha\beta$ coordinates.

System Model

With the transformed three-phase quantities the grid-connected converter system can be modelled in the stationary orthogonal reference frame as shown in Fig. 4.4. From this, the following dynamical equations of the system are derived

$$L_1 \frac{\mathrm{d}\boldsymbol{i}_{c,\alpha\beta}(t)}{\mathrm{d}t} = -R_1\, \boldsymbol{i}_{c,\alpha\beta}(t) - R_2 \left(\boldsymbol{i}_{c,\alpha\beta}(t) - \boldsymbol{i}_{g,\alpha\beta}(t)\right) - \boldsymbol{v}_{\text{cap},\alpha\beta}(t) + \boldsymbol{v}_{c,\alpha\beta}(t) \tag{4.10a}$$

$$C_2 \frac{\mathrm{d}\boldsymbol{v}_{\text{cap},\alpha\beta}(t)}{\mathrm{d}t} = \boldsymbol{i}_{c,\alpha\beta}(t) - \boldsymbol{i}_{g,\alpha\beta}(t) \tag{4.10b}$$

$$L_3 \frac{\mathrm{d}\boldsymbol{i}_{g,\alpha\beta}(t)}{\mathrm{d}t} = -R_3\, \boldsymbol{i}_{g,\alpha\beta}(t) + R_2 \left(\boldsymbol{i}_{c,\alpha\beta}(t) - \boldsymbol{i}_{g,\alpha\beta}(t)\right) + \boldsymbol{v}_{\text{cap},\alpha\beta}(t) - \boldsymbol{v}_{g,\alpha\beta}(t), \tag{4.10c}$$

where the transformer and grid parameters are combined to

$$L_3 = L_t + L_g \qquad \text{and} \qquad R_3 = R_t + R_g. \tag{4.11}$$

The converter voltage is the scaled switching signal

$$\boldsymbol{v}_{c,\alpha\beta}(t) = \frac{V_{\text{dc}}}{2} \boldsymbol{K}\, \boldsymbol{u}_{abc}(t), \tag{4.12}$$

where V_{dc} is the dc-link voltage and $\boldsymbol{u}_{abc}(t)$ is the three-phase switching signal $\boldsymbol{u}_{abc}(t) = [u_a(t)\ u_b(t)\ u_c(t)]^T$. Recall that for the three-level converter, the three-phase switch positions are restricted to $\boldsymbol{u}_{abc} \in \boldsymbol{\mathcal{U}}$, with $\boldsymbol{\mathcal{U}} = \{-1, 0, 1\}^3$.

The state vector is chosen as

$$\boldsymbol{x}_{\alpha\beta}(t) = \left[\boldsymbol{i}_{c,\alpha\beta}^T(t)\ \boldsymbol{v}_{\text{cap},\alpha\beta}^T(t)\ \boldsymbol{i}_{g,\alpha\beta}^T(t)\ \boldsymbol{v}_{g,\alpha\beta}^T(t)\right]^T, \tag{4.13}$$

in which the grid voltage is included as state variable. The size of the state vector is thus $n_x = 8$. The output vector

$$\boldsymbol{y}_{\alpha\beta}(t) = \left[\boldsymbol{i}_{c,\alpha\beta}^T(t)\ \boldsymbol{v}_{\text{cap},\alpha\beta}^T(t)\ \boldsymbol{i}_{g,\alpha\beta}^T(t)\right]^T \tag{4.14}$$

contains the six controlled variables, i.e. $n_y = 6$. With this, the multiple-input multiple-output (MIMO) state-space model is derived in continuous-time

$$\frac{\mathrm{d}\boldsymbol{x}_{\alpha\beta}(t)}{\mathrm{d}t} = \boldsymbol{F}\, \boldsymbol{x}_{\alpha\beta}(t) + \boldsymbol{G}\, \boldsymbol{u}_{abc}(t) \tag{4.15a}$$

$$\boldsymbol{y}_{\alpha\beta}(t) = \boldsymbol{C}\, \boldsymbol{x}_{\alpha\beta}(t), \tag{4.15b}$$

where the matrices $\boldsymbol{F} \in \mathbb{R}^{n_x \times n_x}$, $\boldsymbol{G} \in \mathbb{R}^{n_x \times n_u}$ and $\boldsymbol{C} \in \mathbb{R}^{n_y \times n_x}$ are provided in Appendix C.

4.2 Control Problem

The main control objective for the grid-connected converter system is to regulate the power flow from the converter over the LC filter and transformer to the grid. To achieve a power factor of one, the reactive power reference is set to zero. Note that in practice the real and reactive power are controlled at the PCC. For simplification, we have combined the grid and transformer reactance and resistance in the system model (4.10), which removes the PCC. As a result, we assume to control the power directly at the grid voltage source.

4.2.1 Control Objectives

MP^{3}C$^+$ aims to achieve the following objectives:

1. Minimal harmonic distortions of the grid current at steady-state.
2. Fast response to transients and disturbances.
3. Attenuation of the oscillations caused by the filter resonance.
4. Robustness against observer noise and parameter uncertainties.

The reference trajectories are obtained from the OPPs, which implies optimal harmonic performance during steady-state. By taking into account the impedance of the LC filter in the objective function of the OPP optimisation problem, the harmonics around the resonance frequency can be minimised. The resulting OPPs thus provide active damping of the filter resonances when the steady-state reference trajectories are steadily tracked. During transients, the new set point for the real and reactive power is translated into the required nominal OPP and therefore to the new reference trajectory. By closely tracking this new trajectory, a fast transient response is achieved. The required robustness is inherently achieved with MPC by employing the receding horizon policy, which provides feedback to the controller.

4.2.2 Control Approach

The block diagram of the controller is shown in Fig. 4.5. The controller operates at the equidistant time instants $t = kT_s$ with $k \in \mathbb{N}$ and the sampling interval T_s. An outer control loop translates the real and reactive power set points, P^* and Q^*, to a *converter voltage* reference. This is typically done with the help of a phasor analysis using the system dynamics derived in (4.10). For this, we require the absolute value of the measured grid voltage, $|\boldsymbol{v}_{g,\alpha\beta}|$. The resulting converter voltage reference is defined by the required load angle γ^* and the converter voltage amplitude. The load angle defines the phase angle difference between converter and grid voltage. The obtained voltage amplitude can be mapped into the necessary modulation index m using the measured dc-link voltage V_{dc}.

The modulation index m and the load angle γ^* are then used by the inner control loop to compute the optimal switching signal for the converter. The inner control loop performs two main operations: Reference generation and pulse pattern control.

The *reference generation* creates the steady-state nominal trajectory of each output variable over the prediction horizon, $\boldsymbol{Y}^*_{\alpha\beta}(k)$, and is based on the principle of superposition. Each voltage source in the system, namely the converter voltage and grid voltage, contribute independently to the waveforms. From the OPPs, the trajectory contribution of the converter voltage $\boldsymbol{Y}^*_{1\mathrm{conv},\alpha\beta}(\theta)$ can be computed offline over one fundamental period at the reference sampling angles $\boldsymbol{\theta}^*_{\mathbf{1}}$. During online operation this trajectory is loaded from a look-up table for the provided modulation index m and pulse number d. The current angular position ϕ^*_c on the trajectory

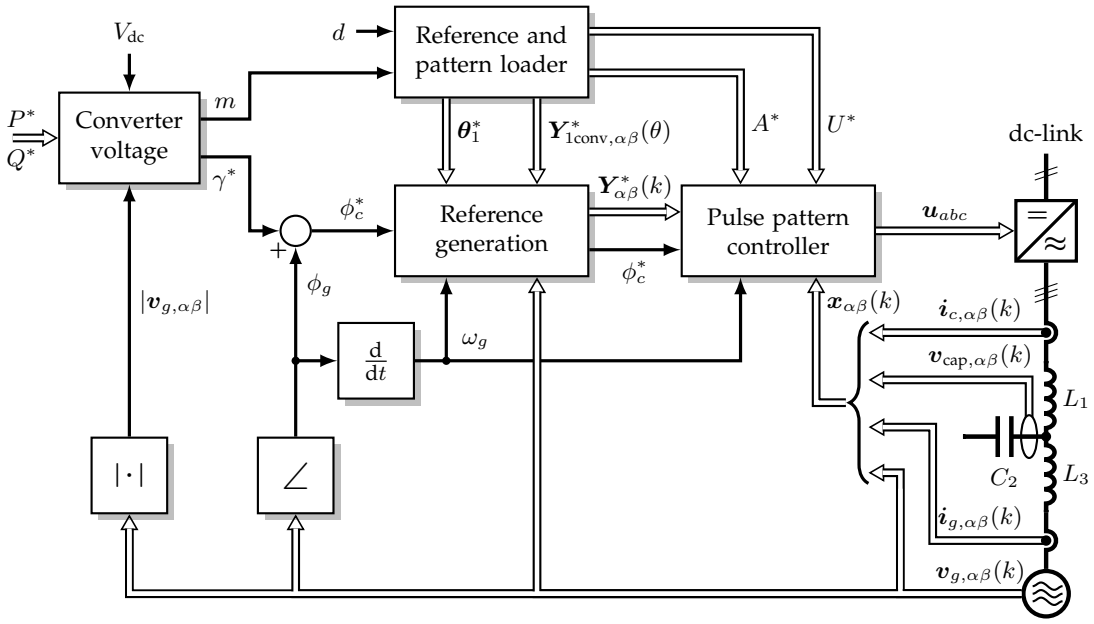

Figure 4.5: Controller for the grid-connected converter system. The outer control loop creates the converter voltage set point from the power references. The inner control loop is composed of the reference and pattern loader, the trajectory generation and the pulse pattern controller.

is obtained from the load angle and the measured grid phase angle ϕ_g. To translate sampling angles of the trajectory into sampling instants of the controller, the measured angular grid frequency ω_g is used. Additionally, the trajectory contribution of the grid voltage is computed and superimposed. A detailed description of the offline and online trajectory computation is given in Section 4.3.

The *pulse pattern controller* receives the OPP with the nominal switching angles A^* and the switching sequence U^*. The OPP is loaded along with the reference trajectories from a look-up table. With the help of the angle ϕ_c^* and the angular frequency ω_g, the current position in the fundamental period of the loaded OPP is identified and the switching angles are translated to switching times. Based on the measured state vector $\boldsymbol{x}_{\alpha\beta}(k)$ at the current sampling instant and the reference trajectory $\boldsymbol{Y}^*_{\alpha\beta}(k)$, the controller then formulates and solves the trajectory tracking MP^{3}C$^+$ problem. The modified switching signal $\boldsymbol{u}_{abc}$ is the optimal solution. Section 4.4 explains the MP^{3}C$^+$ scheme in detail.

The switching signal for the current sampling interval, i.e. until the next sampling instant, is applied to the converter. In practise, the switching instants within the sampling interval along with the new switch positions are provided. This concept is based on time stamps. Alternatively, a single switch position might be computed, e.g. by approximating the switching signal to an integer switch position.

4.3 Reference Computation

The reference trajectories are the nominal waveforms under steady-state conditions for each output variable, i.e.

$$\boldsymbol{y}^*_{\alpha\beta}(t) = \left[\boldsymbol{i}^{*T}_{c,\alpha\beta}(t)\ \boldsymbol{v}^{*T}_{\mathrm{cap},\alpha\beta}(t)\ \boldsymbol{i}^{*T}_{g,\alpha\beta}(t)\right]^T. \tag{4.16}$$

In the assumed case study, the two voltage sources, i.e. the converter voltage $\boldsymbol{v}_{c,\alpha\beta}(t)$ and the grid voltage $\boldsymbol{v}_{g,\alpha\beta}(t)$, contribute to this trajectory. By applying the principle of superposition,

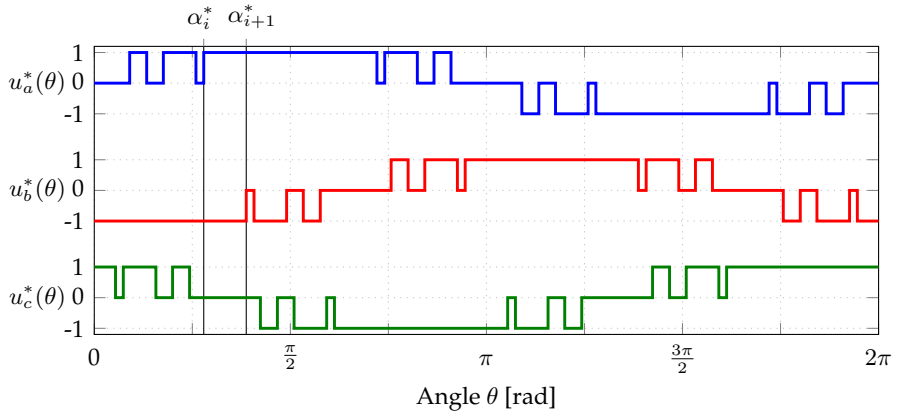

Figure 4.6: Three-phase OPP over one fundamental period. Between α_i^* and α_{i+1}^* the three-phase switch position is constant and the evolution of the output variables can be computed with (4.21).

the contribution of each voltage source can be computed separately and then added together

$$\boldsymbol{y}^*_{\alpha\beta}(t) = \boldsymbol{y}^*_{\text{conv},\alpha\beta}(t) + \boldsymbol{y}^*_{\text{grid},\alpha\beta}(t), \tag{4.17}$$

where $\boldsymbol{y}^*_{\text{conv},\alpha\beta}(t)$ and $\boldsymbol{y}^*_{\text{grid},\alpha\beta}(t)$ contain the reference contributions of the nominal converter and grid voltage, respectively. Recall that at steady-state, the nominal converter voltage is the scaled nominal switching signal $\boldsymbol{u}^*_{abc}(t)$, which corresponds to the OPP. Thus, the reference contribution of the converter voltage can be obtained directly from the OPP in an offline computation. The grid voltage $\boldsymbol{v}_{g,\alpha\beta}(t)$ is assumed to be an ideal sinusoid, which facilitates an online computation of the corresponding reference contribution.

Considering the two voltage sources separately implies using the reduced state vector

$$\tilde{\boldsymbol{x}}_{\alpha\beta}(t) = \boldsymbol{y}^*_{\alpha\beta}(t) \tag{4.18}$$

to derive the state-space model for the reference trajectory computation

$$\frac{\mathrm{d}\tilde{\boldsymbol{x}}_{\alpha\beta}(t)}{\mathrm{d}t} = \tilde{\boldsymbol{F}}\,\tilde{\boldsymbol{x}}_{\alpha\beta}(t) + \boldsymbol{G}_1\,\boldsymbol{u}^*_{abc}(t) + \boldsymbol{G}_2\,\boldsymbol{v}_{g,\alpha\beta}(t). \tag{4.19}$$

The system matrix $\tilde{\boldsymbol{F}} \in \mathbb{R}^{n_y \times n_y}$ and the two input matrices $\boldsymbol{G}_1 \in \mathbb{R}^{n_y \times 3}$, $\boldsymbol{G}_2 \in \mathbb{R}^{n_y \times 2}$ are derived in Appendix D.

4.3.1 Offline Computation

The computation of the reference contribution as a function of the converter voltage is based on the algorithm presented in [46]. The algorithm exploits the fact that at steady-state, the nominal switching signal is periodic, which consequently implies periodicity of the nominal waveforms of the output variables.

An OPP with quarter- and half-wave symmetry and unipolar switch positions is used for the computation. From the OPP with pulse number d and modulation index m given by the vectors A^* and U^*, the nominal three-phase switching signal over one fundamental period $\boldsymbol{u}^*_{abc}(\theta)$ is generated, see Fig. 4.6. Per phase, $4d$ switching angles occur within one fundamental period. A total of $\nu = 3 \times 4d$ switching angles are aggregated in the vector $\left[\alpha_0^*\ \alpha_1^*\ \ldots\ \alpha_\nu^*\ \alpha_{\nu+1}^*\right]^T$ in ascending order. New indices are assigned to the switching angles according to their sorted position. Note that we added the initial angle $\alpha_0^* = 0$ and the terminal angle $\alpha_{\nu+1}^* = 2\pi$ to ease the computation over one fundamental period of 2π. The three-phase switch position between two consecutive switching angles, e.g. α_i^* and α_{i+1}^*, is constant.

To calculate the reference contribution from the converter voltage, we set the grid voltage in (4.19) to zero and consider the three-phase OPP over one fundamental period $\boldsymbol{u}^*_{abc}(\theta)$ as the input signal

$$\frac{\mathrm{d}\tilde{\boldsymbol{x}}_{\mathrm{conv},\alpha\beta}(\theta)}{\mathrm{d}\theta} = \tilde{\boldsymbol{F}}\,\tilde{\boldsymbol{x}}_{\mathrm{conv},\alpha\beta}(\theta) + \boldsymbol{G}_1\,\boldsymbol{u}^*_{abc}(\theta) \tag{4.20a}$$

$$\boldsymbol{y}^*_{\mathrm{conv},\alpha\beta}(\theta) = \tilde{\boldsymbol{x}}_{\mathrm{conv},\alpha\beta}(\theta), \tag{4.20b}$$

where $\theta = \omega_g t$. For a given state vector at α^*_i, the state vector at the next switching angle α^*_{i+1} is calculated with the method of *variation of parameters* [47] by

$$\begin{aligned}\tilde{\boldsymbol{x}}_{\mathrm{conv},\alpha\beta}(\alpha^*_{i+1}) &= e^{\tilde{\boldsymbol{F}}(\alpha^*_{i+1}-\alpha^*_i)}\,\tilde{\boldsymbol{x}}_{\mathrm{conv},\alpha\beta}(\alpha^*_i) + \int_{\alpha^*_i}^{\alpha^*_{i+1}} e^{\tilde{\boldsymbol{F}}(\alpha^*_{i+1}-\theta)}\,\mathrm{d}\theta\,\boldsymbol{G}_1\boldsymbol{u}^*_{abc}(\alpha^*_i)\\ &= \tilde{\boldsymbol{A}}_i\,\tilde{\boldsymbol{x}}_{\mathrm{conv},\alpha\beta}(\alpha^*_i) + \tilde{\boldsymbol{B}}_i\,\boldsymbol{u}^*_{abc}(\alpha^*_i)\end{aligned} \tag{4.21}$$

where

$$\tilde{\boldsymbol{A}}_i = e^{\tilde{\boldsymbol{F}}(\alpha^*_{i+1}-\alpha^*_i)} \qquad \text{and} \qquad \tilde{\boldsymbol{B}}_i = \tilde{\boldsymbol{F}}^{-1}\left[\tilde{\boldsymbol{A}}_i - \boldsymbol{I}_{n_y}\right]\boldsymbol{G}_1 \tag{4.22}$$

and $i \in \{0, 1, 2, \ldots, \nu\}$. We can now use (4.21) to compute the state vector at each switching angle over one fundamental period

$$\begin{aligned}
\tilde{\boldsymbol{x}}_{\mathrm{conv},\alpha\beta}(\alpha^*_1) =& \tilde{\boldsymbol{A}}_0\,\tilde{\boldsymbol{x}}_{\mathrm{conv},\alpha\beta}(\alpha^*_0) + \tilde{\boldsymbol{B}}_0\,\boldsymbol{u}^*_{abc}(\alpha^*_0)\\
\tilde{\boldsymbol{x}}_{\mathrm{conv},\alpha\beta}(\alpha^*_2) =& \tilde{\boldsymbol{A}}_1\,\tilde{\boldsymbol{x}}_{\mathrm{conv},\alpha\beta}(\alpha^*_1) + \tilde{\boldsymbol{B}}_1\,\boldsymbol{u}^*_{abc}(\alpha^*_1)\\
=& \tilde{\boldsymbol{A}}_1\,\tilde{\boldsymbol{A}}_0\,\tilde{\boldsymbol{x}}_{\mathrm{conv},\alpha\beta}(\alpha^*_0) + \tilde{\boldsymbol{A}}_1\,\tilde{\boldsymbol{B}}_0\,\boldsymbol{u}^*_{abc}(\alpha^*_0) + \tilde{\boldsymbol{B}}_1\,\boldsymbol{u}^*_{abc}(\alpha^*_1)\\
\tilde{\boldsymbol{x}}_{\mathrm{conv},\alpha\beta}(\alpha^*_3) =& \tilde{\boldsymbol{A}}_2\,\tilde{\boldsymbol{x}}_{\mathrm{conv},\alpha\beta}(\alpha^*_2) + \tilde{\boldsymbol{B}}_2\,\boldsymbol{u}^*_{abc}(\alpha^*_2)\\
=& \tilde{\boldsymbol{A}}_2\,\tilde{\boldsymbol{A}}_1\,\tilde{\boldsymbol{A}}_0\,\tilde{\boldsymbol{x}}_{\mathrm{conv},\alpha\beta}(\alpha^*_0) + \tilde{\boldsymbol{A}}_2\,\tilde{\boldsymbol{A}}_1\,\tilde{\boldsymbol{B}}_0\,\boldsymbol{u}^*_{abc}(\alpha^*_0) + \tilde{\boldsymbol{A}}_2\,\tilde{\boldsymbol{B}}_1\,\boldsymbol{u}^*_{abc}(\alpha^*_1) + \tilde{\boldsymbol{B}}_2\,\boldsymbol{u}^*_{abc}(\alpha^*_2)\\
&\vdots\\
\tilde{\boldsymbol{x}}_{\mathrm{conv},\alpha\beta}(\alpha^*_{\nu+1}) =& \tilde{\boldsymbol{A}}_\nu\,\tilde{\boldsymbol{x}}_{\mathrm{conv},\alpha\beta}(\alpha^*_\nu) + \tilde{\boldsymbol{B}}_\nu\,\boldsymbol{u}^*_{abc}(\alpha^*_\nu)\\
=& \tilde{\boldsymbol{A}}_\nu\,\tilde{\boldsymbol{A}}_{\nu-1}\ldots\tilde{\boldsymbol{A}}_0\,\tilde{\boldsymbol{x}}_{\mathrm{conv},\alpha\beta}(\alpha^*_0) + \tilde{\boldsymbol{A}}_\nu\,\tilde{\boldsymbol{A}}_{\nu-1}\ldots\tilde{\boldsymbol{A}}_1\,\tilde{\boldsymbol{B}}_0\,\boldsymbol{u}^*_{abc}(\alpha^*_0) +\\
&\tilde{\boldsymbol{A}}_\nu\,\tilde{\boldsymbol{A}}_{\nu-1}\ldots\tilde{\boldsymbol{A}}_2\,\tilde{\boldsymbol{B}}_1\,\boldsymbol{u}^*_{abc}(\alpha^*_1) + \ldots + \tilde{\boldsymbol{A}}_\nu\,\tilde{\boldsymbol{A}}_{\nu-1}\,\tilde{\boldsymbol{B}}_{\nu-2}\,\boldsymbol{u}^*_{abc}(\alpha^*_{\nu-2}) +\\
&\tilde{\boldsymbol{A}}_\nu\,\tilde{\boldsymbol{B}}_{\nu-1}\,\boldsymbol{u}^*_{abc}(\alpha^*_{\nu-1}) + \tilde{\boldsymbol{B}}_\nu\,\boldsymbol{u}^*_{abc}(\alpha^*_\nu).
\end{aligned} \tag{4.23}$$

The terms in (4.23) containing the product of matrices $\tilde{\boldsymbol{A}}_i$ can be simplified by noting that

$$\tilde{\boldsymbol{A}}_\nu\,\tilde{\boldsymbol{A}}_{\nu-1}\ldots\tilde{\boldsymbol{A}}_i = e^{\tilde{\boldsymbol{F}}(\alpha^*_{\nu+1}-\alpha^*_\nu)}\,e^{\tilde{\boldsymbol{F}}(\alpha^*_\nu-\alpha^*_{\nu-1})}\ldots e^{\tilde{\boldsymbol{F}}(\alpha^*_{i+1}-\alpha^*_i)} = e^{\tilde{\boldsymbol{F}}(\alpha^*_{\nu+1}-\alpha^*_i)}. \tag{4.24}$$

The first term in (4.23), i.e. the term of $\tilde{\boldsymbol{A}}_i$ over one fundamental period, thus further reduces to

$$\tilde{\boldsymbol{A}}_\nu\,\tilde{\boldsymbol{A}}_{\nu-1}\ldots\tilde{\boldsymbol{A}}_0 = e^{\tilde{\boldsymbol{F}}(\alpha^*_{\nu+1}-\alpha^*_0)} = e^{\tilde{\boldsymbol{F}}2\pi}. \tag{4.25}$$

With (4.24) and (4.25), we can rewrite (4.23) as

$$\tilde{\boldsymbol{x}}_{\mathrm{conv},\alpha\beta}(\alpha^*_{\nu+1}) = e^{\tilde{\boldsymbol{F}}2\pi}\,\tilde{\boldsymbol{x}}_{\mathrm{conv},\alpha\beta}(\alpha^*_0) + \sum_{i=0}^{\nu} e^{\tilde{\boldsymbol{F}}(\alpha^*_{\nu+1}-\alpha^*_{i+1})}\,\tilde{\boldsymbol{B}}_i\,\boldsymbol{u}^*_{abc}(\alpha^*_i). \tag{4.26}$$

Due to periodicity, we know that

$$\tilde{\boldsymbol{x}}_{\mathrm{conv},\alpha\beta}(\alpha^*_0) = \tilde{\boldsymbol{x}}_{\mathrm{conv},\alpha\beta}(\alpha^*_{\nu+1}). \tag{4.27}$$

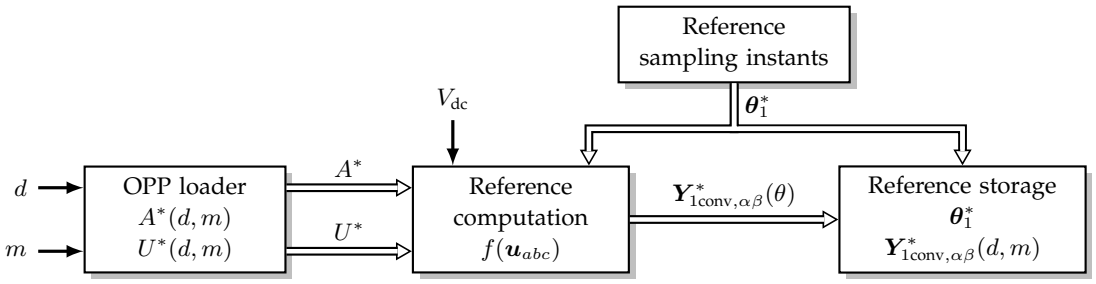

Figure 4.7: Computing the reference contribution of the converter voltage offline. For each pulse number d and modulation index m, the nominal waveforms $\boldsymbol{Y}^*_{1\mathrm{conv},\alpha\beta}(\theta)$ are stored over one fundamental period sampled at $\boldsymbol{\theta}_1^*$.

By inserting (4.26) into (4.27), we derive the initial state vector

$$\tilde{\boldsymbol{x}}_{\mathrm{conv},\alpha\beta}(\alpha_0^*) = \left[\boldsymbol{I}_{n_y} - e^{\tilde{\boldsymbol{F}}2\pi}\right]^{-1} \sum_{i=0}^{\nu} e^{\tilde{\boldsymbol{F}}(\alpha^*_{\nu+1}-\alpha^*_{i+1})}\, \tilde{\boldsymbol{B}}_i\, \boldsymbol{u}^*_{abc}(\alpha_i^*). \tag{4.28}$$

Owing to $\alpha_0^* = 0$ and (4.18), (4.28) states the nominal output vector $\boldsymbol{y}^*_{\mathrm{conv},\alpha\beta}(0)$ at the beginning of the fundamental period, where we have $\theta = 0$.

Starting with the initial state vector (4.28), the evolution of the output variables over the fundamental period can be computed. To do so, we sample the angles between 0 and 2π with the angle interval $\Delta\theta^*$. Then we compute the output variables at the reference angles $\boldsymbol{\theta}_1^* = [0\ \Delta\theta^* \ldots 2\pi]^T$ with the help of the reduced state-space model (4.20a). The reference sampling instants $\boldsymbol{\theta}_1^*$ and the resulting trajectory of nominal output vectors

$$\boldsymbol{Y}^*_{1\mathrm{conv},\alpha\beta}(\theta) = \left[\boldsymbol{y}^{*T}_{\mathrm{conv},\alpha\beta}(0)\ \ \boldsymbol{y}^{*T}_{\mathrm{conv},\alpha\beta}(\Delta\theta^*)\ \ \ldots\ \ \boldsymbol{y}^{*T}_{\mathrm{conv},\alpha\beta}(2\pi)\right]^T \tag{4.29}$$

are stored for one fundamental period in a look-up table, see Fig. 4.7. This is done for each pulse number and modulation index.

4.3.2 Online Computation

The overall reference trajectory for the pulse pattern controller contains the nominal output variables at the next N sampling instants. The reference vector is generated by performing the following three steps online:

1. Selection of the reference values within the prediction horizon from the offline computed converter voltage trajectory contribution.
2. Computation of the grid voltage trajectory contribution.
3. Superpostion of both trajectories.

The online operation is drawn as block diagram in Fig. 4.8.

Reference Selection

During online operation, the precomputed output trajectory $\boldsymbol{Y}^*_{1\mathrm{conv},\alpha\beta}(\theta)$ is loaded from the look-up table for the appropriate pulse number and modulation index. From this, the reference vectors for the next N sampling instants are obtained in the following way. First, the angular position of the converter voltage ϕ_c^* is determined from the grid voltage angle ϕ_g and the load angle γ^* according to

$$\phi_c^* = \phi_g + \gamma^*. \tag{4.30}$$

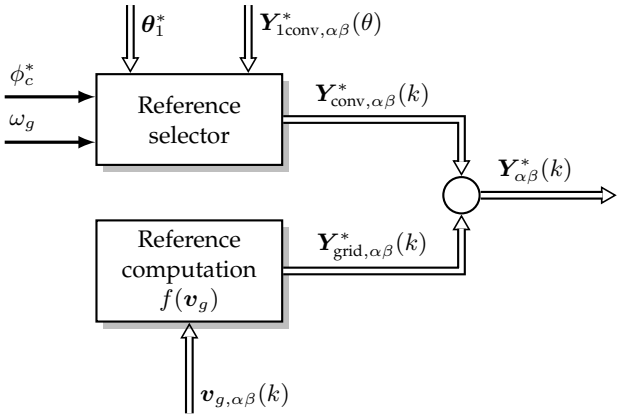

Figure 4.8: Online generation of the overall reference trajectory. Superposition of the selected converter voltage contribution and the computed grid voltage contribution. This corresponds to the reference generation block in Fig. 4.5.

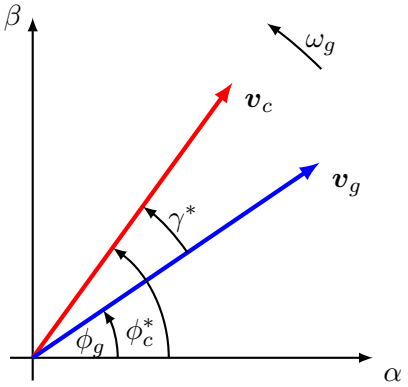

Figure 4.9: Fundamental components of the converter and grid voltage in the stationary orthogonal coordinate system. The load angle γ^* is the angle between the two voltages.

The load angle depends on the real and reactive power references, P^* and Q^*. In Fig. 4.9, the converter and grid voltages are shown in the stationary orthogonal reference frame.

Then, the nominal output vectors over the prediction horizon N

$$\boldsymbol{Y}^*_{\text{conv},\alpha\beta}(k) = \left[\boldsymbol{y}^{*T}_{\text{conv},\alpha\beta}(k+1)\ \ \boldsymbol{y}^{*T}_{\text{conv},\alpha\beta}(k+2)\ \ \ldots\ \ \boldsymbol{y}^{*T}_{\text{conv},\alpha\beta}(k+N)\right]^T \tag{4.31}$$

are computed by interpolation. This concept is explained in Fig. 4.10. Note that the outputs at the current time step k are not required.

Reference Trajectory Contribution of Grid Voltage

For the computation of the reference trajectory as a function of the grid voltage, a perfect sinusoidal grid voltage is assumed. We introduce the corresponding state vector $\tilde{\boldsymbol{x}}_{\text{grid},\alpha\beta}$. The grid voltage is given in stationary orthogonal $\alpha\beta$ coordinates by

$$\boldsymbol{v}_{g,\alpha\beta}(t) = \hat{v}_g \begin{bmatrix} \sin(\omega_g t - \phi_g) \\ -\cos(\omega_g t - \phi_g) \end{bmatrix}, \tag{4.32}$$

where $\hat{v}_g$ is the amplitude of the grid voltage. It follows that all state variables are sinusoidal signals with the grid frequency ω_g. Each pair of state variables in stationary orthogonal coordinates is then described by

$$\boldsymbol{\xi}_{\alpha\beta}(t) = \hat{\xi} \begin{bmatrix} \sin(\omega_g t - \phi_\xi) \\ -\cos(\omega_g t - \phi_\xi) \end{bmatrix} \tag{4.33}$$

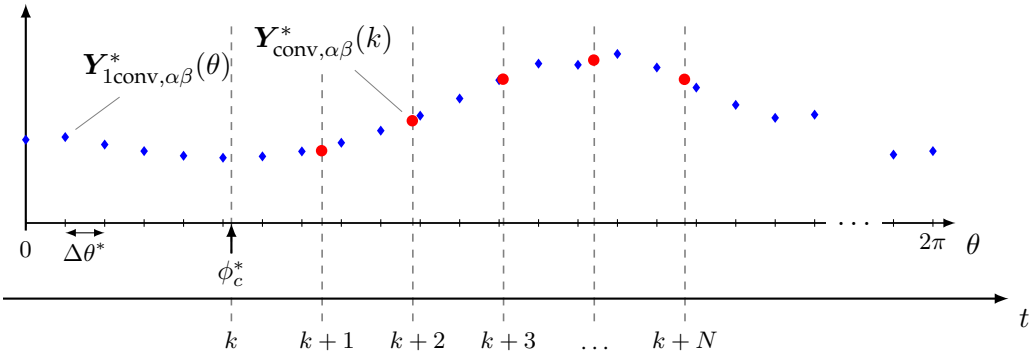

Figure 4.10: Interpolation of the reference trajectory $\boldsymbol{Y}^*_{\text{conv},\alpha\beta}(k)$ at the sampling instants $k+1,\ldots,k+N$ from the precomputed output trajectory $\boldsymbol{Y}^*_{1\text{conv},\alpha\beta}(\theta)$.

and evolves according to the differential equation

$$\frac{\mathrm{d}\boldsymbol{\xi}_{\alpha\beta}(t)}{\mathrm{d}t} = \omega_g \begin{bmatrix} 0 & -1 \\ 1 & 0 \end{bmatrix} \boldsymbol{\xi}_{\alpha\beta}(t). \tag{4.34}$$

With this, we can explicitly state the derivative of the state vector and rewrite (4.19) as

$$\omega_g \underbrace{\begin{bmatrix} \begin{bmatrix} 0 & -1 \\ 1 & 0 \end{bmatrix} & \mathbf{0}_2 & \mathbf{0}_2 \\ \mathbf{0}_2 & \begin{bmatrix} 0 & -1 \\ 1 & 0 \end{bmatrix} & \mathbf{0}_2 \\ \mathbf{0}_2 & \mathbf{0}_2 & \begin{bmatrix} 0 & -1 \\ 1 & 0 \end{bmatrix} \end{bmatrix}}_{\boldsymbol{R}} \tilde{\boldsymbol{x}}_{\text{grid},\alpha\beta}(t) = \tilde{\boldsymbol{F}}\, \tilde{\boldsymbol{x}}_{\text{grid},\alpha\beta}(t) + \boldsymbol{G}_2\, \boldsymbol{v}_{g,\alpha\beta}(t), \tag{4.35}$$

where the switching signal, and thus the converter voltage, was set to zero. Note that $\mathbf{0}_2$ is the 2×2 zero matrix. By rearranging (4.35), we obtain the nominal output vector

$$\boldsymbol{y}^*_{\text{grid},\alpha\beta}(k) = \left[\boldsymbol{R} - \tilde{\boldsymbol{F}}\right]^{-1} \boldsymbol{G}_2\, \boldsymbol{v}_{g,\alpha\beta}(k). \tag{4.36}$$

as a function of the grid voltage, where we have used (4.18). The trajectory contribution of the grid voltage over the prediction horizon follows as

$$\boldsymbol{Y}^*_{\text{grid},\alpha\beta}(k) = \left[\boldsymbol{y}^{*T}_{\text{grid},\alpha\beta}(k+1)\ \ \boldsymbol{y}^{*T}_{\text{grid},\alpha\beta}(k+2)\ \ \ldots\ \ \boldsymbol{y}^{*T}_{\text{grid},\alpha\beta}(k+N)\right]^T. \tag{4.37}$$

Superposition

By superposition, the overall resulting reference trajectory of the system is derived as

$$\boldsymbol{Y}^*_{\alpha\beta}(k) = \boldsymbol{Y}^*_{\text{conv},\alpha\beta}(k) + \boldsymbol{Y}^*_{\text{grid},\alpha\beta}(k), \tag{4.38}$$

which contains the output vectors for the next N sampling instants

$$\boldsymbol{Y}^*_{\alpha\beta}(k) = \left[\boldsymbol{y}^{*T}_{\alpha\beta}(k+1)\ \ \boldsymbol{y}^{*T}_{\alpha\beta}(k+2)\ \ \ldots\ \ \boldsymbol{y}^{*T}_{\alpha\beta}(k+N)\right]^T. \tag{4.39}$$

This trajectory includes the offline computed contribution from the OPP and the online computed contribution from the grid voltage. It will be used by the controller as a *reference* for the output variables over the prediction horizon.

Fig. 4.11 shows examples of the reference trajectories in the stationary reference frame for one fundamental period obtained from the example OPP shown in Fig. 4.6.

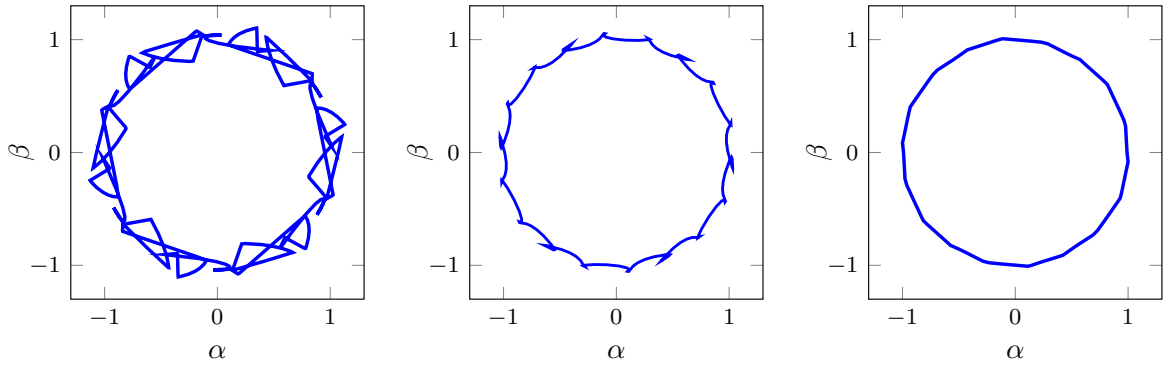

(a) Converter current (b) Capacitor voltage (c) Grid current

Figure 4.11: Reference trajectories of the output variables in $\alpha\beta$ coordinates and in per unit.

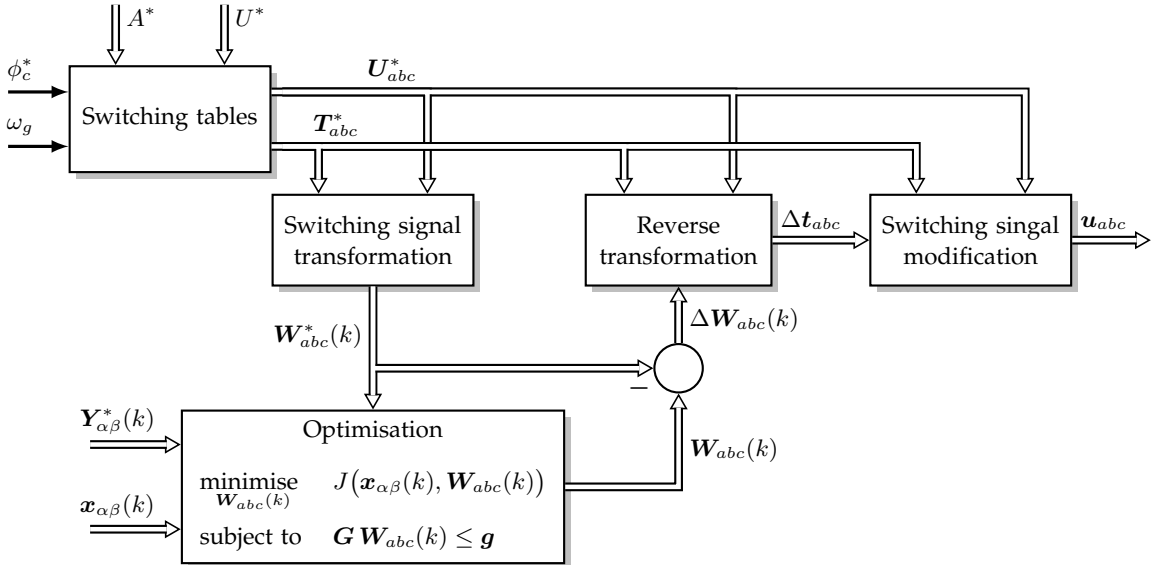

Figure 4.12: Inner loop of MP^{3}C$^+$: the pulse pattern controller with integrated modulator stage. This corresponds to the pulse pattern controller block in Fig. 4.5.

4.4 Pulse Pattern Controller

The pulse pattern controller modifies the switching instants of precomputed OPPs in order to regulate the output variables along their optimal reference trajectories. The pulse pattern controller is shown in the block diagram in Fig. 4.12. The single blocks are described in detail hereafter.

4.4.1 Switching Tables

The switching tables $\boldsymbol{T}^*_{abc}$ and $\boldsymbol{U}^*_{abc}$ define the three-phase nominal switching signal $\boldsymbol{u}^*_{abc}(t)$ over the prediction horizon, and are generated using the single-phase vectors A^* and U^*, which define the OPP. The ith switching angle is translated into a switching time by

$$t^*_{pi} = \frac{\alpha^*_{pi}}{\omega_g}, \tag{4.40}$$

where ω_g denotes the angular grid frequency. The current position within the fundamental period is given by $kT_s = \frac{\phi_c^*}{\omega_g}$. The switching transitions that fall within the prediction horizon,

i.e. $kT_s \leq t^*_{pi} \leq (k+N)T_s$ with $p \in \{a,b,c\}$ and $i \in \{1,\ldots,n_p\}$, are identified. Note that n_p is the number of switching transitions within the prediction horizon in phase p. Their nominal switching time t^*_{pi} and switch position u^*_{pi} are stored in the switching tables as follows

$$\boldsymbol{T}^*_{abc} = \begin{bmatrix} t^*_{a1} & t^*_{b1} & t^*_{c1} \\ t^*_{a2} & t^*_{b2} & t^*_{c2} \\ \vdots & \vdots & \vdots \\ t^*_{an_a} & t^*_{bn_b} & t^*_{cn_c} \end{bmatrix} \quad \text{and} \quad \boldsymbol{U}^*_{abc} = \begin{bmatrix} u^*_{a1} & u^*_{b1} & u^*_{c1} \\ u^*_{a2} & u^*_{b2} & u^*_{c2} \\ \vdots & \vdots & \vdots \\ u^*_{an_a} & u^*_{bn_b} & u^*_{cn_c} \end{bmatrix}. \tag{4.41}$$

4.4.2 Switching Signal Transformation

For the switching signal transformation, each phase is considered separately. The nominal switching signal $u^*_p(t)$ in phase p with $p \in \{a,b,c\}$, which is constructed from the nominal switching tables $\boldsymbol{T}^*_{abc}$ and $\boldsymbol{U}^*_{abc}$, is shown in Fig. 4.13a. In each sampling interval ℓT_s with $\ell = k,\ldots,k+N-1$ within the prediction horizon, a specific number of switching instants occurs. Let n_{pk} be the number of switching instants occurring within the kth sampling interval $t \in [kT_s,\ (k+1)T_s]$

$$kT_s \leq t^*_{p1} \leq t^*_{p2} \leq \ldots \leq t^*_{pn_{pk}} \leq (k+1)T_s, \tag{4.42}$$

where t^*_{pi} defines the nominal switching time of the ith switching instant with $i \in \{1,\ldots,n_{pk}\}$ in the kth sampling interval.

For simplification in the derivation, we rename the interval limits to

$$t^*_{p0} = kT_s \qquad \text{and} \qquad t^*_{p,n_{pk}+1} = (k+1)T_s. \tag{4.43}$$

By averaging the nominal switching signal $u^*_p(t)$ over the kth sampling interval, the equivalent averaged switch position $w^*_p(k)$ is obtained

$$w^*_p(k) = \frac{1}{T_s}\int_{kT_s}^{(k+1)T_s} u^*_p(t)\,\mathrm{d}t. \tag{4.44}$$

Recall that the switching signal has the constant switch position u^*_{pi} between the switching instants t^*_{pi} and $t^*_{p,i+1}$. With this, we split the integral in (4.44) into $n_{pk}+1$ intervals of constant switch position and obtain

$$\begin{aligned} w^*_p(k) &= \frac{1}{T_s}\int_{t^*_{p0}}^{t^*_{p1}} u^*_{p0}\,\mathrm{d}t + \frac{1}{T_s}\int_{t^*_{p1}}^{t^*_{p2}} u^*_{p1}\,\mathrm{d}t + \ldots + \frac{1}{T_s}\int_{t^*_{pn_{pk}}}^{t^*_{p,n_{pk}+1}} u^*_{pn_{pk}}\,\mathrm{d}t \\ &= \sum_{i=0}^{n_{pk}} \frac{1}{T_s}\int_{t^*_{pi}}^{t^*_{p,i+1}} u^*_{pi}\,\mathrm{d}t. \end{aligned} \tag{4.45}$$

Solving the integral gives

$$w^*_p(k) = \sum_{i=0}^{n_{pk}} \frac{t^*_{p,i+1} - t^*_{pi}}{T_s} u^*_{pi}, \tag{4.46}$$

which states the general transformation law for the kth sampling interval of the single-phase switching signal with n_{pk} switching transitions from the continuous-time to the discrete-time domain.

Note that when $n_{pk} = 0$, there is no switching transition occurring within the kth sampling interval. Thus, the interval limits $t^*_{p0} = kT_s$ and $t^*_{p1} = (k+1)T_s$ are inserted in (4.46), which yields

$$w^*_p(k) = u^*_{p0}. \tag{4.47}$$

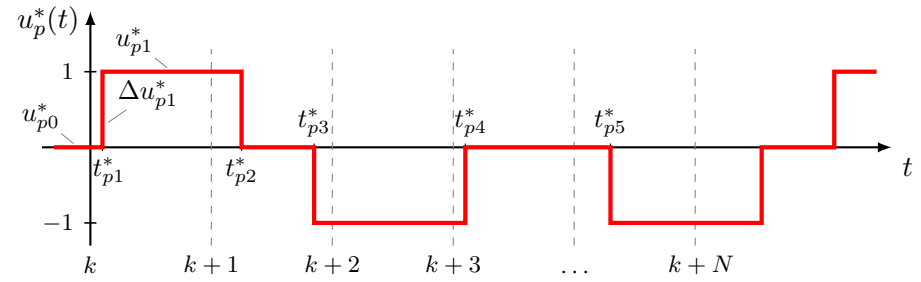

(a) Nominal continuous-time switching signal.

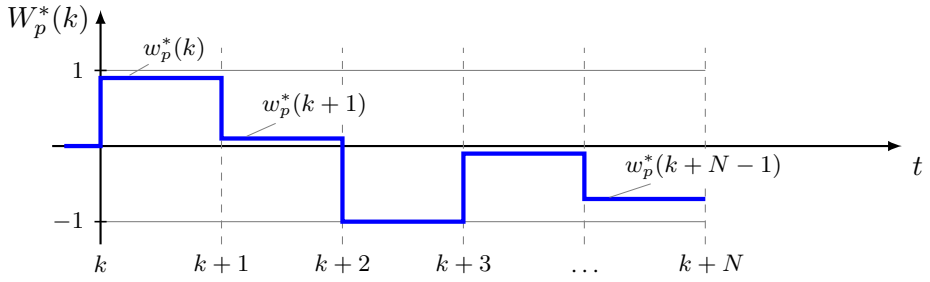

(b) Sequence of nominal averaged switch positions.

Figure 4.13: The nominal switching signal is divided in N sampling intervals over the prediction horizon. In each sampling interval, the switching signal is transformed to an averaged switch position.

This implies, as expected, that the averaged switch position corresponds to the integer switch position of the nominal OPP during that sampling interval.

The nominal averaged switch positions in the kth sampling interval of each phase are aggregated in the nominal averaged three-phase switch position $\boldsymbol{w}_{abc}^*(k) = \left[w_a^*(k)\ w_b^*(k)\ w_c^*(k)\right]^T$. Transforming the switching signal in each sampling interval within the prediction horizon yields the sequence of nominal averaged three-phase switch positions

$$\boldsymbol{W}_{abc}^*(k) = \left[\boldsymbol{w}_{abc}^{*T}(k)\ \ \boldsymbol{w}_{abc}^{*T}(k+1)\ \ \ldots\ \ \boldsymbol{w}_{abc}^{*T}(k+N-1)\right]^T. \tag{4.48}$$

In Fig. 4.13b, the sequence of averaged switch positions is shown that results from transforming the example switching signal of Fig. 4.13a.

4.4.3 Constraints on the Averaged Switching Signal

We require that in each phase the order of switching instants in the switching signal remains unchanged. Consider the switching signal in phase p and assume n_{pk} switching transitions in the kth sampling interval. To maintain the switching instant order, we impose the constraint

$$kT_s \leq t_{p1} \leq t_{p2} \leq \ldots \leq t_{pn_{pk}} \leq (k+1)T_s \tag{4.49}$$

on the modified switching instants t_{pi} in each phase. Between the three phases, no constraint is imposed. This constraint on the switching times restricts the switching instants to their corresponding sampling intervals, i.e. that sampling interval in which the corresponding nominal switching time lies, see Fig. 4.14a. Next, we translate these constraints into constraints on the averaged switch positions $w_p(k)$. We impose on the averaged switch position the constraint

$$\underline{w}_p(k) \leq w_p(k) \leq \overline{w}_p(k), \tag{4.50}$$

where $\underline{w}_p(k)$ is the lower bound on the manipulated variable $w_p(k)$, and $\overline{w}_p(k)$ is its upper bound. Consider the case when all n_{pk} switching instants in the sampling interval k are placed

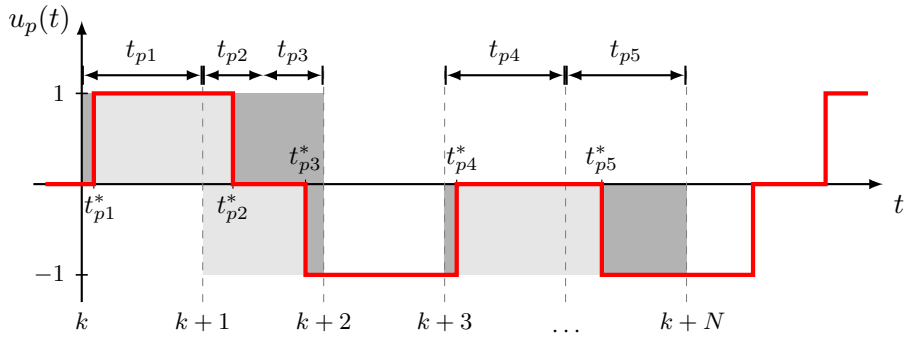

(a) Constraints on the switching times of the continuous-time switching signal.

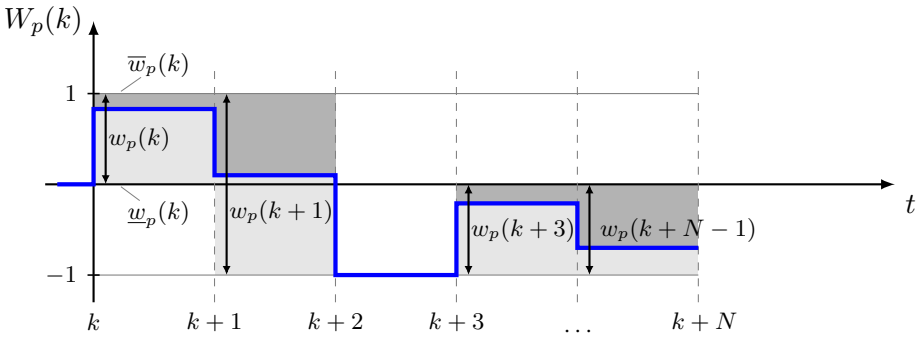

(b) Corresponding constraints on the averaged switch positions.

Figure 4.14: The upper and lower bounds on the averaged switch position follow from the maximum and minimum value of the switching signal in the corresponding sampling interval.

at the lower (upper) bound. Depending on the corresponding switching transitions, the switching signal $u_p(t)$ adopts either the lowest or highest switch position in that sampling interval $t \in [kT_s,\ (k+1)T_s]$. It follows that the bounds in (4.50) are directly given by the lowest (highest) switch position of the continuous-time switching signal in the respective sampling interval

$$\underline{w}_p(k) = \min_{t\,\in\,[kT_s,\ (k+1)T_s]} u_p(t) \qquad \text{and} \qquad \overline{w}_p(k) = \max_{t\,\in\,[kT_s,\ (k+1)T_s]} u_p(t) \tag{4.51}$$

These definitions hold true independent of the number of switching transitions in that sampling interval, see Fig. 4.14.

4.4.4 System Model

The continuous-time system (4.15) is sampled with the sampling interval T_s. Applying the constant averaged switch position $\boldsymbol{w}_{abc}(k)$ in the sampling interval, the discrete-time system model is obtained

$$\boldsymbol{x}_{\alpha\beta}(k+1) = \boldsymbol{A}\,\boldsymbol{x}_{\alpha\beta}(k) + \boldsymbol{B}\,\boldsymbol{w}_{abc}(k) \tag{4.52a}$$

$$\boldsymbol{y}_{\alpha\beta}(k) = \boldsymbol{C}\,\boldsymbol{x}_{\alpha\beta}(k) \tag{4.52b}$$

by exact discretisation, with

$$\boldsymbol{A} = e^{\boldsymbol{F}\,T_s} \qquad \text{and} \qquad \boldsymbol{B} = \boldsymbol{F}^{-1}\left(\boldsymbol{A} - \boldsymbol{I}_{n_x}\right)\boldsymbol{G}, \tag{4.53}$$

where $\boldsymbol{I}_{n_x}$ is the identity matrix of the size $n_x \times n_x$.

4.4.5 Optimisation Stage

A constrained optimisation problem is formulated based on the measured (or estimated) state vector $\boldsymbol{x}_{\alpha\beta}(k)$, the reference trajectory $\boldsymbol{Y}^*_{\alpha\beta}(k)$, the sequence of nominal averaged switch positions $\boldsymbol{W}^*_{abc}(k)$, and the discrete-time system model (4.52). The optimisation variable is the sequence of averaged switch positions

$$\boldsymbol{W}_{abc}(k) = \left[\boldsymbol{w}^T_{abc}(k) \;\; \boldsymbol{w}^T_{abc}(k+1) \;\; \dots \;\; \boldsymbol{w}^T_{abc}(k+N-1)\right]^T. \tag{4.54}$$

Cost Function The cost function of the MP^{3}C$^+$ optimisation problem

$$J\big(\boldsymbol{W}_{abc}(k)\big) = \sum_{\ell=k}^{k+N-1} \left\|\boldsymbol{y}^*_{\alpha\beta}\left(\ell+1\right) - \boldsymbol{y}_{\alpha\beta}\left(\ell+1\right)\right\|^2_{\boldsymbol{Q}} + \lambda_w \|\boldsymbol{w}^*_{abc}(\ell) - \boldsymbol{w}_{abc}(\ell)\|^2_2 \tag{4.55}$$

is a function of the sequence of averaged switch positions over the prediction horizon, $\boldsymbol{W}_{abc}(k)$. The tracking error $\boldsymbol{y}^*_{\alpha\beta}(\ell+1) - \boldsymbol{y}_{\alpha\beta}(\ell+1)$ is the difference between the optimal steady-state reference trajectory, computed in (4.39), and the predicted output variables, which are obtained from the discrete-time system model (4.52) using $\boldsymbol{W}_{abc}(k)$ as the input. The positive definite penalty matrix $\boldsymbol{Q} \in \mathbb{R}^{n_y \times n_y}$ adjusts the weight on the tracking error for each output variable. Note that $\|\boldsymbol{\xi}\|^2_{\boldsymbol{Q}} = \boldsymbol{\xi}^T\boldsymbol{Q}\boldsymbol{\xi}$. The definition of positive definite matrices was given in Section 2.4.3.

The control effort corresponds to the degree with which the averaged switch positions are modified. We define it as the 2-norm of $\boldsymbol{w}^*_{abc}(\ell) - \boldsymbol{w}_{abc}(\ell)$, i.e. of the difference between the nominal and the modified averaged switch position. The control effort is penalised with the scalar weight $\lambda_w > 0$.

Constraints The previously derived constraints on the averaged switch positions in each phase and sampling interval are added to the optimisation problem. To do so, we use Algorithm 1.

Algorithm 1 Switching signal constraint

for $p \in \{a, b, c\}$ **do**
  for $\ell = k$ to $k + N - 1$ **do**
    if $\nexists\, i$ such that $\ell T_s \le t_{pi} \le (\ell+1)T_s, \;\; i \in \{1, \dots, n_p\}$ **then**
      $w_p(\ell) = u_p(\ell T_s)$
    else
      $\underline{w}_p(\ell) \le w_p(\ell) \le \overline{w}_p(\ell)$ with $\underline{w}_p(\ell) = \min_{t \in [\ell T_s,\ (\ell+1)T_s]} u_p(t)$
      and $\overline{w}_p(\ell) = \max_{t \in [\ell T_s,\ (\ell+1)T_s]} u_p(t)$
    end if
  end for
end for

We aggregate the upper bounds on the averaged switching signals in the vector

$$\overline{\boldsymbol{W}}_{abc}(k) = \Big[\overline{w}_a(k)\, \overline{w}_b(k)\, \overline{w}_c(k) \dots \; \overline{w}_a(k+N-1) \;\; \overline{w}_b(k+N-1) \;\; \overline{w}_c(k+N-1)\Big]^T. \tag{4.56}$$

The lower bounds are aggregated accordingly in the vector $\underline{\boldsymbol{W}}_{abc}(k)$. This allows us to derive the general formulation for the constraints

$$\boldsymbol{G}\, \boldsymbol{W}_{abc}(k) \le \boldsymbol{g}, \tag{4.57}$$

with

$$\boldsymbol{G} = \begin{bmatrix} \boldsymbol{I}_{3N} \\ -\boldsymbol{I}_{3N} \end{bmatrix} \qquad \text{and} \qquad \boldsymbol{g} = \begin{bmatrix} \overline{\boldsymbol{W}}_{abc}(k) \\ -\underline{\boldsymbol{W}}_{abc}(k) \end{bmatrix}. \tag{4.58}$$

Note that $\boldsymbol{I}_{3N}$ denotes the identity matrix of the size $3N \times 3N$.

Quadratic Program The cost function J in (4.55), the inequality constraints (4.57) and the discrete-time system model (4.52) form the basis to formulate the optimisation problem underlying MP^{3}C$^+$. As shown in Appendix E, the quadratic program (QP)

$$\begin{aligned} \boldsymbol{W}_{abc}(k) = \underset{\boldsymbol{W}_{abc}(k)}{\text{arg minimise}} \quad & \frac{1}{2}\boldsymbol{W}_{abc}^T(k)\,\boldsymbol{H}\,\boldsymbol{W}_{abc}(k) + \boldsymbol{\Theta}^T(k)\,\boldsymbol{W}_{abc}(k) \\ \text{subject to} \quad & \boldsymbol{G}\,\boldsymbol{W}_{abc}(k) \leq \boldsymbol{g} \end{aligned} \tag{4.59}$$

results, where the Hessian matrix $\boldsymbol{H} \in \mathbb{R}^{3N\times 3N}$ and the parameter vector $\boldsymbol{\Theta} \in \mathbb{R}^{3N}$ are defined in (E.6) and (E.7), respectively. The Hessian is positive definite, as $\boldsymbol{Q}$ is positive definite and $\lambda_w > 0$. Thus, the QP (4.59) is convex and can be solved efficiently in real-time. For more information on convex QPs and solvers, the interested reader is referred to [18]. By solving the QP at time step k, we obtain the optimal sequence of averaged three-phase switching signals over the prediction horizon $\boldsymbol{W}_{abc}(k)$.

4.4.6 Reverse Transformation

By subtracting the sequence of nominal averaged switch positions, the sequence of optimal averaged switch position *modifications*

$$\begin{aligned} \Delta\boldsymbol{W}_{abc}(k) &= \boldsymbol{W}_{abc}(k) - \boldsymbol{W}^*_{abc}(k) \\ &= \left[\Delta\boldsymbol{w}^T_{abc}(k)\ \ \Delta\boldsymbol{w}^T_{abc}(k+1)\ \ldots\ \Delta\boldsymbol{w}^T_{abc}(k+N-1)\right]^T \end{aligned}$$

results. These are modifications to be applied in each sampling interval in the prediction horizon and for each phase. The sequence of switching signal modifications $\Delta\boldsymbol{W}_{abc}(k)$ in the discrete-time domain is translated back into switching time modifications

$$\Delta\boldsymbol{t}_{abc} = [\Delta t_{a1}\ \Delta t_{a2}\ \ldots\ \Delta t_{an_a}\ \Delta t_{b1}\ \ldots\ \Delta t_{bn_b}\ \Delta t_{c1}\ \ldots\ \Delta t_{cn_c}]^T \tag{4.60}$$

in the continuous-time domain. This is done separately for each phase and for each sampling interval within the prediction horizon, see Fig. 4.15. Let $\Delta w_p(k)$ denote the averaged switch position modification in the kth sampling interval in phase p, in which n_{pk} switching transitions occur. This modification $\Delta w_p(k)$ must correspond to the n_{pk} switching time modifications Δt_{pi}, with $i \in \{1, 2, \ldots, n_{pk}\}$ in that sampling interval and phase. As derived in Appendix F, the following relationship holds true

$$\Delta w_p(k) T_s = -\sum_{i=1}^{n_{pk}} \Delta t_{pi} \Delta u_{pi}. \tag{4.61}$$

To compute the switching instant modifications we formulate and solve the linear optimisation problem

$$\underset{\left[\Delta t_{p1}\ldots\Delta t_{pn_{pk}}\right]^T}{\text{minimise}} \quad \sum_{i=1}^{n_{pk}} |\Delta t_{pi}| \tag{4.62a}$$

$$\text{subject to} \quad \Delta w_p(k) = -\sum_{i=1}^{n_{pk}} \frac{\Delta t_{pi}}{T_s} \Delta u_{pi} \tag{4.62b}$$

$$kT_s \leq t^*_{p1} + \Delta t_{p1} \leq \ldots \leq t^*_{pn_{pk}} + \Delta t_{pn_{pk}} \leq (k+1)T_s, \tag{4.62c}$$

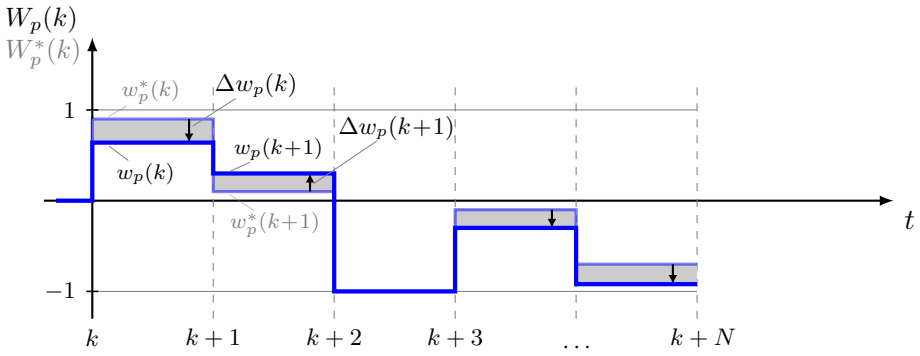

(a) Averaged switch position modifications.

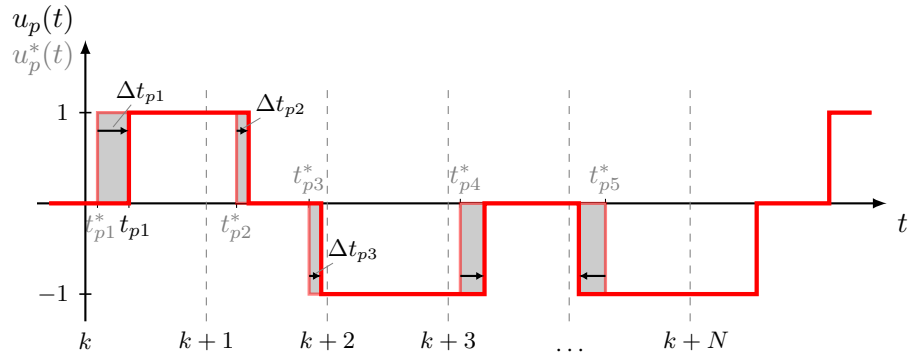

(b) Translated switching time modifications.

Figure 4.15: The averaged switch position modifications are translated into switching time modifications for each switching instant in the corresponding sampling interval.

which is a so-called linear program (LP). The objective is to minimise the switching time modification, which is achieved by penalising them with the 1-norm. The constraint (4.62b) ensures that the averaged switch position modification $\Delta w_p(k)$ is entirely applied to the continuous-time switching signal $u_p(t)$ in the kth sampling interval. Recall the constraint (4.49) on the modified switching transitions, which ensures that the order of the switching transitions is kept and that the switching instants are restricted to their corresponding sampling intervals. With the help of $t_{pi} = t_{pi}^* + \Delta t_{pi}$ the constraint (4.62c) directly follows. Solving the LP results in the vector of switching instant modifications $\left[\Delta t_{p1}\ \Delta t_{p2} \dots \Delta t_{pn_{pk}}\right]^T$ in the kth sampling interval in phase p.

4.4.7 Switching Signal Modification

With the vector of switching time modifications $\Delta \boldsymbol{t}_{abc}$ and the nominal switching times in the switching table $\boldsymbol{T}_{abc}^*$, the modified switching times are obtained with the help of

$$t_{pi} = t_{pi}^* + \Delta t_{pi}. \tag{4.63}$$

From these modified switching times, the ones occurring within the current sampling interval are selected, i.e. $kT_s \leq t_{pi} \leq (k+1)T_s$. With the corresponding switch positions stored in the switching table $\boldsymbol{U}_{abc}^*$, the modified switching signal $\boldsymbol{u}_{abc}$ for the current sampling interval is created.

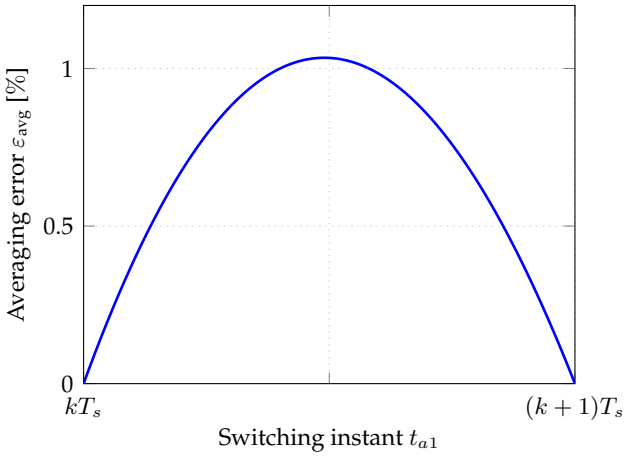

Figure 4.16: Averaging error in dependence of the switching time t_{a1} within a sampling interval.

4.5 Control Characteristics

One key characteristic of the described MPC problem is the minimisation of the weighted tracking error between the reference and the predicted behaviour of the system. In MP^{3}C$^+$, the reference is computed from the OPP with the help of the continuous-time system model (4.19), while the predictions are computed by the discrete-time model (4.52) with averaged switch positions, which are the transformed OPP. Due to the averaging of the OPP, the discrete-time model produces an *averaging error* in the internal system predictions of MP^{3}C$^+$. For a better understanding, consider the system as described in the case study over one sampling interval T_s. The switching signals in phase b and c are constant, while in phase a there is one switching instant at t_{a1} within the sampling interval $t_{a1} \in [kT_s, (k+1)T_s]$. The system outputs at the beginning of the sampling interval are $\boldsymbol{y}(k)$. Based on this the exact system outputs $\boldsymbol{y}_{\text{cont}}(k+1)$ at the next sampling instant $(k+1)T_s$ can be computed with the continuous-time model. Transforming the switching signal to an averaged switch position, the averaged system outputs $\boldsymbol{y}_{\text{avg}}(k+1)$ are computed with the discrete-time model. We define the normalised averaging error as

$$\varepsilon_{\text{avg}} = \frac{\|\boldsymbol{y}_{\text{cont}}(k+1) - \boldsymbol{y}_{\text{avg}}(k+1)\|_2}{\|\boldsymbol{y}_{\text{cont}}(k+1)\|_2} \cdot 100. \tag{4.64}$$

In Fig 4.16, the normalised averaging error is plotted in dependence of the switching time t_{a1}, which is varied within the sampling interval. For this example, the system of the case study was assumed to be in steady-state and the sampling interval was chosen to $T_s = 200\,\mu\text{s}$. It should be clear that when the switching instant occurs at the interval limits, the averaged model exactly predicts the system behaviour and the averaging error is zero. The maximum averaging error arises when the switching transition occurs in the middle of the sampling interval. We can conclude from the figure that the maximum averaging error is proportional to the sampling frequency.

Note that the averaging error is relatively small. While it is present at steady-state and during transients, the impact on the controller operation is noticeable only at steady-state. Based on the slightly divergent predictions resulting from the nominal averaged switch positions, the controller identifies this averaging error as tracking error. As a result, the computed optimal solution leads to slight modifications of the switching signal. A small sampling interval is thus favourable to avoid these unnecessary modifications to the optimal continuous-time OPP.

Choosing the sampling interval too short, however, restricts the capability of MP^{3}C$^+$ during transients. Recall that the controller can modify the switching instants only within their respective sampling intervals (4.49). Therefore, reducing the sampling interval overly restricts

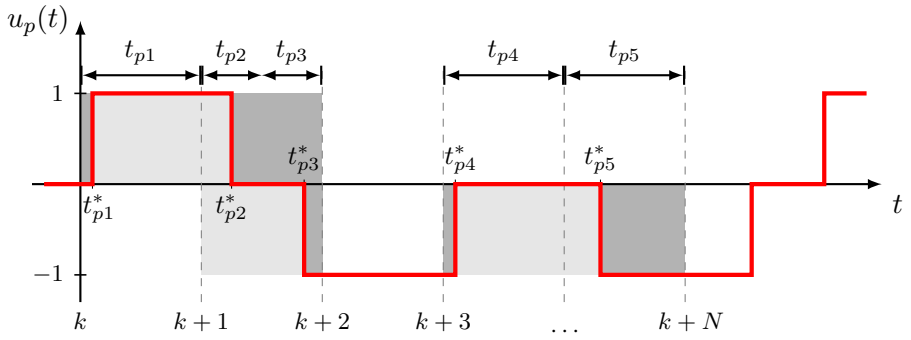

(a) Available control actions with long sampling intervals T_s.

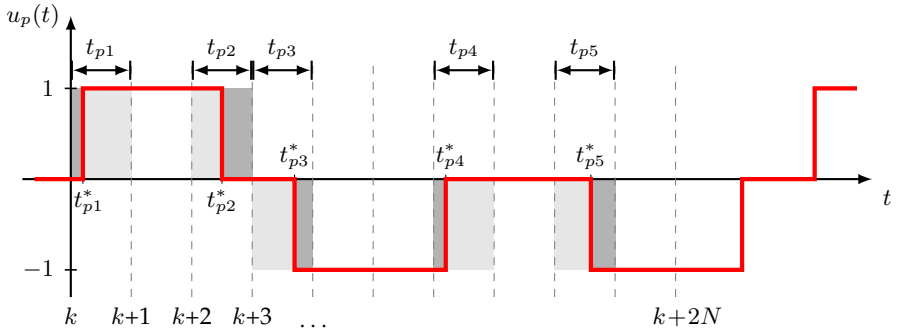

(b) Available control actions with short sampling intervals $\frac{T_s}{2}$.

Figure 4.17: A short sampling interval reduces the capability of the controller to correct tracking errors quickly. Due to the increased restriction of each switching instant, more switching instants are required to reduce a large tracking error.

the available control actions as illustrated in Fig. 4.17. The single-phase switching signal $u_p(t)$ is sampled once with T_s and once with $\frac{T_s}{2}$. In both cases, the same number of switching instants is available for modification, because the prediction horizon is increased to $2N$ for the latter case. From the indicated maximal allowed modification for each switching instant, the limited available control actions are clearly recognisable in the second case.

Choosing the sampling interval in MP^{3}C$^+$ is thus a trade-off between the amount of available control actions during transients and the averaging error at steady-state. In general, a long sampling interval is the preferable choice as the steady-state control benefits from the receding horizon policy. This policy is illustrated in Fig. 4.18. Again the system of the described case study at steady-state is assumed.

At time step kT_s, the controller derives the optimal sequence of averaged switch positions $\boldsymbol{W}_{abc}(k)$, which give the output predictions $\boldsymbol{Y}_{\alpha\beta}(k)$ over the prediction horizon based on the measured state vector $\boldsymbol{x}_{\alpha\beta}(k)$. The corresponding weighted tracking error $\left\|\boldsymbol{Y}^*_{\alpha\beta}(k) - \boldsymbol{Y}_{\alpha\beta}(k)\right\|^2_{\tilde{\boldsymbol{Q}}}$ and the switching effort $\lambda_w \|\boldsymbol{W}^*_{abc}(k) - \boldsymbol{W}_{abc}(k)\|_2^2$ over the prediction horizon are shown in Fig. 4.18a. The predicted tracking error and switching error at the next sampling instant $(k+1)T_s$ are shown in Fig. 4.18b. We can see from the figures that the measured state vector at time step $k+1$ is smaller than predicted, which also leads to reductions of the predicted tracking error over the next sampling steps. Due to the continuous feedback of the actual system behaviour, the controller can adjust the manipulated variable at each sampling step.

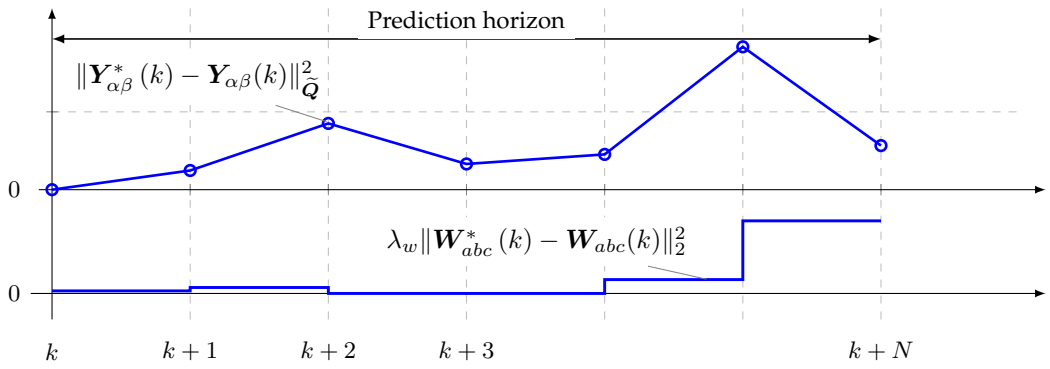

(a) Predictions at $t = kT_s$.

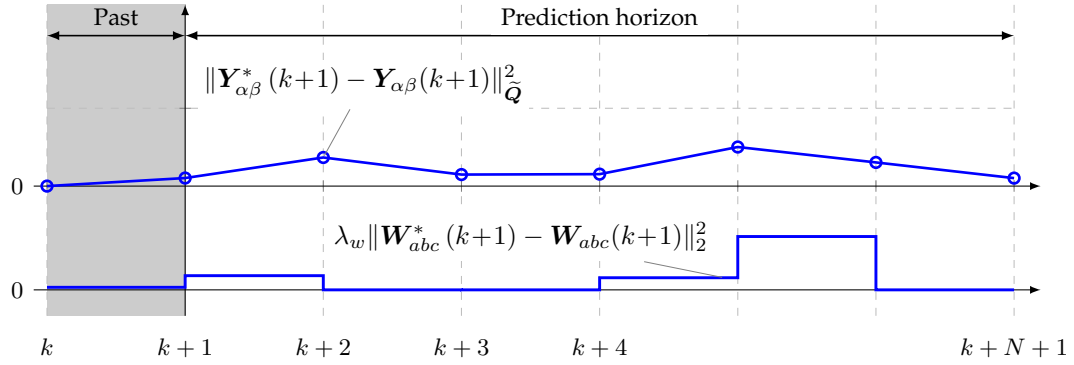

(b) Predictions at $t = (k+1)T_s$.

Figure 4.18: The receding horizon policy reduces the impact of the averaging error on the controller predictions.

4.6 Performance Evaluation

The controller performance is evaluated with MATLAB simulations considering the case study described in Section 4.1.3 at steady-state and during transients. The sampling frequency is set to $T_s = 200\,\mu\text{s}$, and a relatively long prediction horizon of $N = 15$ steps is used. The penalty matrix and the scalar weight in the cost function are chosen as

$$\boldsymbol{Q} = \text{diag}(0.1, 0.1, 5, 5, 12, 12) \quad \text{and} \quad \lambda_w = 0.016.$$

This selection of weights implies that the grid currents have the highest priority, followed by the capacitor voltages, and then the converter currents. This means that during transients the controller attempts to drive the grid currents towards their steady-state trajectories faster than the other quantities. The QP (4.59) is solved using the `quadprog` solver of the Optimization Toolbox of MATLAB. The pulse number is set to $d = 5$, which results in a switching frequency of $f_{\text{sw}} = 250\,\text{Hz}$ per semiconductor device for the $50\,\text{Hz}$ grid frequency.

4.6.1 Steady-state Behaviour

Consider steady-state operation at rated real power $P^* = 1\,\text{pu}$ and zero reactive power $Q^* = 0\,\text{pu}$. This implies operation at the modulation index $m = 1.12$. The corresponding OPP is shown in Fig. 4.6, and the references for the output trajectories are depicted in Fig. 4.11.

The steady-state performance of the controller is shown in Fig. 4.19. The nominal OPP and the reference signals are shown as dotted lines, whereas the modified OPP and the actual output signals are shown as solid lines. It can be seen that the nominal and actual output

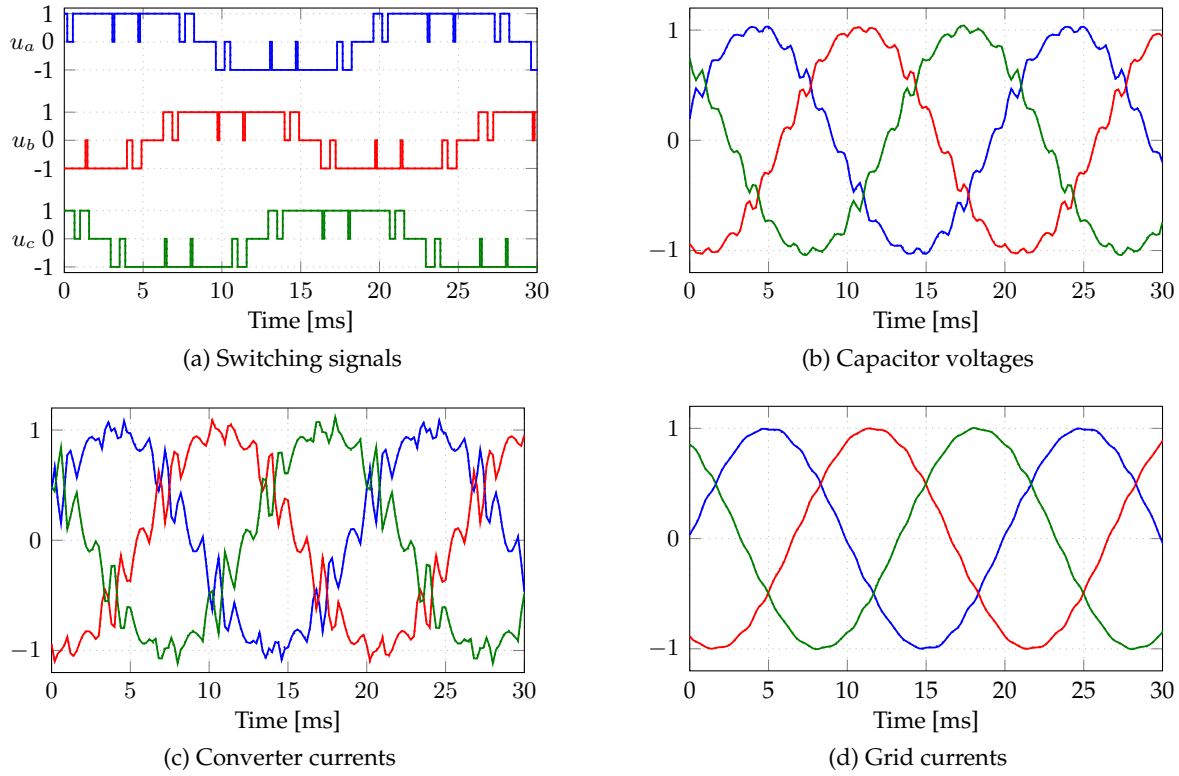

(a) Switching signals

(b) Capacitor voltages

(c) Converter currents

(d) Grid currents

Figure 4.19: System states (solid lines) and reference trajectories (dotted lines) at steady-state operation in per unit.

signals are nearly identical, as the dotted lines are concealed by the solid lines. This means that the output references are tracked accurately, and only minor modifications are applied to the switching signals. These modifications relate to the previously discussed divergent system predictions due to the averaging error. The slight difference between the references and the actual system behaviour can be seen in the zoomed in figures in Fig. 4.20 for each state variable.

For the harmonic analysis, the grid currents were recorded over 10 fundamental periods. The time-domain resolution corresponds to the controller sampling interval of $10\,\mu s$ and a rectangular window was used. The computed harmonic spectra of the grid currents are shown in Fig. 4.21a, where the harmonics of each phase are plotted on top of each other. As expected, only harmonics of integer and odd order exist. This verifies the good trajectory tracking performance of the controller. Furthermore, due to the incorporation of the LC filter impedance in the OPP computation, the harmonics around the resonance frequency of $485\,\text{Hz}$, which is slightly below the 10th order harmonic, are small.

However, slight differences in the spectra of the three phases can be noticed. Moreover, small harmonics at the 3rd and 9th order can be observed. When reducing the sampling interval to one tenth, i.e. $T_s = 20\,\mu s$, the harmonic spectra shown in Fig. 4.21b results. These spectra are effectively the same as the ideal OPP spectra, without any differences between the phases and without triple harmonics.

4.6.2 Response during Transient

The performance of the controller during reference steps is shown in Fig. 4.22. The reference of the real power is reduced at time $t = 15\,\text{ms}$ from $P^* = 1\,\text{pu}$ to $P^* = 0.5\,\text{pu}$; at $t = 35\,\text{ms}$ it is increased back to $P^* = 1\,\text{pu}$. The controller achieves relatively short settling times, which are in the order of $7\,\text{ms}$, after which the system outputs follow their references again closely.

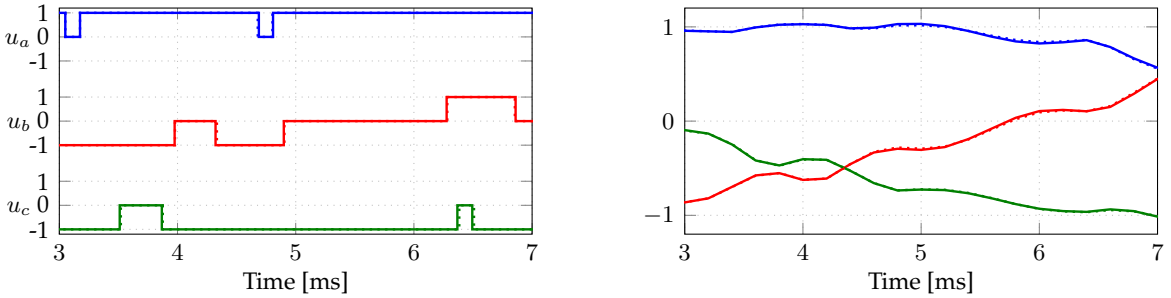

(a) Switching signals

(b) Capacitor voltages

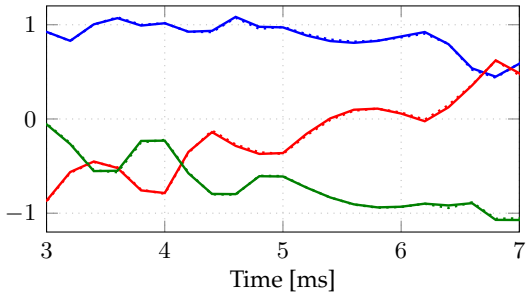

(c) Converter currents

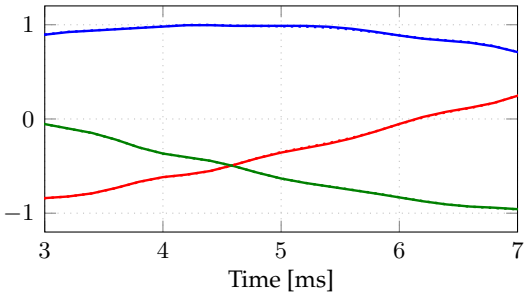

(d) Grid currents

Figure 4.20: Zoomed in system states (solid lines) and reference trajectories (dotted lines) at steady-state operation in per unit.

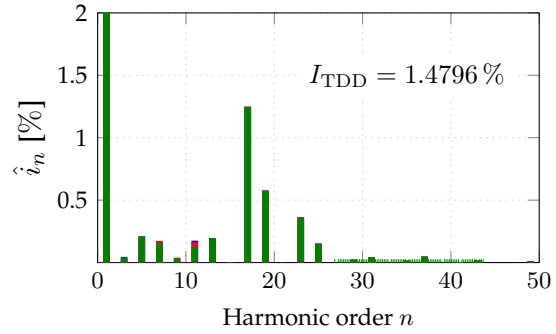

(a) $T_s = 200\,\mu\mathrm{s}$

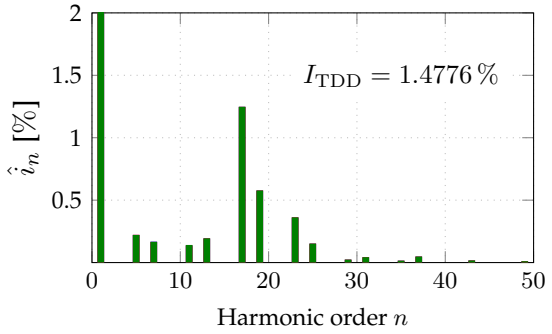

(b) $T_s = 20\,\mu\mathrm{s}$

Figure 4.21: Harmonic spectra of the grid currents for different sampling frequencies.

It can be observed that some oscillations are present in the output signals. Most likely, these are caused by the tight constraints on the switching transitions (see Section 4.4.3) and the few switching transitions available due to the low pulse number.

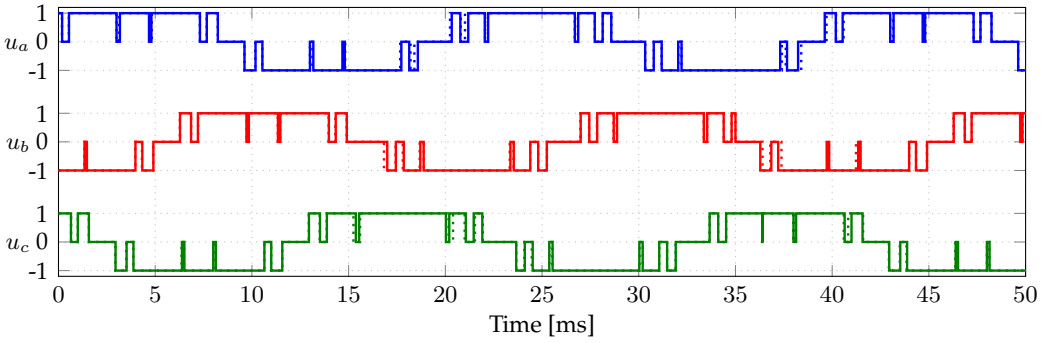

(a) Switching signals

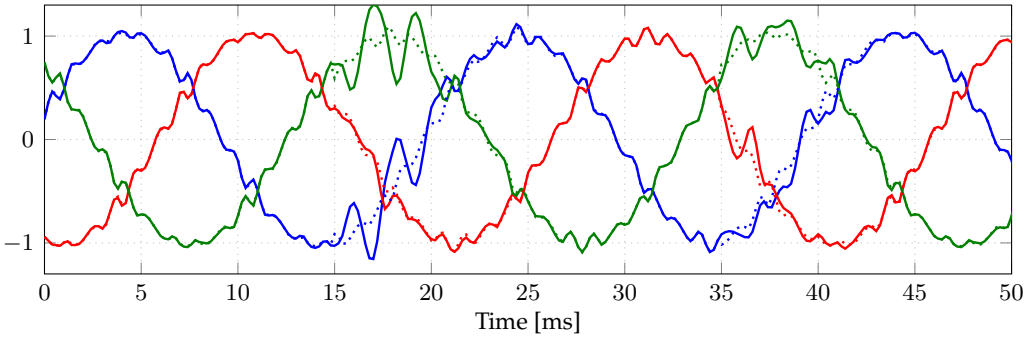

(b) Capacitor voltages

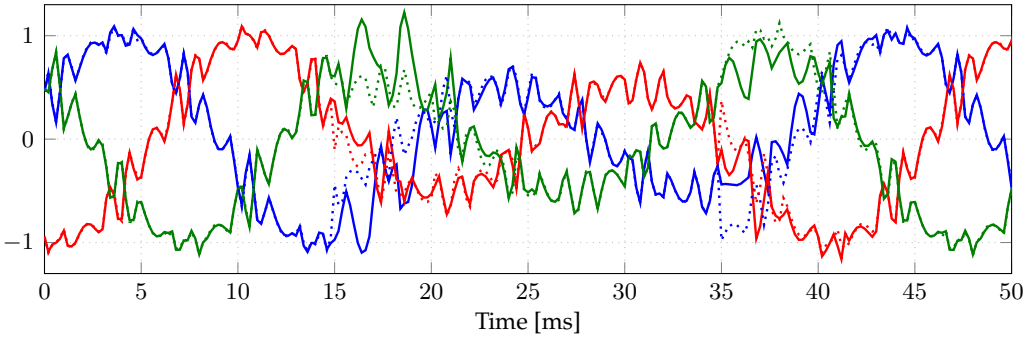

(c) Converter currents

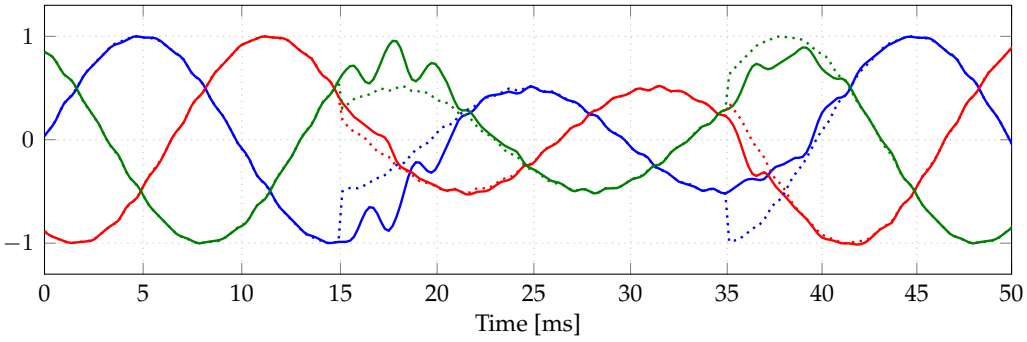

(d) Grid currents

Figure 4.22: System states (solid lines) during step changes in the real power reference. The reference trajectories (dotted lines) are obtained from the OPPs at the corresponding set points.

4.7 Summary

In this chapter, a new MPC method for higher-order systems based on OPPs was introduced and analysed. The novelty of the proposed approach is the control of all output variables of the system along their respective references. As a result, nearly optimal steady-state and fast transient responses can be achieved.

In order to predict the system behaviour with the discrete-time MIMO model, the continuous-time OPP is transformed into discrete-time averaged switch positions. By additionally transforming the necessary constraints, the optimisation is performed in the discrete-time domain. The obtained optimal solution is translated back into continuous-time switching signal modifications by a reverse transformation.

The performance of the proposed controller is mainly dependent on the choice of the sampling interval. With a small sampling interval, steady-state prediction errors are avoided and an optimal behaviour is achieved. A long sampling interval facilitates fast transient responses as the available control action is increased. The use of the receding horizon policy is beneficial as it enables the use of long sampling intervals without impairing the steady-state performance.

Chapter 5

Conclusions

5.1 Discussion of Results

Two main results were achieved in this thesis: First, OPPs with relaxed symmetry were computed, which significantly reduced the current harmonic distortions. Second, a general MP^{3}C$^+$ algorithm was proposed, which allows closed-loop control of higher-order systems with OPPs.

Reduction of Current TDD with Relaxed OPPs The relaxation of symmetry in the OPP computation revealed the restrictive nature of the commonly made symmetry assumptions. The newly computed, relaxed OPPs achieve lower harmonic distortions for the same switching frequency. This reduces the harmonic losses when operating the converter at a given switching frequency. Conversely, for the same harmonic distortions in the load, the switching frequency can be reduced. Thus, in order to fully exploit the cooling capacity of the converter, its power rating can be increased.

During the computation of the relaxed OPPs, the feature of two optimal solutions was encountered. It was identified that the two solutions are symmetrical to each other, which resulted in the same harmonic distortions. This allows adding a second objective in order to determine the best suitable solution for a particular application.

Generalised MP^{3}C$^+$ with Averaged Switch Positions With the proposed MP^{3}C$^+$ algorithm, control of the grid-connected converter system with an LC filter based on OPPs was achieved. The converter system is controlled with a single control loop, not requiring any additional control loops, such as an active damping loop.

The cornerstone of the proposed controller is the OPP transformation from continuous- to discrete-time by averaging it over the sampling intervals. In the discrete-time domain, the sequence of optimal averaged switch positions is obtained by solving a QP subject to constraints. By reverse transformation, the optimal switching time modifications of the nominal switching signal in the continuous-time domain are obtained.

MP^{3}C$^+$ is based on the state-space representation of the system. This makes MP^{3}C$^+$suitable for a variety of applications provided an accurate model exists. The bulk of the computational effort is shifted to the offline computation of the OPPs. In this OPP computation, special system dynamics, such as the resonance behaviour of the LC filter, can be already included. Online, the OPPs only have to be modified in order to reject disturbances or noise, and to allow fast transient responses.

The performance of the proposed MP^{3}C$^+$ algorithm depends on the chosen sampling frequency. However, due to the receding horizon policy, continuous feedback is provided to the

controller. This makes it robust to the averaging error, model inaccuracies and other non-idealities of the system.

5.2 Recommendations for Future Research

In this section, ideas to advance the presented research topics of this thesis are briefly described.

Efficient OPP Computation with Virtual Switching Angles The computation of OPPs is challenging due to the non-convex and mixed-integer optimisation problem that needs to be solved. With the approach of enumerating all feasible switching sequences in combination with multiple initial values, the computation of OPPs for high pulse numbers becomes intractable. Specifically tailored algorithms are required, which exploit the particular characteristics of the OPP optimisation problem. An example of such an algorithm is the previously mentioned method of *virtual angles* [27]. By combining the value of the switching angle and the sign of the corresponding switching transition into one optimisation variable, the enumeration of all feasible switching sequences is avoided. A similar approach has been also presented in [23] for the half-wave symmetric SHE problem. Adopting this scheme to the half-wave symmetric and full-wave symmetric OPP problems would greatly reduce the computational effort and would allow the computation of OPPs at higher pulse numbers.

Low-dimensional QP The optimisation variable $\boldsymbol{W}_{abc}(k)$ of the QP (4.59) underlying the proposed MP^{3}C$^+$ method is of the dimension $3N$, owing to the three phases and the prediction horizon N. The time required to solve the QP strongly depends on the dimension of $\boldsymbol{W}_{abc}(k)$. To speed up the computations, the problem dimension can be easily reduced. Recall that the controller is allowed to modify the averaged switch positions only in sampling intervals in which at least one switching transition occurs. Conversely, the averaged switch positions cannot be manipulated in sampling intervals without a switching transition; the averaged switch positions are thus fixed, and can be removed as a degree of freedom. This means that the dimension of the optimisation vector can be reduced accordingly. However, the Hessian matrix then becomes a time-varying matrix.

Constraints on Averaged Switch Positions So far, the switching instants cannot be moved beyond their respective sampling interval, see (4.49). This implies that the lower and upper constraints on the averaged switch positions are determined by the minimum and maximum switch position that can be synthesised in the sampling interval; the constraints are thus relatively tight. Because of that a relatively long sampling interval was chosen in the simulations to provide the controller with a sufficient degree of freedom to manipulate the switching instants.

To relax the somewhat artificial restriction imposed by the sampling interval, the bounds can be relaxed by a given $\Delta w_{p,\max}$. This implies that the switching instants are allowed to be moved beyond their corresponding sampling intervals by a fixed maximum amount.

Alternatively, the sampling interval restrictions can be fully removed. Consider the switching signal in phase p, with $p \in \{a, b, c\}$, and n_p switching transitions within the prediction horizon. The constraint (4.49) can then be generalised to the whole prediction horizon interval, i.e.

$$kT_s \leq t_{p1} \leq t_{p2} \leq \ldots \leq t_{pn_p} \leq (k+N)T_s. \tag{5.1}$$

The lower constraint at kT_s ensures that switching instants are not moved into the past. The upper constraint at $(k+N)T_s$ limits the last switching instant t_{pn_p} to the prediction horizon interval. The constraints in (5.1) can be translated into equivalent constraints on the averaged switch positions in the discrete-time domain $w_p(\ell)$ with $\ell \in \{k, k+1, \ldots, k+N\}$.

Moving the switching transitions beyond their nominal sampling intervals, however, requires a further adaptation of the problem formulation. Recall that due to the switching signal transformation the averaged switch position depends only on the switching transitions occurring in that sampling interval. However, when the nominal and the modified switching transition occur in different sampling intervals, a new sequence of averaged switch positions arises. This implies that the optimisation problem needs to be solved again.

Constraints on Output Variables One of the main benefits of MPC is its ability to impose constraints on state, input and output variables. So far, we have only imposed constraints on the manipulated variables, i.e. on the averaged switch positions. Constraints on the output variables might be beneficial to limit overshoots during transients and faults. By limiting the converter current and capacitor voltage to their safe operating area with the help of output constraints, damage to the converter and its passive components can be avoided.

To do so, recall (E.3). Based on the current state vector $\boldsymbol{x}_{\alpha\beta}(k)$ and the sequence of future manipulated variables $\boldsymbol{W}_{abc}(k)$, this equation predicts the future output variables $\boldsymbol{Y}_{\alpha\beta}(k)$ as defined in (E.2). It is straightforward to impose upper and lower constraints on these output variables. To ensure that a solution to the quadratic program always exists, i.e. that a sequence of manipulated variables $\boldsymbol{W}_{abc}(k)$ can be computed for the given state vector and OPP in all circumstances, it is advisable to impose the constraints on the output variables as soft constraints. These introduce slack variables in the inequality constraints, which are heavily penalised in an additional term in the objective function. In doing so, (slight) violations of the output constraints are possible, albeit at the expense of a huge penalty in the objective function.

Controller Tests The presented simulation results of the controller performance were computed for ideal conditions. More tests to analyse the control performance under real operating conditions would be interesting. To that end, a ripple of the dc-link voltage or grid harmonics might be simulated. Furthermore, model inaccuracies such as parameter mismatches or measurement noise might be assumed. It is expected that the proposed MP^{3}C$^+$ will still achieve nearly optimal steady-state outputs. The continuous feedback together with the receding horizon policy allow the controller to adjust the control actions at each sampling instant to reject disturbances and to reduce the impact of modelling errors.

Implementation Finally, the MP^{3}C$^+$ algorithm should be implemented on an embedded system, such as a field-programmable gate array (FPGA) to perform practical tests. The implementation of OPPs with look-up tables on such devices is well-known [48]. QP solvers running on FPGAs has been also successfully demonstrated [49]. The transformation of the switching signal entails only simple summations and multiplications. For the reverse transformation of the switching signal modifications, a solver for a linear program needs to be implemented.

Appendices

A Harmonic Analysis of Pulse Patterns with Relaxed Symmetry

In this appendix, two sets of Fourier coefficients are derived for three-level pulse patterns with relaxed symmetry: First, pulse patterns with full-wave symmetry are considered and second, half-wave symmetry is also imposed.

Full-wave Symmetry Recall that the pulse pattern $u(\theta)$ is a piecewise constant function with $4d+1$ intervals of constant value, i.e. the switch positions. Thus, we can write the Fourier coefficients in (2.12) as $4d+1$ individual integral terms with the switching angles as limits and the switch positions as constant factors

$$a_n = \frac{1}{\pi}\left[u_0\int_0^{\alpha_1}\cos(n\theta)\,\mathrm{d}\theta + u_1\int_{\alpha_1}^{\alpha_2}\cos(n\theta)\,\mathrm{d}\theta + \cdots + u_{4d}\int_{\alpha_{4d}}^{2\pi}\cos(n\theta)\,\mathrm{d}\theta\right]. \tag{A.1}$$

With (2.9) we write the switch positions as the sum of switching transitions and rearrange the terms in (A.1) as follows

$$\begin{aligned} a_n &= \frac{1}{\pi}\left[u_0\int_0^{\alpha_1}\cos(n\theta)\,\mathrm{d}\theta + (u_0+\Delta u_1)\int_{\alpha_1}^{\alpha_2}\cos(n\theta)\,\mathrm{d}\theta + \cdots + \left(u_0+\sum_{j=1}^{4d}\Delta u_j\right)\int_{\alpha_{4d}}^{2\pi}\cos(n\theta)\,\mathrm{d}\theta\right] \\ &= \frac{1}{\pi}\left[u_0\int_0^{2\pi}\cos(n\theta)\,\mathrm{d}\theta + \Delta u_1\int_{\alpha_1}^{2\pi}\cos(n\theta)\,\mathrm{d}\theta + \cdots + \Delta u_{4d}\int_{\alpha_{4d}}^{2\pi}\cos(n\theta)\,\mathrm{d}\theta\right] \\ &= \frac{1}{\pi}\left[u_0\int_0^{2\pi}\cos(n\theta)\,\mathrm{d}\theta + \sum_{i=1}^{4d}\Delta u_i\int_{\alpha_i}^{2\pi}\cos(n\theta)\,\mathrm{d}\theta\right]. \end{aligned} \tag{A.2}$$

For $n=0$, the cosine functions in (A.2) are one, and the integrals simplify to

$$a_0 = \frac{1}{\pi}\left[2\pi u_0 + 2\pi\sum_{i=1}^{4d}\Delta u_i - \sum_{i=1}^{4d}\Delta u_i\alpha_i\right]. \tag{A.3}$$

Note that, due to periodicity, the sum of all $4d$ switching transitions is zero, $\sum_{i=1}^{4d}\Delta u_i = 0$. Thus, (A.3) simplifies to

$$a_0 = 2u_0 - \frac{1}{\pi}\sum_{i=1}^{4d}\Delta u_i\alpha_i. \tag{A.4}$$

For $n \geq 1$, the first term in (A.2) is zero, as it is the integral over n fundamental periods of the cosine function. The remaining integrals are solved to

$$a_n = \frac{1}{\pi n}\sum_{i=1}^{4d}\Delta u_i\Big[\sin(n2\pi) - \sin(n\alpha_i)\Big]. \tag{A.5}$$

Thus, we find the following expression for the Fourier coefficients a_n

$$a_n = -\frac{1}{\pi n}\sum_{i=1}^{4d}\Delta u_i\sin(n\alpha_i), \qquad n = 1,2,3,\ldots \tag{A.6}$$

A similar derivation is performed for the Fourier coefficients b_n, leading to the analogous expression

$$b_n = \frac{1}{\pi n}\sum_{i=1}^{4d}\Delta u_i\cos(n\alpha_i), \qquad n = 1,2,3,\ldots \tag{A.7}$$

Half-wave Symmetry By imposing half-wave symmetry, the expressions for the Fourier coefficients can be simplified. The integral in (2.12a) is divided into two terms, each over one half-wave of the fundamental period,

$$a_n = \frac{1}{\pi}\int_0^{\pi} u(\theta)\cos(n\theta)\,\mathrm{d}\theta + \frac{1}{\pi}\int_{\pi}^{2\pi} u(\theta)\cos(n\theta)\,\mathrm{d}\theta. \tag{A.8}$$

Substituting the variable θ in the second term with $\theta = \pi + \theta'$ leads to

$$\begin{aligned} a_n &= \frac{1}{\pi}\int_0^{\pi} u(\theta)\cos(n\theta)\,\mathrm{d}\theta + \frac{1}{\pi}\int_0^{\pi} u(\pi+\theta')\cos(n\pi + n\theta')\,\mathrm{d}\theta' \\ &= \frac{1}{\pi}\int_0^{\pi} u(\theta)\cos(n\theta)\,\mathrm{d}\theta - \frac{1}{\pi}\int_0^{\pi} u(\theta')\cos(n\pi + n\theta')\,\mathrm{d}\theta', \end{aligned} \tag{A.9}$$

where we incorporated the half-wave symmetry condition (2.6) in the second integral to get (A.9). With the help of the trigonometric identity

$$\cos(n\pi + n\theta') = (-1)^n\cos(n\theta'), \tag{A.10}$$

and by removing the index $'$, the two integral terms in (A.9) can be combined, which gives

$$\begin{aligned} a_n &= \frac{1}{\pi}\int_0^{\pi} u(\theta)\Big[\cos(n\theta) - (-1)^n\cos(n\theta)\Big]\,\mathrm{d}\theta \\ &= \Big[1 - (-1)^n\Big]\frac{1}{\pi}\int_0^{\pi} u(\theta)\cos(n\theta)\,\mathrm{d}\theta. \end{aligned} \tag{A.11}$$

As a result, the Fourier coefficients are non-zero only for odd numbered harmonic orders

$$a_n = \begin{cases} 0, & n = 0, 2, 4, \ldots \\ \dfrac{2}{\pi}\displaystyle\int_0^{\pi} u(\theta)\cos(n\theta)\,\mathrm{d}\theta, & n = 1, 3, 5, \ldots \end{cases} \tag{A.12}$$

For the Fourier coefficients b_n, similar steps are applied to the integral terms in (2.12b), which result in

$$b_n = \begin{cases} 0, & n = 0, 2, 4, \ldots \\ \dfrac{2}{\pi}\displaystyle\int_0^{\pi} u(\theta)\sin(n\theta)\,\mathrm{d}\theta, & n = 1, 3, 5, \ldots \end{cases} \tag{A.13}$$

Next, the procedure of deriving the Fourier coefficients for the full-wave symmetric pulse patterns is repeated for the integrals in (A.12) and (A.13). According to the definition of the half-wave symmetric pulse patterns, the integrals are divided into multiple intervals of constant switch position and are again rearranged, which gives for the odd numbered harmonic orders

$$\begin{aligned} a_n &= \frac{2}{\pi}\left[u_0\int_0^{\pi}\cos(n\theta)\,\mathrm{d}\theta + \sum_{i=1}^{2d}\Delta u_i\int_{\alpha_i}^{\pi}\cos(n\theta)\,\mathrm{d}\theta\right] \\ &= -\frac{2}{\pi n}\sum_{i=1}^{2d}\Delta u_i\sin(n\alpha_i), \qquad n = 1, 3, 5, \ldots \end{aligned} \tag{A.14}$$

Note that the first term in (A.14) integrates the cosine function over half of the fundamental period, which yields zero. For the Fourier coefficients b_n the same procedure of dividing and rearranging the integral terms is applied, which leads for odd harmonic orders to

$$b_n = \frac{2}{\pi}\left[u_0 \int_0^{\pi} \sin(n\theta)\,\mathrm{d}\theta + \sum_{i=1}^{2d} \Delta u_i \int_{\alpha_i}^{\pi} \sin(n\theta)\,\mathrm{d}\theta\right]$$

$$= \frac{2}{\pi}\left[2u_0 + \sum_{i=1}^{2d} \Delta u_i + \sum_{i=1}^{2d} \Delta u_i \cos(n\alpha_i)\right], \qquad n = 1, 3, 5, \ldots \tag{A.15}$$

Recall (2.9) and the restriction to the initial switch position imposed by half-wave symmetry

$$u_0 + \sum_{i=1}^{2d} \Delta u_i = u_{2d} = -u_0. \tag{A.16}$$

As a result, the first two terms in (A.15) sum up to zero, and the remaining term corresponds to the expression of Fourier coefficients for half-wave symmetric pulse patterns given in (3.3) in Table 3.2.

B Harmonic Analysis of Symmetrical Solutions

Consider the two half-wave symmetric OPPs in Section 3.5.2 with the symmetry as in (3.20). In this Appendix, we derive two pairs of Fourier coefficients to prove that their corresponding values of the objective function are identical. Note that we refer to the two pulse patterns with $u_A(\theta)$ for the first solution and with $u_B(\theta)$ for the second solution. Recall the Fourier coefficient (A.12) for half-wave symmetric OPPs. For the two solutions we define the Fourier coefficients

$$a_{An} = \frac{2}{\pi}\int_0^{\pi} u_A(\theta)\cos(n\theta)\,\mathrm{d}\theta \tag{B.1}$$

$$a_{Bn} = \frac{2}{\pi}\int_0^{\pi} u_B(\theta)\cos(n\theta)\,\mathrm{d}\theta, \qquad n = 1, 3, 5, \ldots \tag{B.2}$$

Note that due to half-wave symmetry the Fourier coefficients are zero for even harmonics, therefore only odd harmonics are considered. Next we insert (3.20) in (B.2) to obtain

$$a_{Bn} = \frac{2}{\pi}\int_0^{\pi} u_A(\pi - \theta)\cos(n\theta)\,\mathrm{d}\theta \tag{B.3}$$

and substitute the variable θ with $\theta = \pi - \overline{\theta}$

$$a_{Bn} = -\frac{2}{\pi}\int_{\pi}^{0} u_A(\overline{\theta})\cos(n\pi - n\overline{\theta})\,\mathrm{d}\overline{\theta}$$

$$= -\frac{2}{\pi}\int_0^{\pi} u_A(\overline{\theta})\cos(n\overline{\theta})\,\mathrm{d}\overline{\theta}. \tag{B.4}$$

Note that in the second term we have used the cosine identity $\cos(n\pi - n\overline{\theta}) = (-1)^n\cos(n\overline{\theta})$ and exploited the fact that the Fourier coefficient exists only for odd harmonics. Inspection of (B.4) and (B.1) shows that for the two Fourier coefficients the statement holds

$$a_{An} = -a_{Bn}. \tag{B.5}$$

A similar derivation can be performed for the Fourier coefficients b_{An} and b_{Bn} starting with (A.13), which follows the exact same steps but employs the sine identity $\sin(n\pi - n\theta) = -(-1)^n\sin(n\theta)$ instead. In the end, the statement

$$b_{An} = b_{Bn} \tag{B.6}$$

results for the two Fourier coefficients.

C State-space Model of the Grid-connected Converter System

For the derivation of the state-space model of the grid-connected converter system, assume ideal sinusoidal grid voltages

$$\boldsymbol{v}_{g,\alpha\beta}(t) = \hat{v}_g \begin{bmatrix} \sin(\omega_g t - \phi_g) \\ -\cos(\omega_g t - \phi_g) \end{bmatrix}, \tag{C.1}$$

where $\hat{v}_g$ is the amplitude of the grid voltage and ϕ_g is the phase angle. With this, the dynamics of the grid voltage can be directly described by

$$\frac{\mathrm{d}\boldsymbol{v}_{g,\alpha\beta}(t)}{\mathrm{d}t} = \hat{v}_g \omega_g \begin{bmatrix} \cos(\omega_g t - \phi_g) \\ \sin(\omega_g t - \phi_g) \end{bmatrix} = \begin{bmatrix} 0 & -\omega_g \\ \omega_g & 0 \end{bmatrix} \boldsymbol{v}_{g,\alpha\beta}(t). \tag{C.2}$$

By substituting (C.2) in the derived equation system (4.10), and using the state and output vectors defined in (4.13) and (4.14), respectively, the matrices for the state-space model (4.15) are derived as

$$\boldsymbol{F} = \begin{bmatrix} -\frac{R_1+R_2}{L_1}\boldsymbol{I}_2 & -\frac{1}{L_1}\boldsymbol{I}_2 & \frac{R_2}{L_1}\boldsymbol{I}_2 & \boldsymbol{0}_2 \\ \frac{1}{C_2}\boldsymbol{I}_2 & \boldsymbol{0}_2 & -\frac{1}{C_2}\boldsymbol{I}_2 & \boldsymbol{0}_2 \\ \frac{R_2}{L_3}\boldsymbol{I}_2 & \frac{1}{L_3}\boldsymbol{I}_2 & -\frac{R_2+R_3}{L_3}\boldsymbol{I}_2 & -\frac{1}{L_3}\boldsymbol{I}_2 \\ \boldsymbol{0}_2 & \boldsymbol{0}_2 & \boldsymbol{0}_2 & \begin{bmatrix} 0 & -\omega_g \\ \omega_g & 0 \end{bmatrix} \end{bmatrix}, \tag{C.3}$$

$$\boldsymbol{G} = \begin{bmatrix} \frac{V_{\mathrm{dc}}}{2L_1}\boldsymbol{I}_2 & \boldsymbol{0}_{2\times 6} \end{bmatrix}^T \boldsymbol{K}, \tag{C.4}$$

$$\boldsymbol{C} = \begin{bmatrix} \boldsymbol{I}_6 & \boldsymbol{0}_{6\times 2} \end{bmatrix}. \tag{C.5}$$

Note that $\boldsymbol{I}_2$ is the identity, and $\boldsymbol{0}_2$ is the zero matrix. Both matrices are of the size 2×2.

D Reduced State-space Model for Reference Computation

For the reference computation, the state-space model is derived for the reduced state vector $\tilde{\boldsymbol{x}}_{\alpha\beta}(t) \in \mathbb{R}^{n_y}$. In this, the grid voltage is considered not a state but an input variable. Thus, the matrix $\tilde{\boldsymbol{F}}$ is readily obtained from the previously derived matrix $\boldsymbol{F}$ in (C.3) by removing the last two dimensions

$$\tilde{\boldsymbol{F}} = \begin{bmatrix} -\frac{R_1+R_2}{L_1}\boldsymbol{I}_2 & -\frac{1}{L_1}\boldsymbol{I}_2 & \frac{R_2}{L_1}\boldsymbol{I}_2 \\ \frac{1}{C_2}\boldsymbol{I}_2 & \boldsymbol{0}_2 & -\frac{1}{C_2}\boldsymbol{I}_2 \\ \frac{R_2}{L_3}\boldsymbol{I}_2 & \frac{1}{L_3}\boldsymbol{I}_2 & -\frac{R_2+R_3}{L_3}\boldsymbol{I}_2 \end{bmatrix}. \tag{D.1}$$

The input matrices for the converter and grid voltage are derived from $\boldsymbol{G}$ in (C.4) and the last column of $\boldsymbol{F}$ accordingly

$$\boldsymbol{G}_1 = \begin{bmatrix} \frac{V_{\text{dc}}}{2L_1}\boldsymbol{I}_2 & \boldsymbol{0}_{2\times 4} \end{bmatrix}^T \boldsymbol{K}_{\alpha\beta} \tag{D.2}$$

$$\boldsymbol{G}_2 = \begin{bmatrix} \boldsymbol{0}_{2\times 4} & -\frac{1}{L_3}\boldsymbol{I}_2 \end{bmatrix}^T. \tag{D.3}$$

E Derivation of Quadratic Program

From the cost function (4.55), the discrete-time system model (4.52) and the constraints (4.57), the MP^{3}C$^+$ optimisation problem follows as

$$\begin{aligned} \boldsymbol{W}_{abc}(k) = &\underset{\boldsymbol{W}_{abc}(k)}{\text{arg minimise}} \quad \sum_{\ell=k}^{k+N-1} \left\|\boldsymbol{y}^*_{\alpha\beta}(\ell+1) - \boldsymbol{y}_{\alpha\beta}(\ell+1)\right\|^2_{\boldsymbol{Q}} + \lambda_w \|\boldsymbol{w}^*_{abc}(\ell) - \boldsymbol{w}_{abc}(\ell)\|_2^2 \\ &\text{subject to} \quad \begin{aligned} &\boldsymbol{x}_{\alpha\beta}(\ell+1) = \boldsymbol{A}\,\boldsymbol{x}_{\alpha\beta}(\ell) + \boldsymbol{B}\,\boldsymbol{w}_{abc}(\ell) \\ &\boldsymbol{y}_{\alpha\beta}(\ell+1) = \boldsymbol{C}\,\boldsymbol{x}_{\alpha\beta}(\ell+1) \qquad \forall \ell = k, \ldots, k+N-1 \\ &\boldsymbol{G}\,\boldsymbol{W}_{abc}(k) \leq \boldsymbol{g}. \end{aligned} \end{aligned} \tag{E.1}$$

To solve (E.1), a more convenient form of the quadratic program (QP) is required. A detailed derivation of a similar QP can be found in [8, Ch. 5 Appendix B].

We define the sequence of predicted output variables over the prediction horizon computed at the current sampling instant kT_s as

$$\boldsymbol{Y}_{\alpha\beta}(k) = \begin{bmatrix} \boldsymbol{y}^T_{\alpha\beta}(k+1) & \boldsymbol{y}^T_{\alpha\beta}(k+2) & \ldots & \boldsymbol{y}^T_{\alpha\beta}(k+N) \end{bmatrix}^T. \tag{E.2}$$

It is derived as a function of the current state vector $\boldsymbol{x}_{\alpha\beta}(k)$ and the sequence of averaged switch positions $\boldsymbol{W}_{abc}(k)$ by recursively inserting (4.52)

$$\boldsymbol{Y}_{\alpha\beta}(k) = \underbrace{\begin{bmatrix} \boldsymbol{CA} \\ \boldsymbol{CA}^2 \\ \vdots \\ \boldsymbol{CA}^N \end{bmatrix}}_{\boldsymbol{\Gamma}} \boldsymbol{x}_{\alpha\beta}(k) + \underbrace{\begin{bmatrix} \boldsymbol{CB} & \boldsymbol{0}_{6\times 3} & \ldots & \boldsymbol{0}_{6\times 3} \\ \boldsymbol{CAB} & \boldsymbol{CB} & \ldots & \boldsymbol{0}_{6\times 3} \\ \vdots & \vdots & \ddots & \vdots \\ \boldsymbol{CA}^{N-1}\boldsymbol{B} & \boldsymbol{CA}^{N-2}\boldsymbol{B} & \ldots & \boldsymbol{CB} \end{bmatrix}}_{\boldsymbol{\Upsilon}} \boldsymbol{W}_{abc}(k), \tag{E.3}$$

where $\boldsymbol{\Gamma} \in \mathbb{R}^{6N\times 8}$ and $\boldsymbol{\Upsilon} \in \mathbb{R}^{6N\times 3N}$. We define the matrix

$$\widetilde{\boldsymbol{Q}} = \text{diag}(\boldsymbol{Q}, \boldsymbol{Q}, \ldots, \boldsymbol{Q}),$$

where $\widetilde{\boldsymbol{Q}} \in \mathbb{R}^{6N\times 6N}$. With this definition and with (E.3), we rewrite the cost function as

$$\begin{aligned} J = &\Big(\boldsymbol{Y}^*_{\alpha\beta}(k) - \boldsymbol{\Gamma}\boldsymbol{x}_{\alpha\beta}(k) - \boldsymbol{\Upsilon}\,\boldsymbol{W}_{abc}(k)\Big)^T \widetilde{\boldsymbol{Q}} \Big(\boldsymbol{Y}^*_{\alpha\beta}(k) - \boldsymbol{\Gamma}\boldsymbol{x}_{\alpha\beta}(k) - \boldsymbol{\Upsilon}\,\boldsymbol{W}_{abc}(k)\Big) \\ &+ \lambda_w \Big(\boldsymbol{W}^*_{abc}(k) - \boldsymbol{W}_{abc}(k)\Big)^T \Big(\boldsymbol{W}^*_{abc}(k) - \boldsymbol{W}_{abc}(k)\Big). \end{aligned} \tag{E.4}$$

After some algebraic manipulations we derive the cost function

$$J = \frac{1}{2}\boldsymbol{W}^T_{abc}(k)\,\boldsymbol{H}\,\boldsymbol{W}_{abc}(k) + \boldsymbol{\Theta}^T(k)\,\boldsymbol{W}_{abc}(k) + \theta(k), \tag{E.5}$$

with

$$\boldsymbol{H} = 2\left[\boldsymbol{\Upsilon}^T\widetilde{\boldsymbol{Q}}\,\boldsymbol{\Upsilon} + \lambda_w \boldsymbol{I}_{3N}\right] \tag{E.6}$$

$$\boldsymbol{\Theta}(k) = 2\left[\boldsymbol{\Upsilon}^T\widetilde{\boldsymbol{Q}}\left(\boldsymbol{\Gamma}\boldsymbol{x}_{\alpha\beta}(k) - \boldsymbol{Y}^*_{\alpha\beta}(k)\right) - \lambda_w\, \boldsymbol{W}^*_{abc}(k)\right] \tag{E.7}$$

$$\theta(k) = \left\|\boldsymbol{Y}^*_{\alpha\beta}(k) - \boldsymbol{\Gamma}\boldsymbol{x}_{\alpha\beta}(k)\right\|^2_{\widetilde{\boldsymbol{Q}}} + \lambda_w\|\boldsymbol{W}^*_{abc}(k)\|_2^2. \tag{E.8}$$

Note that the term $\theta(k)$ remains constant during the optimisation and can thus be neglected in the cost function. This leads to the cost function for the MP^{3}C$^+$ problem as stated in (4.59).

F Deriving Averaged Switch Position Modification

Consider the single-phase averaged switch position modification in the kth sampling interval

$$\Delta w_p(k) = w_p(k) - w^*_p(k), \tag{F.1}$$

where $w_p(k)$ is the modified averaged switch position in the kth sampling interval. Recall that n_{pk} denotes the number of nominal switching transitions in the kth sampling interval, and that the limits of the sampling interval are renamed according to (4.43). In (F.1) we substitute $w^*_p(k)$ with (4.46); $w_p(k)$ can be replaced by an equivalent equation without the superscript *. This results in

$$\Delta w_p(k) = \sum_{i=0}^{n_{pk}} \frac{t_{p,i+1} - t_{pi}}{T_s} u_{pi} - \sum_{i=0}^{n_{pk}} \frac{t^*_{p,i+1} - t^*_{pi}}{T_s} u^*_{pi}. \tag{F.2}$$

Because the switch positions are not modified, we have $u_{pi} = u^*_{pi}$, leading to

$$\Delta w_p(k) = \sum_{i=0}^{n_{pk}} \frac{t_{p,i+1} - t^*_{p,i+1}}{T_s} u_{pi} - \sum_{i=0}^{n_{pk}} \frac{t_{pi} - t^*_{pi}}{T_s} u_{pi}. \tag{F.3}$$

Note that according to (4.43) the first and last switching instants for the modified and nominal switching signals are equal, as they correspond to the sampling interval limits

$$t_{p0} = t^*_{p0} = kT_s \qquad \text{and} \qquad t_{p,n_{pk}+1} = t^*_{p,n_{pk}+1} = (k+1)T_s. \tag{F.4}$$

Furthermore, we define the ith switching instant modification in phase p

$$\Delta t_{pi} = t_{pi} - t^*_{pi} \tag{F.5}$$

as the difference between the modified switching instant t_{pi} and the nominal switching instant t^*_{pi}. With (F.4) and (F.5), the sums in (F.2) reduce to

$$\begin{aligned}
\Delta w_p(k) &= \sum_{i=0}^{n_{pk}-1} \frac{\Delta t_{p,i+1}}{T_s} u_{pi} - \sum_{i=1}^{n_{pk}} \frac{\Delta t_{pi}}{T_s} u_{pi} \\
&= \sum_{i=1}^{n_{pk}} \frac{\Delta t_{pi}}{T_s} u_{p,i-1} - \sum_{i=1}^{n_{pk}} \frac{\Delta t_{pi}}{T_s} u_{pi} \\
&= \sum_{i=1}^{n_{pk}} \frac{\Delta t_{pi}}{T_s} \left(u_{p,i-1} - u_{pi}\right).
\end{aligned} \tag{F.6}$$

With the definition of the switching transition Δu_{pi} in (2.8), (F.6) simplifies to

$$\Delta w_p(k) = -\sum_{i=1}^{n_{pk}} \frac{\Delta t_{pi}}{T_s} \Delta u_{pi}. \tag{F.7}$$

Bibliography

[1] J. Rodríguez, S. Bernet, P. K. Steimer, and I. E. Lizama. A survey on neutral-point-clamped inverters. *IEEE Transactions on Industrial Electronics*, 57(7):2219–2230, July 2010.

[2] K. Hasse. Zum dynamischen verhalten der asynchronmaschine bei betrieb mit variabler standerfrequenz und standerspannung. *ETZ-A Bd.*, 89:77, 1968.

[3] F. Blaschke. Das prinzip der feldorientierung, die grundlage fur die transvector-regelung von drehfeldmaschinen. *Siemens-Zeitschrift*, 45:757–767, 1971.

[4] D. G. Holmes and T. A. Lipo. *Pulse Width Modulation for Power Converters: Principles and Practice*. John Wiley & Sons, Ltd, 2003.

[5] A. K. Rathore, J. Holtz, and T. Boller. Synchronous optimal pulsewidth modulation for low-switching-frequency control of medium-voltage multilevel inverters. *IEEE Transactions on Industrial Electronics*, 57(7):2374–2381, July 2010.

[6] A. Edpuganti and A. K. Rathore. A survey of low switching frequency modulation techniques for medium-voltage multilevel converters. *IEEE Transactions on Industry Applications*, 51(5):4212–4228, September 2015.

[7] J. Holtz. Pulsewidth modulation-a survey. *IEEE Transactions on Industrial Electronics*, 39(5):410–420, October 1992.

[8] T. Geyer. *Model Predictive Control of High Power Converters and Industrial Drives*. John Wiley & Sons, Ltd, 2016.

[9] F. G. Turnbull. Selected harmonic reduction in static D-C – A-C inverters. *IEEE Transactions on Communication and Electronics*, 83(73):374–378, July 1964.

[10] H. S. Patel and R. G. Hoft. Generalized techniques of harmonic elimination and voltage control in thyristor inverters: Part I–harmonic elimination. *IEEE Transactions on Industry Applications*, IA-9(3):310–317, May 1973.

[11] H. S. Patel and R. G. Hoft. Generalized techniques of harmonic elimination and voltage control in thyristor inverters: Part II–voltage control techniques. *IEEE Transactions on Industry Applications*, IA-10(5):666–673, September 1974.

[12] J. N. Chiasson, L. M. Tolbert, K. J. McKenzie, and Z. Du. A complete solution to the harmonic elimination problem. *IEEE Transactions on Power Electronics*, 19(2):491–499, March 2004.

[13] V. G. Agelidis, A. I. Balouktsis, and C. Cossar. On attaining the multiple solutions of selective harmonic elimination PWM three-level waveforms through function minimization. *IEEE Transactions on Industrial Electronics*, 55(3):996–1004, March 2008.

[14] J. N. Chiasson, L. M. Tolbert, K. J. McKenzie, and Z. Du. A unified approach to solving the harmonic elimination equations in multilevel converters. *IEEE Transactions on Power Electronics*, 19(2):478–490, March 2004.

[15] G. S. Buja and G. B. Indri. Optimal pulsewidth modulation for feeding AC motors. *IEEE Transactions on Industry Applications*, IA-13(1):38–44, January 1977.

[16] G. S. Buja. Optimum output waveforms in PWM inverters. *IEEE Transactions on Industry Applications*, IA-16(6):830–836, November 1980.

[17] A. K. Rathore, J. Holtz, and T. Boller. Generalized optimal pulsewidth modulation of multilevel inverters for low-switching-frequency control of medium-voltage high-power industrial AC drives. *IEEE Transactions on Industrial Electronics*, 60(10):4215–4224, October 2013.

[18] S. Boyd and L. Vandenberghe. *Convex Optimization*. Cambridge University Press, 2004.

[19] P. N. Enjeti, P. D. Ziogas, and J. F. Lindsay. Programmed PWM techniques to eliminate harmonics: a critical evaluation. *IEEE Transactions on Industry Applications*, 26(2):302–316, March 1990.

[20] J. R. Wells, B. M. Nee, P. L. Chapman, and P. T. Krein. Selective harmonic control: a general problem formulation and selected solutions. *IEEE Transactions on Power Electronics*, 20(6):1337–1345, November 2005.

[21] M. S. A. Dahidah, G. Konstantinou, N. Flourentzou, and V. G. Agelidis. On comparing the symmetrical and non-symmetrical selective harmonic elimination pulse-width modulation technique for two-level three-phase voltage source converters. *IET Power Electronics*, 3(6):829–842, November 2010.

[22] M. S. A. Dahidah, V. G. Agelidis, and M. V. Rao. On abolishing symmetry requirements in the formulation of a five-level selective harmonic elimination pulse-width modulation technique. *IEEE Transactions on Power Electronics*, 21(6):1833–1837, November 2006.

[23] A. Pérez-Basante, S. Ceballos, G. Konstantinou, J. Pou, I. Kortabarria, and I. M. de Alegría. A universal formulation for multilevel selective-harmonic-eliminated PWM with half-wave symmetry. *IEEE Transactions on Power Electronics*, 34(1):943–957, January 2019.

[24] A. Tripathi and G. Narayanan. Optimal pulse width modulation of voltage-source inverter fed motor drives with relaxation of quarter wave symmetry condition. In *IEEE International Conference on Electronics, Computing and Communication Technologies (CONECCT)*, January 2014.

[25] A. Tripathi and G. Narayanan. High-performance off-line pulse width modulation without quarter wave symmetry for voltage-source inverter. In *Proc. Int. Conf. Advances in Electronics Computers and Communications*, October 2014.

[26] A. D. Birda, J. Reuss, and C. Hackl. Synchronous optimal pulse-width modulation with differently modulated waveform symmetry properties for feeding synchronous motor with high magnetic anisotropy. In *European Conference on Power Electronics and Applications (EPE)*, September 2017.

[27] J. Lago and M. L. Heldwein. Generalized synchronous optimal pulse width modulation for multilevel inverters. *IEEE Transactions on Power Electronics*, 32(8):6297–6307, August 2017.

[28] J. H. Halton. Algorithm 247: Radical-inverse quasi-random point sequence. *Communications of the ACM*, 7(12):701–702, 1964.

[29] L. Kocis and W. J. Whiten. Computational investigations of low-discrepancy sequences. *ACM Transactions on Mathematical Software (TOMS)*, 23(2):266–294, 1997.

[30] A. Birth, T. Geyer, H. D. Mouton, and T. Dorfling. Generalized three-level optimal pulse patterns with lower harmonic distortion. *IEEE Transactions on Power Electronics*, 2019. Early Access, Digital Object Identifier: 10.1109/TPEL.2019.2953819.

[31] J. B. Rawlings and D. Q. Mayne. *Model Predictive Control: Theory and Design*. Nob Hill Publ., 2009.

[32] J. Rodríguez, M. P. Kazmierkowski, J. R. Espinoza, P. Zanchetta, H. Abu-Rub, H. A. Young, and C. A. Rojas. State of the art of finite control set model predictive control in power electronics. *IEEE Transactions on Industrial Informatics*, 9(2):1003–1016, May 2013.

[33] T. Geyer, N. Oikonomou, G. Papafotiou, and F. D. Kieferndorf. Model predictive pulse pattern control. *IEEE Transactions on Industry Applications*, 48(2):663–676, March 2012.

[34] P. Cortés, M. P. Kazmierkowski, R. M. Kennel, D. E. Quevedo, and J. Rodríguez. Predictive control in power electronics and drives. *IEEE Transactions on Industrial Electronics*, 55(12):4312–4324, December 2008.

[35] J. Rodríguez, J. Pontt, C. A. Silva, P. Correa, P. Lezana, P. Cortés, and U. Ammann. Predictive current control of a voltage source inverter. *IEEE Transactions on Industrial Electronics*, 54(1):495–503, February 2007.

[36] R. Vargas, P. Cortés, U. Ammann, J. Rodríguez, and J. Pontt. Predictive control of a three-phase neutral-point-clamped inverter. *IEEE Transactions on Industrial Electronics*, 54(5):2697–2705, October 2007.

[37] T. Geyer and D. E. Quevedo. Multistep finite control set model predictive control for power electronics. *IEEE Transactions on Power Electronics*, 29(12):6836–6846, December 2014.

[38] T. Geyer and D. E. Quevedo. Performance of multistep finite control set model predictive control for power electronics. *IEEE Transactions on Power Electronics*, 30(3):1633–1644, March 2015.

[39] T. Geyer, P. Karamanakos, and R. Kennel. On the benefit of long-horizon direct model predictive control for drives with LC filters. In *Proc. IEEE Energy Conversion Congress and Exposition (ECCE)*, pages 3520–3527, September 2014.

[40] J. Holtz and B. Beyer. Off-line optimized synchronous pulsewidth modulation with online control during transients. *EPE Journal*, 1(3):193–200, December 1991.

[41] J. Holtz and B. Beyer. Fast current trajectory tracking control based on synchronous optimal pulsewidth modulation. *IEEE Transactions on Industry Applications*, 31(5):1110–1120, September 1995.

[42] J. Holtz and N. Oikonomou. Synchronous optimal pulsewidth modulation and stator flux trajectory control for medium-voltage drives. *IEEE Transactions on Industry Applications*, 43(2):600–608, March 2007.

[43] N. Oikonomou and J. Holtz. Closed-loop control of medium-voltage drives operated with synchronous optimal pulsewidth modulation. *IEEE Transactions on Industry Applications*, 44(1):115–123, January 2008.

[44] N. Oikonomou, C. Gutscher, P. Karamanakos, F. D. Kieferndorf, and T. Geyer. Model predictive pulse pattern control for the five-level active neutral-point-clamped inverter. *IEEE Transactions on Industry Applications*, 49(6):2583–2592, November 2013.

[45] P. Al Hokayem, T. Geyer, and N. Oikonomou. Active damping for model predictive pulse pattern control. In *Proc. IEEE Energy Conversion Congress and Exposition (ECCE)*, pages 1220–1227, September 2014.

[46] T. Mouton and T. Geyer. Trajectory-based LQR control of a grid-connected converter with an LCL filter. In *IFAC Conference on Nonlinear Model Predictive Control*, pages 273 – 278, August 2018.

[47] G. F. Franklin, J. D. Powell, M. L. Workman, et al. *Digital control of dynamic systems*, volume 3. Addison-wesley Menlo Park, CA, 1998.

[48] J. A. Pontt, J. R. Rodriguez, A. Liendo, P. Newman, J. Holtz, and J. M. San Martin. Network-friendly low-switching-frequency multipulse high-power three-level PWM rectifier. *IEEE Transactions on Industrial Electronics*, 56(4):1254–1262, April 2009.

[49] J. L. Jerez, G. A. Constantinides, and E. C. Kerrigan. An FPGA implementation of a sparse quadratic programming solver for constrained predictive control. In *Proceedings of the 19th ACM/SIGDA international symposium on Field programmable gate arrays*, pages 209–218. ACM, 2011.